ISSN en trámite

Geofísica Internacional

Revista Trimestral Publicada por el Instituto de Geofísica de la
Universidad Nacional Autónoma de México

México
Volume 57 Number 3
July - September
2018

— Geofísica Internacional —

Dr. Hugo Delgado Granados
Director of Instituto de Geofísica

Dra. Ligia Pérez Cruz
President of Unión Geofísica Mexicana

Editor Chief

Dr. Servando De la Cruz-Reyna
Instituto de Geofísica, UNAM
sdelacrr@geofisica.unam.mx

Technical Editor

Mtra. Andrea Rostan Robledo
Instituto de Geofísica, UNAM
arostan@igeofisica.unam.mx

Editorial Board

Donald Bruce Dingwell
Earth and Environment
Ludwig Maximilian University of Munich, Germany

Eric Desmond Barton
Departamento de Oceanografía
Instituto de Investigaciones Marinas, Spain

Jorge Clavero
Amawta Consultores, Chile

Gerhardt Jentzsch
Institut für Geowissenschaften
Friedrich-Schiller-Universität Jena, Germany

Peter Malischewsky
Institut für Geowissenschaften
Friedrich-Schiller-Universität Jena, Germany

François Michaud
Géosciences Azur
Université Pierre et Marie Curie, France

Olga Borisovna Popovicheva
Scobeltzine Institute of Nuclear Physics
Moscow State University, Rusia

Jaime Pous
Facultad de Geología
Universidad de Barcelona, Spain

Joaquín Rui
UA Science
University of Arizona, United States

Angelos Vourlidas
Solar Physics Branch
NASA Goddard Space Flight Center, United States

Théophile Ndougsa Mbarga
Department of Physics
University of Yaounde I, Cameroon

Associate Editors

José Agustín García Reynoso
Atmospheric Science Centro de Ciencias de la Atmósfera UNAM, Mexico

Tereza Cavazos
Atmospheric Science
Departamento de Oceanografía Física CICESE, Mexico

Dante Jaime Morán-Zenteno
Geochemistry
Instituto de Geología, UNAM, Mexico

Margarita López
Geochemistry
Instituto de Geología UNAM, Mexico

Avto Gogichaisvilii
Geomagnetism And Paleomagnetism
Instituto de Geofísica UNAM, Mexico

Jaime Urrutia-Fucugauchi
Geomagnetism And Paleomagnetism
Instituto de Geofísica, UNAM, Mexico

Felipe I. Arreguín Cortés
Hydrology
Instituto Mexicano de Tecnología del Agua IMTA, Mexico

William Lee Bandy
Marine Geology And Geophysics
Instituto de Geofísica UNAM, Mexico

Fabian García-Nocetti
Mathematical And Computational Modeling
Instituto de Investigaciones en Matemáticas Aplicadas y en Sistemas UNAM, Mexico

Graciela Herrera-Zamarrón
Mathematical Modeling
Instituto de Geofísica, UNAM, Mexico

Ismael Herrera Revilla
Mathematical And Computational Modeling
Instituto de Geofísica UNAM, Mexico

Rene Chávez Segura
Near-Surface Geophysics
Instituto de Geofísica UNAM, Mexico

Juan García-Abdeslem
Near-Surface Geophysics
División de Ciencias de la Tierra CICESE, Mexico

Alec Torres-Freyermuth
Oceanography
Instituto de Ingeniería, UNAM, Mexico

Jorge Zavala Hidalgo
Oceanography
Centro de Ciencias de la Atmósfera UNAM, Mexico

Shri Krishna Singh
Seismology
Instituto de Geofísica, UNAM, Mexico

Xyoli Pérez-Campos
Seismology
Servicio Sismológico Nacional, UNAM, Mexico

Blanca Mendoza Ortega
Space Physics
Centro de Ciencias de la Atmósfera, UNAM, Mexico

Inez Staciarini Batista
Space Physics
Pesquisador Senior Instituto Nacional de Pesquisas Espaciais, Brazil

Roberto Carniel
Volcanology
Laboratorio di misure e trattamento dei segnali DPIA - Università di Udine, Italy

Miguel Moctezuma-Flores
Satellite Geophysics
Facultad de Ingeniería, UNAM, Mexico

Assistance

Elizabeth Morales Hernández,
Management
eliedit@igeofisica.unam.mx

GEOFÍSICA INTERNACIONAL, Año 57, Vol. 57, Núm. 3, julio - septiembre de 2018 es una publicación trimestral, editada por la Universidad Nacional Autónoma de México, Ciudad Universitaria, Alcaldía Coyoacán, C.P. 04150, Ciudad de México, a través del Instituto de Geofísica, Circuito de la Investigación Científica s/n, Ciudad Universitaria, Alcaldía Coyoacán, C.P. 04150, Ciudad de México, Tel. (55)56 22 41 15. URL: http://revistagi.geofisica.unam.mx, correo electrónico: revistagi@igeofisica.unam.mx. Editora responsable: Andrea Rostan Robledo. Certificado de Reserva de Derechos al uso Exclusivo del Título: 04-2022-081610251200-102, ISSN: en trámite, otorgados por el Instituto Nacional del Derecho de Autor (INDAUTOR). Responsable de la última actualización Saúl Armendáriz Sánchez, Editor Técnico. Fecha de la última modificación: 30 de junio 2018, Circuito de la Investigación Científica s/n, Ciudad Universitaria, Alcaldía Coyoacán, C.P. 04150, Ciudad de México.

El contenido de los artículos es responsabilidad de los autores y no refleja el punto de vista de los árbitros, del Editor o de la UNAM. Se autoriza la reproducción total o parcial de los textos siempre y cuando se cite la fuente completa y la dirección electrónica de la publicación.

Esta obra está bajo una Licencia Creative Commons Atribución-NoComercial-SinDerivadas 4.0 Internacional.

Geofísica
Internacional
Vol. 57, Núm. 3, julio-septiembre de 2018

Contents

Assessing groundwater vulnerability by pollution mapping in Iran: Case study Hamadan – Bahar plain.
Balal Oroji
161

Application of magnetic method on the Argentine continental shelf between 35ºS and 48ºS.
María A. Arecco, Patricia A. Larocca, Francisco Ruiz, Armando T. Canero, Víctor A. Ramos
175

Soil gas radon measurements for investigating the actual status of seismic quiescence along the bounding fault of the Ghab pull-apart basin in western Syria.
Mohamed Al-Hilal, Mohamad K. Abdul-Wahed
177

Geoelectrical Combined Sounding-Profiling Configuration for Characterizing the Sedimentary Phosphatic Environment in Al-Sharquieh Deposits Mine in Syria.
Jamal Asfahani
189

A Graphic Processing Unit (GPU) based implementation of an incompressible two-phase flow model in porous media.
V. Leonardo Teja-Juárez, Luis M. de la Cruz
205

Geofísica Internacional (2018) 57-3: 161-174

Original paper

Assessing groundwater vulnerability by pollution mapping in Iran: Case study Hamadan – Bahar plain

Balal Oroji*

Received: May 16, 2017 ; accepted: March 14, 2018; published on line: July 02, 2018

Resumen

El agua subterránea es vulnerable a la contaminación debido a actividades humanas. Un aspecto fundamental de su manejo es la localización de la vulnerabilidad. El acuífero de Hamadan-Bahar se encuentra en la parte central de la provincia de Hamadan al oeste de Irán, y es una reserva económica prioritaria ya que se utiliza tanto en irrigación como para consumo doméstico. A partir de 2005 se han desarrollado en Irán modelos numéricos para evaluar la vulnerabilidad y varios indicadores hidrológicos de contaminación potencial del agua. La aplicación de métodos como DRASTIC, SINTACS, SI y GOD ha mostrado que las zonas de mayor vulnerabilidad se encuentran al sur y al oeste del acuífero de Hamadan-Bahar. Los resultados indican que con los modelos DRASTIC, SI, GOD y SINTACS, el 7.1, 44.21, 29.56 y 20.16 por ciento de las áreas tienen un alto potencial de vulnerabilidad. Considerando el modelo DRASTIC el 33.6 % del área de estudio presenta una vulnerabilidad baja a la contaminación, mientras que el 29.4% presenta vulnerabilidad moderada. La precisión de los modelos se evaluó aplicando una regresión lineal entre los valores observados de nitratos y la vulnerabilidad estimada por contaminación en los pozos medidos. Una correlación significativa se observó entre los nitratos medidos y el potencial de contaminación evaluada con el modelo DRASTIC $p<0.05$, sin embargo con los modelos GOD, SINTACS e IS no se observó una correlación significativa. Los resultados mostraron que el modelo DRASTIC fue el mejor para estimar la vulnerabilidad del agua subterránea a la contaminación en los pozos medidos..

Palabras clave: DRASTIC; SINTACS; GOD; SI; agua subterránea; vulnerabilidad; contaminación.

Abstract

Groundwater is vulnerable to contamination by anthropological activities. Vulnerability mapping is considered as a fundamental aspect of groundwater management. Hamadan - Bahar aquifer located in the center of Hamadan province in western Iran, is considered as an economic priority resource due to its use in irrigation and domestic consumption. Numerical modeling of assessment of vulnerability and various hydrological indicators of potential pollution of water resources in Iran have been the subject of several studies since 2005. The application of various methods, DRASTIC, SINTACS, SI and GOD, showed that the most vulnerable zones were the southern and western part of the Hamadan - Bahar aquifer. The results showed that with DRASTIC, SI, GOD and SINTACS models, 7.1, 44.21, 29.56 and 20.16 percent respectively of the areas have high potential vulnerability. According to the DRASTIC model 33.6 % of the study area has a low class of groundwater vulnerability to contamination, whereas a total of 29.4% of the study area has moderate vulnerability. Accuracy of the models was evaluated using a linear regression between nitrate observation values and estimated vulnerability to pollution in measured wells. A significant correlation was observed between measured nitrate and pollution potential evaluated by DRASCTIC model $p<0.05$, but no significant correlation was observed for GOD, SINTACS and IS models. The results showed that the DRASTIC model is better than other models to estimate groundwater vulnerability to pollution in the measured wells.

Key words: DRASTIC; SINTACS; GOD; SI; groundwater, vulnerability, pollution.

Balal Oroji
Department of Environments
Faculty of Natural Resources and Environments
Malayer University
Hamadan province, Iran
*Corresponding author: Balaloroji@yahoo.com

Introduction

Groundwater is the main source of drinking water in arid and semiarid areas, and hence its vulnerability assessment management helps to delineate areas that are more susceptible to contamination (Ghazavi *et al*., 2010; Ighbal *et al*., 2014). The groundwater dynamics reflects the response of the groundwater system to external factors such as groundwater consumption, water storage, climate condition, and other human activities (Minville *et al*., 2010; Ghazavi *et al*., 2011, 2012). Groundwater is vulnerable to contamination by anthropological activities and infiltration of urban and industrial wastewater can recharge aquifers and pollute those used for potable water supply (Oiste, 2014; Odukoya and Abimbola, 2010).

The nitrate pollution of groundwater caused by agricultural activity and a substantial increase in fertilizer utilization are also becoming an increasing problem. Recently, groundwater vulnerability mapping is an important key to decision making processes and improving planning in order to prevent groundwater contamination (Mahvi *et al*., 2005). Groundwater vulnerability means the degree of protection that the natural environment provides against the spread of pollution in groundwater and is classified as intrinsic and specific vulnerability (National Research Council, 1993). Specific vulnerability is used to define the vulnerability of groundwater to particular contaminants (Gogu and Dassargues, 2000). Intrinsic vulnerability can be defined as the ease with which a contaminant introduced into the ground surface can reach and diffuse in groundwater (Vrba and Zoporozec, 1994). Groundwater-specific vulnerability is regarded as more meaningful than intrinsic vulnerability, because some affecting factors of intrinsic vulnerability, such as soil media, net recharge or groundwater depth, have been changed due to an increasing effect of human activities. Different methods have been introduced to estimate groundwater vulnerability, that may be divided into three general categories: statistical methods, process-based simulation models, and overlay and index methods (Chenini *et al*., 2015). Therefore, overlay and index methods are based on combining different maps of the region. The more popular type of the overlay and index methods are DRASTIC (Aller *et al*., 1987), AVI (Van Stemproot *et al*., 1992), GOD (Foster, 1987), and IRISH (Daly and Drew, 1999). These models have been used in several places including the Iran (Saatsaz and Sulaiman, 2011), Morocco (Ettazarini, 2006), USA (Fritch *et al*., 2000; Shukla *et al*., 2000), and China (Wen *et al*., 2008; Huan *et al*., 2012). In arid and semiarid regions, irrigation is always changing due to many factors: high evapotranspiration, low rainfall, groundwater quality, structural, and soil condition. In most arid countries, increasing populations and high living standards causes excessive water demands used in urban and industry's needs. Water used in irrigation has also been an important water demand. In arid and semiarid regions over exploitation of groundwater induced alarming declines in water levels (Edoulati *et al*., 2013). One of the most important issues in this regard is that, remediation of contaminated aquifers is expensive.

To recognize the need to an efficient method to protect groundwater resources from contamination, scientists and managers develop aquifer vulnerability techniques for predicting which areas are the most vulnerable (Mueller *et al*., 2012; Chenini *et al*., 2015). During the past years the assessment of groundwater vulnerability to pollution has been subject of intensive research and a variety of methods have been developed. To evaluate aquifer vulnerability, the GIS and remote sensing tools are combined to various methods: standard DRASTIC, GOD, SINTACS and SI, also used to evaluate aquifer vulnerability to pollution. A comparative study of the vulnerability maps was performed in order to choose the best method (Teixeira *et al*., 2015; Chenini *et al*., 2015). Because of expansion of agricultural activities, of excessive use of chemical fertilizers, and of location of industrial and municipal wastewater of Hamadan, it is possible for this aquifer to be polluted. The aim of the present study is to assess the aquifer vulnerability of Hamadan - Bahar plain and to recognize the sensitive areas against pollution. Recognizing the vulnerability of groundwater will help to manage their quality and protect groundwater resources. The possibility of pollutants reaching and releasing into the groundwater after contaminating the ground, is called the aquifer vulnerability. In this study aquifer vulnerability assessment is to identify areas prone to pollution that were modeled via the DRASTIC, GOD, SINTACS and SI models, and the Maps generated for each parameter were classified and combined based on the models.

Materials and Methods

In this study, the vulnerability rating used is the SI, SINTACS, GOD, and DRASTIC (Aller *et al*., 1987). Before starting detailed data collection, some general information pertaining to the socioeconomic, physical characteristics and demographic, settlement patterns and water supply schemes of the communities under study were gathered. This information has been used as a base for planning the field data collection and determining the selection of the sample population (Tadesse *et al*., 2013). The parameters used in these models are: Topography (T) that to the slope percent of the land surface which was determined directly from the topographic maps of Hamadan area (scale 1:50.000). Soil Media (S) index obtained by digitizing the existing soil maps, with 1:50.000 scale were required from Hamadan Research and Education Center for Agriculture and Natural Resources and cover the entire region. The Water Table Fluctuations method (WTF) was used to calculate Net Recharges (R) parameter. One of the major impacts of the integrated watershed management program was on improving groundwater recharge and its availability (Pathak *et al*., 2013). It estimates groundwater recharge as the product of specific yield and the annual rate of water table rise added to the total groundwater draft ended by the equivalent permeability, which is found from well logs (Sophocleous, 1991). One of the most important parameters used in these models is the water depth (D) index. This index represents the depth from the land surface to the first groundwater aquifer. It determines the thickness of material through which infiltrating water must move before reaching the aquifer-saturated zone (Witczak *et al*., 2004). Consequently, the depth of the groundwater impacts on the interaction degree between the percolating contaminant and subsurface materials and, therefore, on the degree and extent of physical and chemical attenuation and degradation processes, the depth groundwater distribution was established by subtracting the groundwater level, measured in 35 wells in Hamadan - Bahar aquifer, from the topographic elevation in the corresponding cell location (Rahman, 2008). Hydraulic Conductivity (C), is defined as the ability of aquifer materials to transmit water which, controls the rate at which groundwater will flow under a given hydraulic gradient. The rate, at which the groundwater flows, also controls the rate at which it enters the aquifer. Figure 1 shows the Flowchart of methodology for groundwater pollution vulnerability analysis.

Study Area

The study area is situated in the Hamadan province and partially in the Central province of northwest Iran, covering an area from latitude 34° N to 35° and from longitude 48°E to 49°30′E (Figure 2). The highest elevation, 3.580 meters, occurs at the Kuh-e Alvand south of Hamadan. The lowest elevations, slightly less than 1.500 meters, occur along the water courses on the western margin of the sheet. The survey area was flown in blocks of constant barometric altitude of 7.000 feet IN METERS, 8.000 feet

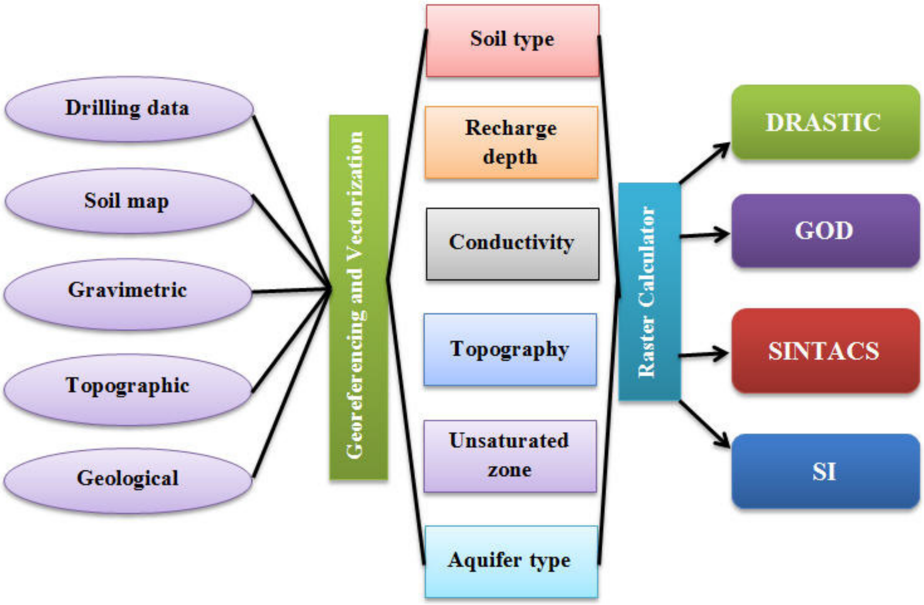

Figure 1. Flowchart of methodology for assessing groundwater vulnerability in the study area.

IN METERS, and 9.500 feet IN METERS with higher portions of the area drape flown, and at a terrain clearance of 1.500 feet in the northeast corner of the quadrangle. Traverses were flown with 7.5 km spacing at headings of 45°/225° for all the blocks (Akhavan *et al*., 2011). The lines were flown with a 40 km spacing perpendicular to the traverses. Refer to the map for exact flight path locations. Numbers on the flight path refer to either line numbers or fiducial (data point) numbers. The most prominent geologic feature is the belt of metamorphic and igneous rocks which trends northwest-southeast. This belt consists largely of Hamadan phyllites with well-developed hornfels near the margins of post-Cretaceous granodiorite intrusions. An area of more mafic igneous material occurs northwest of Hamadan. Paleozoic marbles and Cretaceous crushed limestone and igneous bodies occur in the Zagros thrust belt in the southwestern corner of the sheet. Cretaceous limestone and Oligo-Miocene marbles and limestone's occupy the northeastern and southeastern portions of the sheet. Faulting in this area trends northwest-southeast except for the Mesozoic sedimentary zone east of Hamadan where there is a north-northeast to south-southwest trend (Akhavan *et al*., 2011).

Methodological analysis

The Hamadan - Bahar alluvial aquifer is an important water resource used for irrigation, therefore the aquifer vulnerability to pollution by generic pollutants has been studied by applying the following methods.

A raster map was made from interpolation of the well data using the GIS software for each indicator. To obtain the vulnerability indexes the corresponding weight and rating according to the formula of each method was given to each indicator. All indicators in different models were mapped (Philes, 2004). The slope map was obtained from the digital elevation model and the maps of soils were scanned and then processed from the Soil Map. Each indicator was classified on certain vulnerability classes with values from the DEM. The distribution of each indicator was mapped using the Kriging interpolation technique. After data classification for each indicator, a spatial mapping in Raster format by interpolation of these indicators was necessary. All the maps were projected in "WGS 1984 UTM Zone 39 N, datum Carthage". At ArcGIS software maps are classified by "symbology" and then

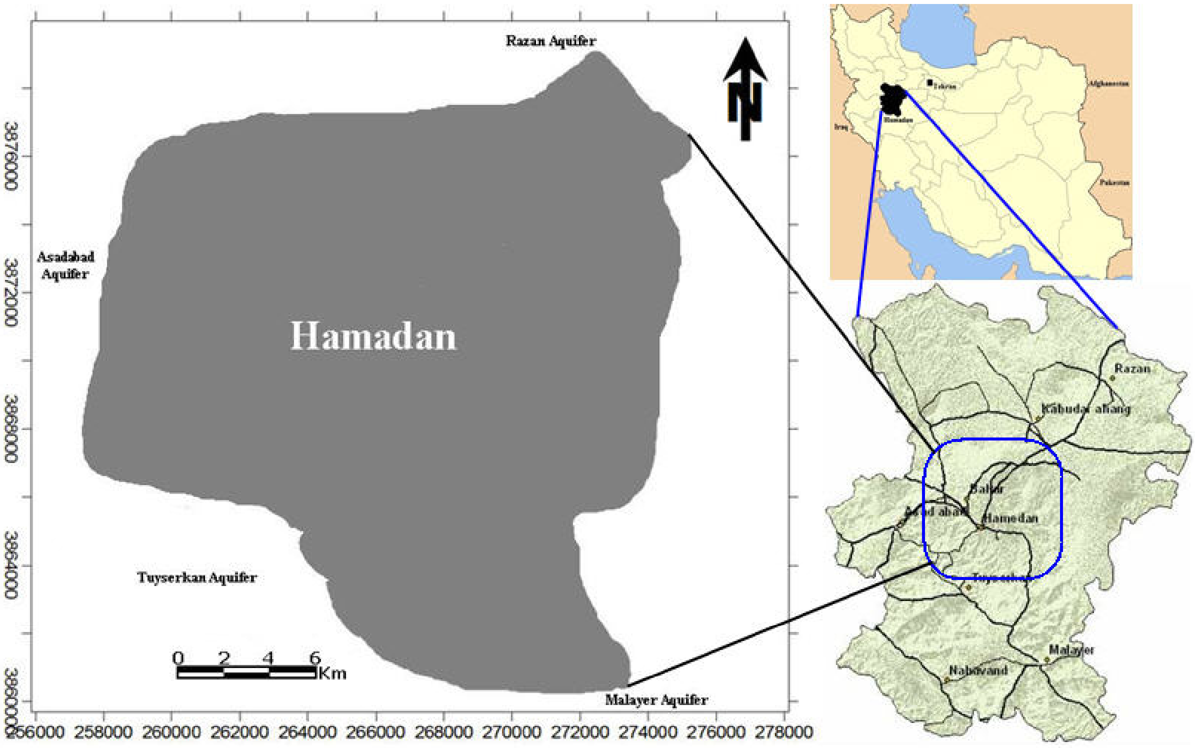

Figure 2. Location of Hamadan – Bahar Plain study area.

cut with the tool "Extract by Mask" ; then they will be recorded in Raster "Tiff" format. The maps are then superposed through "ArcScene," and the final product of vulnerability has been deducted by the "Raster calculator" tool, using the formulas already defined previously and multiplying the classified indicators by their equivalent weight.

For DRASTIC method, inherent in each hydrogeological setting are the physical characteristics that affect the groundwater pollution potential. After the factors such as transmissivity, temperature, aquifer chemistry, gaseous phase transport, tortuosity and some others have been evaluated, the most important factors that control the groundwater pollution potential have been determined to be Net Recharge, Soil Type, Depth to Water, Topography, Aquifer Material, impact of the Unsaturated Zone and Aquifer Media of the Hydraulic Conductivity, in short DRASTIC. In the following, a numerical ranking system to assess groundwater pollution potential in hydrogeological setting has been devised (Aller *et al*., 1987). It assigns a note between 1 and 10 and a weight between 1 and 5 for each used parameter. DRASTIC models use Eq. (1).

$$\begin{aligned} DI = {} & Cp \times Cc + Ip \times Ic + Tp \times Tc + Sp \times Sc \\ & + Ap \times Ac + Rp \times Rc + Dp \times Dc \end{aligned} \qquad (1)$$

where, DI is the vulnerability index based on the DRASTIC model; C: hydraulic Conductivity; I: Unsaturated zone; T: Topography; S: Soil Media; A: Aquifer Material; R: Net Recharge and D: Depth to Water.

The GOD method is an empirical method for the assessment of aquifer pollution vulnerability developed in Great Britain; this method uses three indicators: Overlying lithology, Depth to groundwater and Groundwater occurrence. Values from 0 to 1 can be assigned to the indicators (Foster, 1987). For GOD models used Eq. (2).

$$IGOD = C_i \times C_a \times C_p \qquad (2)$$

Where, C_i: Aquifer type; C_a: Saturated zone and C_p: Depth.

The acronym SINTACS stands for seven indicators included in the method: Net recharge, Depth to water, Vadose zone, Slope, Hydraulic Conductivity, Aquifer media and Soil media. The SINTACS method was established for hydrogeological, climatic and impacts settings, typical of the Mediterranean countries. In the same way that DRASTIC method, SINTACS assigns notes and weights for each of these indicators (Civita and De Maio, 2004) using Eq. (3).

$$\boldsymbol{I_v = Sp \times Sc + Cp \times Cc + Ap \times Ac + Tp \times Tc + Np \times Nc + Ip \times Ic + Sp \times Sc} \qquad (3)$$

where $\boldsymbol{I_v}$ is the vulnerability index based on the SINTACS model; $\boldsymbol{S}$: Slope; $\boldsymbol{C}$: Conductivity; $\boldsymbol{A}$: Hydrogeological aquifer characteristics; $\boldsymbol{T}$: Soil type; $\boldsymbol{N}$: Vadose zone; $\boldsymbol{I}$: Net recharge and $\boldsymbol{S}$: Depth to water.

Specific vulnerability is the term used to define the vulnerability of groundwater to a particular contaminant or group of contaminants. SI method is a vulnerability method for evaluating the specific vertical vulnerability to pollution originated by agricultural activities mainly by nitrates (Ribeiro, 2000). SI assigns notes and weight for each of these indicators in the following way. For SI models Eq. (4) was used.

$$\begin{aligned} IS = {} & Dp \times Dc + Rp \times Rc + Ap \times Nc \\ & + Tp \times Tc + OSp \times OSc \end{aligned} \qquad (4)$$

Where: D: Depth to water; R: Net recharge; A: Lithology; T: Topography and OS: Soil Occupation.

The results

The results of DRASTIC model are shown in Figure 3.

The results of GOD model are shown in Figure 4.

The results of SINTACS model are shown in Figure 5.

The results of SI model are shown in Figure 6.

Discussion

Groundwater contamination risk mapping was carried out by overlay of layers representing the different indicators in the parametric models. Theoretically an overlay was necessary for each indicator. However some indicators are frequently closely associated. In some areas, topography and soil are intimately related, also in other areas, the vadose zone and aquifer media are the same. Values for hydraulic conductivity was frequently extrapolated from only a few points of reference and simply estimated from aquifer media. The data used to generate the Vulnerability Index Map is produced at a variety of scales. Through a function specific to the GIS software the overlay function, the various

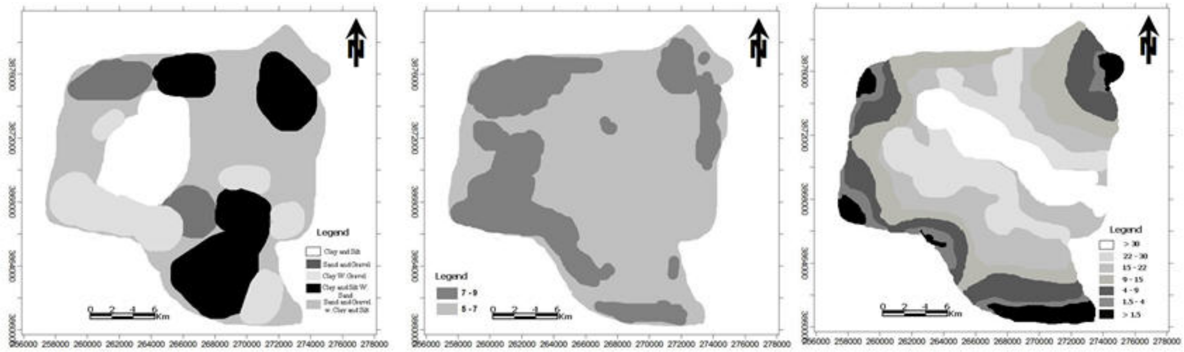

a. Vadose Zone Material

b. Recharge

c. Depth to Water

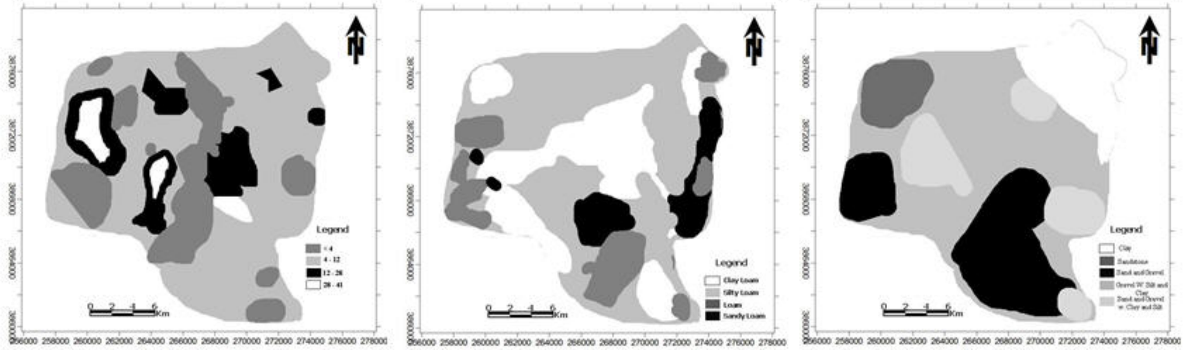

d. Conductivity

e. Soil Media

f. Aquifer Media

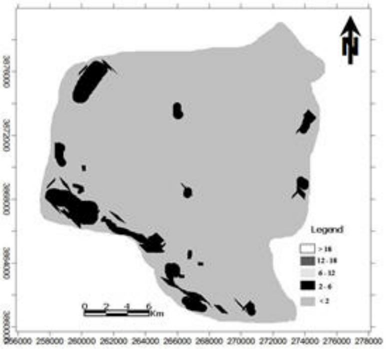

g. Topography

Figure 3. Mapping of DRASTIC model indicators.

maps for each index models are combined through the map calculator function from the spatial analyst extension resulting in the vulnerability map of groundwater. After mapping all the indicators, the vulnerability maps were obtained by overlaying the individual maps and calculating the indices on a grid map (Figure 7). The Vulnerability Index for each grid cell was calculated as the weighted sum of the indicators according to equation 4. Finally, the areas on the final map are labeled with the appropriate hydrogeologic setting. The vulnerability indexes for all models are calculated and the final vulnerability map was subdivided into classes related to vulnerability degrees according to the classification of Engel *et al*. (1996).

The comparison between DRASTIC, SINTACS, SI and GOD methods shows that the closest results are those from the method SINTACS and SI, modified versions of the DRASTIC method adapted to climate prevailing in the study area. The DRASTIC vulnerability map, provides, in turn, more detailed results widely different from other methods (Figure 8). The results showed that the maximum contamination potential in the Hamadan-Bahar plain groundwater was observed in the south, west and northeast borders of the plain. Also there were areas with very low and low potential in the center, north and east of the plain. Both techniques prospected the vulnerability potential in Hamadan - Bahar plain with the same accuracy. This region is an

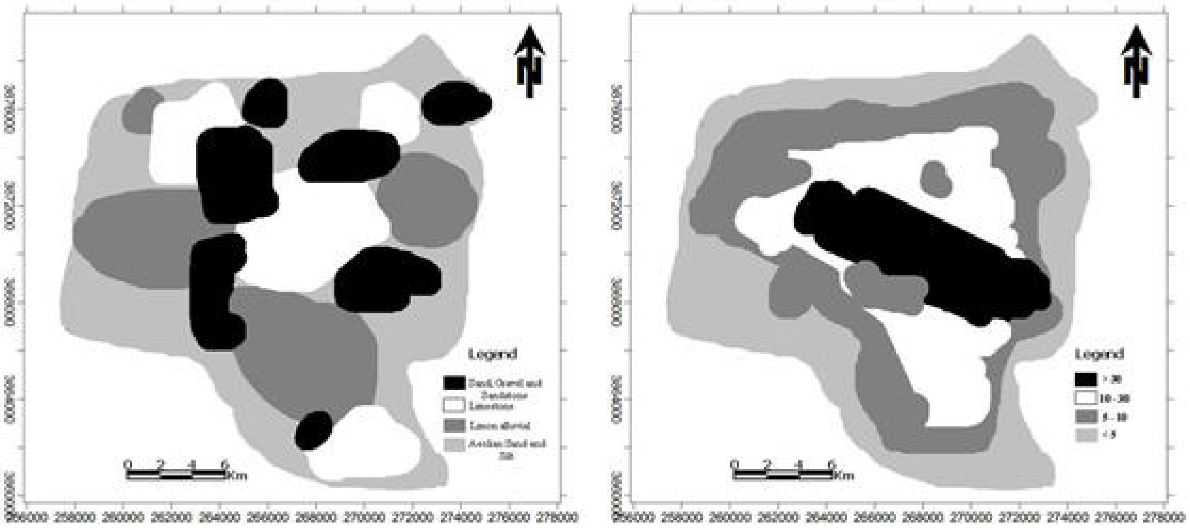

a. Aquifer lithology

b. Depth to Water

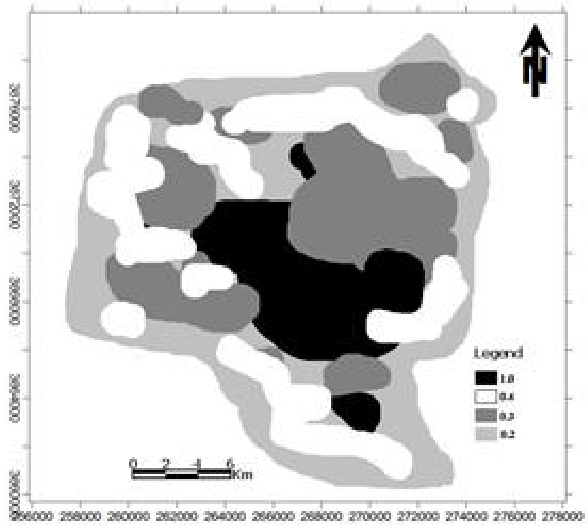

c. Aquifer Media

Figure 4. Mapping of GOD model indicators.

area of high agricultural activity with an intense use of chemical fertilizers. The DRASTIC map resulting from overlaying the seven thematic maps shows four classes, as indicated in Figure 8. The highest class of Vulnerability Index (VI: ☐ 200) covers 7.1% of the total surface in the central part of the study area (Table 1). This condition is due to the high aquifer permeability coming from the vadose zone sediments nature.

The aquifer combination was of quaternary alluvium and sandstones, medium recharge, shallow groundwater and medium hydraulic conductivity. This results in a low capacity to attenuate the contaminants. Also, very low vulnerability, which is represented by 14.7% of the total Hamadan surface, are essentially due to the deep groundwater, the vadose zone sediments and the low permeability, added to the low hydraulic conductivity. As well as the low recharge rate, we assume that these are the same conditions in the case of low vulnerability, with less degree of impact for these indicators. The moderate vulnerability represents 29.4% of the study area. Vulnerability pattern is mainly dictated by the variation of the permeability and the vadose zone (Aranyossy, 1991). The recharge and the depth of groundwater are two

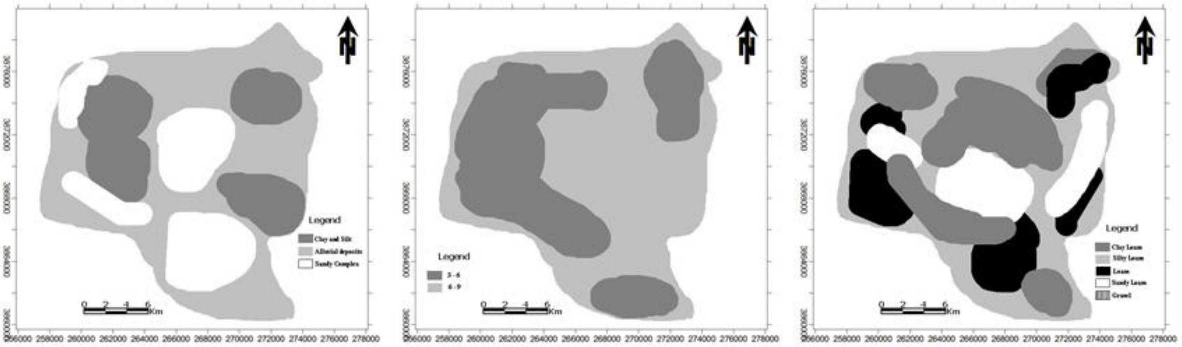

a. Vadose Zone Material

b. Recharge

e. Soil Media

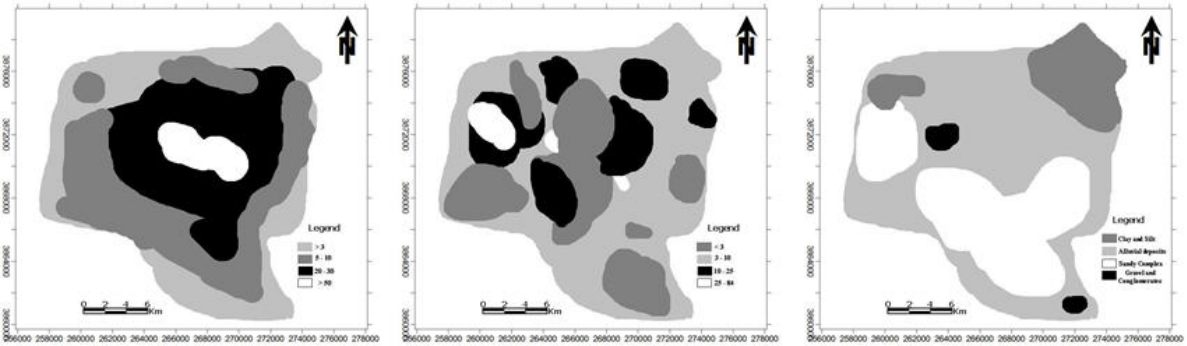

c. Depth to Water

d. Conductivity

f. Aquifer Media

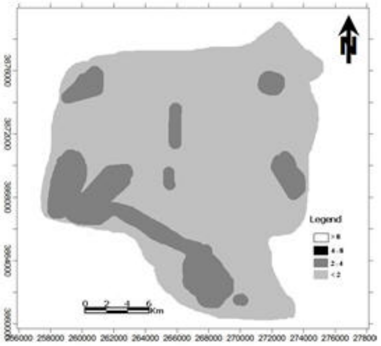

g. Topography

Figure 5. Mapping of SINTACS model indicators.

indicators having an influence on vulnerability degrees to pollution. The application of SI, susceptibility index method indicates the high vulnerable zones to be contaminated by pollutants (Figure 8). The most vulnerable areas have an indicator between 85 and 100. Zones which have indicator value less than 45 are the less vulnerable (Table 2).

The use of the SI Model SINTACS indicates the very high vulnerable zones to be contaminated by pollutants (Figure 8). The most vulnerable areas have an index between 187 and 210. Zones which have index values less than 106 are the less vulnerable (Table 2). The GOD Model application indicates the very high vulnerable zones to be contaminated by pollutants (Figure 8). The most vulnerable areas have an index between 0.5 and 0.7 (Table 2). Zones which have index value between 0.1 and 0.3 are the less vulnerable. A statistical comparison among the vulnerability maps generated by each method has been carried out. Figure 8 shows the difference of classification between the used methods of vulnerabilities. This comparison shows a certain similarity between the results obtained using the SINTACS and SI methods (Rahman, 2008).

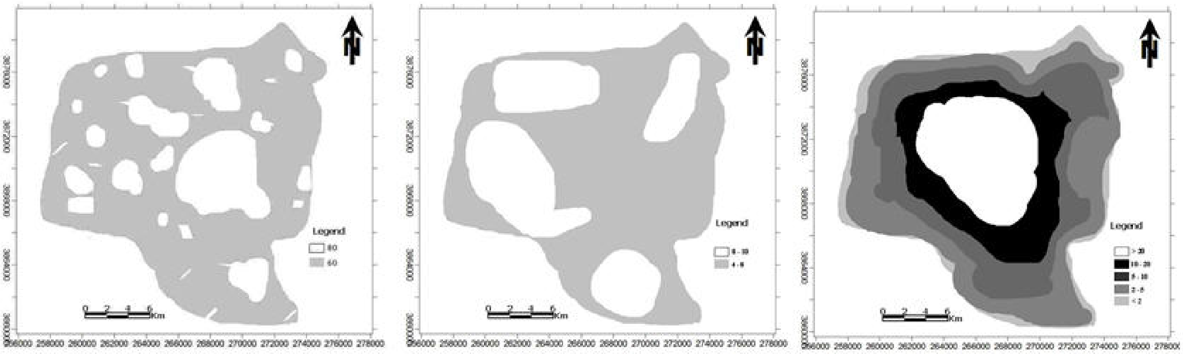

a. Aquifer lithology

b. Recharge

c. Depth to Water

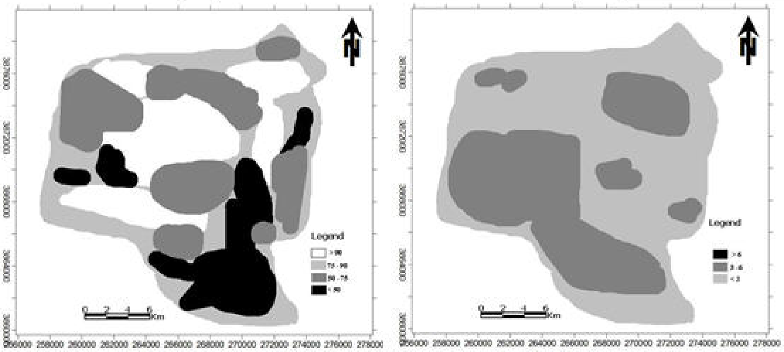

d. Occupation of the soil

f. Topography

Figure 6. Mapping of SI model indicators.

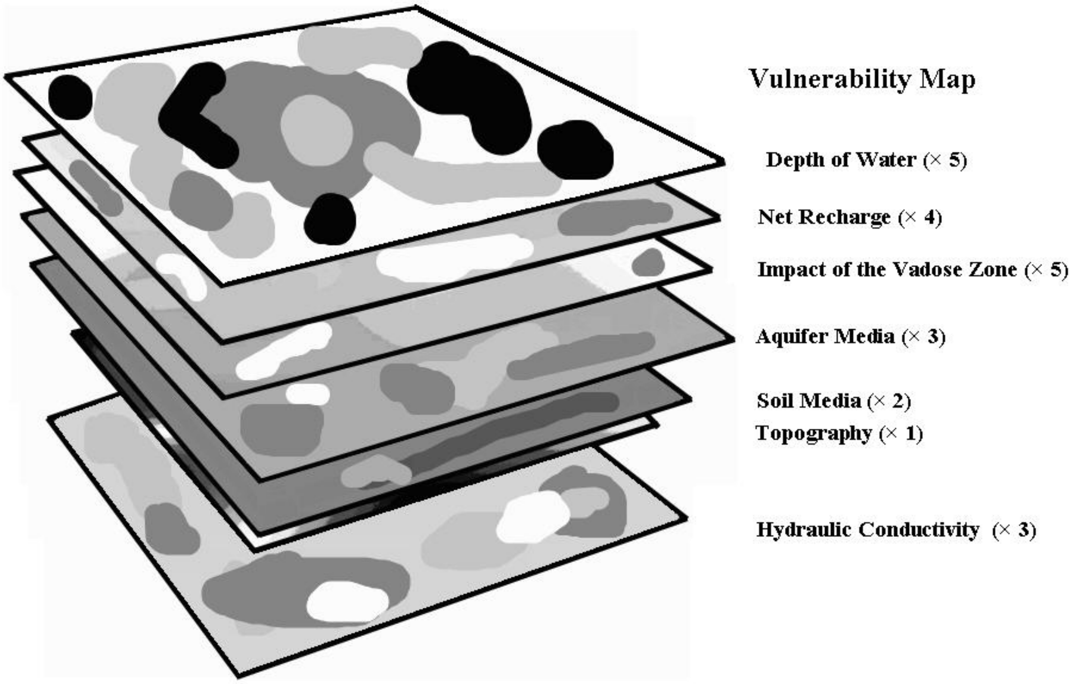

Figure 7. Overlaying of indicators.

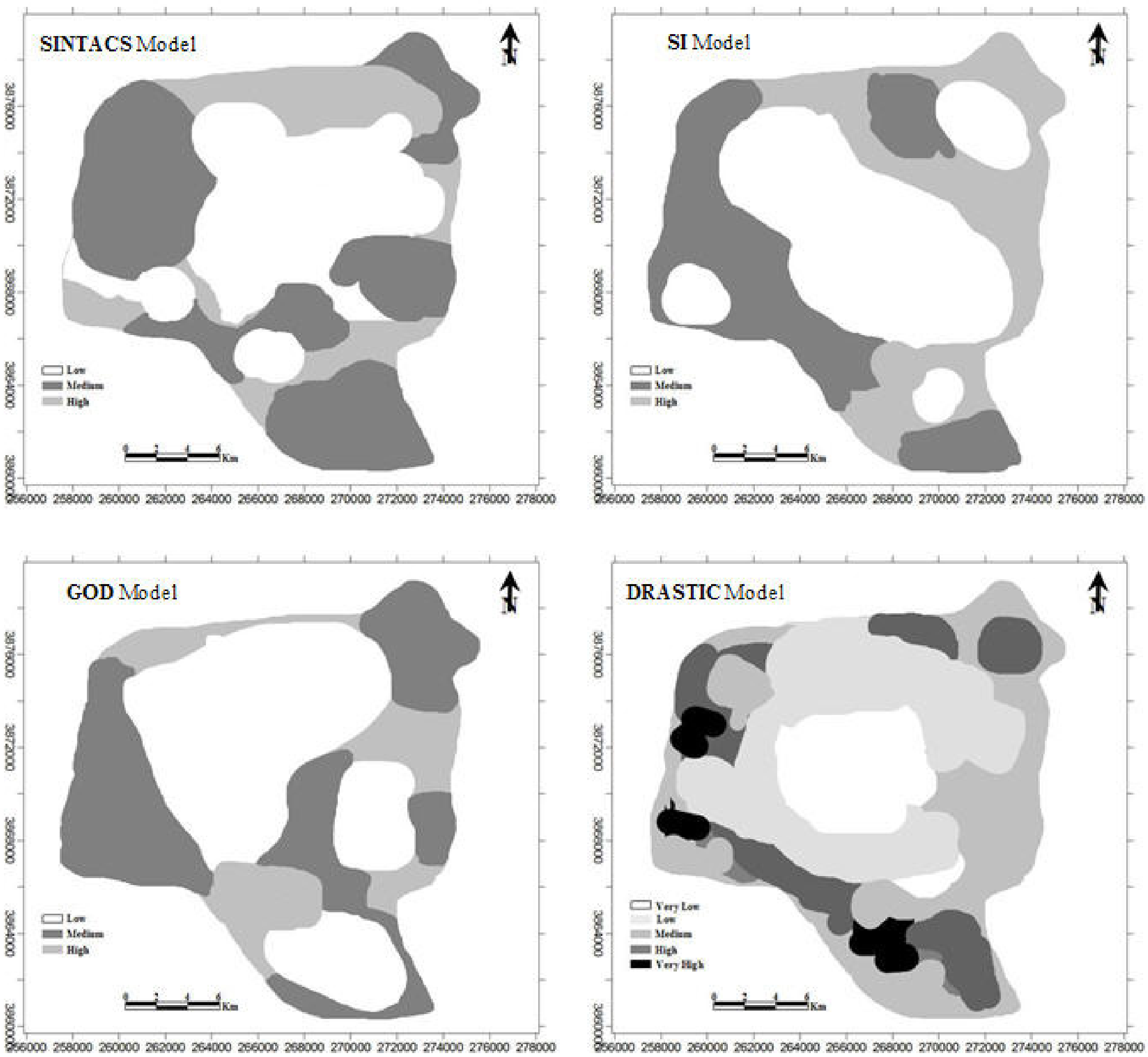

Figure 8. Vulnerability map models of the study area.

Table 1. Evaluation criteria of the degree of vulnerability in DRASTIC model.

Vulnerability	Vulnerability Index	Area	
		(Km^2)	(%)
Very Low	1 – 60	70.56	14.7
Low	61 – 120	180.48	33.6
Medium	121 – 160	121.92	29.4
High	161 – 200	72.96	15.2
Very High	> 200	34.08	7.1

Also, the DRASTIC map classification shows different results. We see much more of a class at the DRASTIC method, this method is thus more suitable to use in our case. So, in conclusion a specific vulnerability study using the modified DRASTIC method, especially in nitrate, was more recommended for this type of environment. It helps to protect the most vulnerable areas and to guide investors to take decisions.

Table 2. Evaluation criteria of the degree of vulnerability in SI, GOD and SINTACS models.

Vulnerability	SI model Area		GOD model Area		SINTACS model Area	
	(Km^2)	(%)	(Km^2)	(%)	(Km^2)	(%)
Low	173.5	36.14	217.54	45.32	168.9	35.22
Medium	94.3	19.65	120.58	25.12	214.3	44.62
High	212.2	44.21	141.88	29.56	96.8	20.16

Models Validation

Validation refers to some independent procedure that can verify the results of the vulnerability analysis. Verification of vulnerability assessments can be done in many different ways. The most common approach, particularly for verification of assessments done with overlay and index methods, is to compare the vulnerability map with the actual occurrence of some common pollutant in groundwater. Typical pollutants used are nitrate and pesticides (Javadi *et al*., 2001 2011 in the reference list CHECK). Nitrate concentration was selected as the primary contamination parameter to validate models in the present study. According to the results, a significant correlation was observed between measured nitrate and pollution potential evaluated by DRASTIC, but no significant correlation was observed with other models. This value is for the DRASTIC model $P<0.01$. The correlation coefficient for other models was $P<0.05$, which indicates more accuracy with the DRASTIC model in this study area. Figure 9 shows the distribution map of nitrate parameter in the study area.

Comparative analysis between DRASTIC results and nitrate levels has been used in several studies (Assaf and Saadeh, 2009). Javadi *et al*. (2011) modified the DRASTIC model using nitrate measurements. They showed that the correlation coefficient between DRASTIC index and nitrate concentration was 68 % in the modified model that was substantially higher than 23 % obtained for the original model. Huan *et al*. (2012) indicated that mapping of groundwater vulnerability to nitrate can be applied for sensible groundwater resource management and land-use planning.

DRASTIC, GOD and AVI models were compared in an alluvial aquifer of Florina basin in Greece using a linear regression analysis (Kazakis and Voudouris, 2011). To obtain a comparable value, a quantitative comparison of vulnerability methods was involved. The results of this study indicate that the GOD method has a stronger correlation with the other two methods, and the three models produced comparable vulnerability maps. Ighbal *et al*. (2014) compared a GIS-based fuzzy pattern recognition model with a standard DRASTIC model in Ranchi district, Jharkhand, India. The results of this study indicated that GIS-based fuzzy pattern recognition model had better performance than the standard DRASTIC model. Polemio *et al*. (2009) indicate that the GOD method is useful for mapping large areas with high vulnerability contrasts, whereas DRASTIC are useful for any type of aquifer. Correlation coefficient between DRASTIC index and nitrate concentration was 68 % compared with 28 % for GOD index.

Conclusions

The databases which are behind all layers can anytime be updated. Also, the use of GIS facilitates the rapid visualization of some elements in the map by selecting them from the attribute table. The vulnerability maps, contamination data and groundwater quality can be used in view of a rapid and correct evaluation of pollution risk. By using this technology, the information will be used in an efficient manner. The models application showed that Hamadan - Bahar groundwater was characterized by low to high vulnerability degrees. The results of all methods showed that the maximum contamination potential in the Hamadan - Bahar plain groundwater was observed in the south, west and northeast borders of the plain. According to the sensitivity analysis the depth to water table was the most effective parameter on the vulnerability potential. There were areas with very low and low potential in the center, north and east of the plain. Both techniques prospected the vulnerability potential in Hamadan - Bahar plain with the same accuracy. Waters are easily accompanied by various geochemical elements coming from toxic pesticides and their extensive use in farmland, and wastewater. So, in high vulnerability areas, we shouldn’t allow additional high risk activities in order to obtain economic advantage and to reduce environmental pollution hazard.

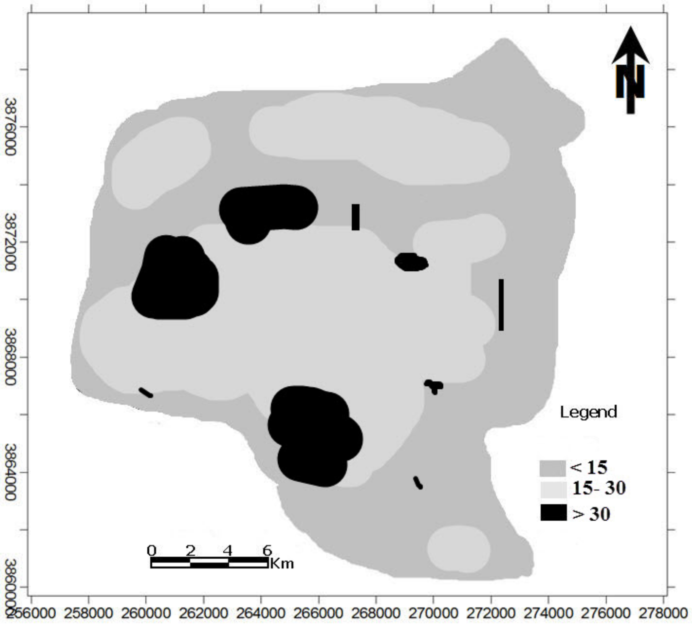

Figure 9. Distribution map of nitrate parameter in the study area.

Acknowledgements

The author would like to thank Mohsen Ghasemi Jahromi and Hashem Karimi of Tehran University for assistance in determining geologic characteristics and processes.

References

Abe K., 1981, Magnitude of large shallow earthquakes from 1904 to 1980. *Phys. Earth. Planet. Interiors*, 27, 72-92.

Akhavan S., Mousavi S.F., Abedi-Koupai J., Abbaspour K.C. 2011, Conditioning DRASTIC model to simulate nitrate pollution case study: Hamadan–Bahar plain. Environ. Earth Sci., 63, 1155-1167.

Aller L., Bennet T., Lehr J.H., Petty R.J., Hachet G. 1987, DRASTIC: A standardised system for evaluating groundwater pollution potential using hydrogeologic settings (EPA 600/2-87). Environmental Research Laboratory, Office of Research and Development, US Environmental Protection Agency Report, Tucson pp. 622.

Aranyossy J.F. 1991, The Contribution of Isotope Techniques to Study the Recharge under Constraints Techniques and Climate Extremes," Diplomafor Accreditation to Supervise Research in Sciences, University of Paris sud, Orsay, pp. 576.

Assaf, H. and Saadeh, M., 2009. Geostatistical assessment of groundwater nitrate contamination with reflection on DRASTIC vulnerability assessment: the case of the Upper Litani Basin, Lebanon. Water Res. Manag., 23, 775-796.

Chenini I., Zghibi A., Kouzana L. 2015, Hydrogeological investigations and groundwater vulnerability assessment and mapping for groundwater resource protection and management: State of the art and a case study. J. Afric. Earth. Sci., 109, 11-26.

Civita M., De Maio M. 2004, Assessing and mapping groundwater vulnerability to contamination: The Italian "combined" approach. Geofis. Int., 43, 513-532.

Daly D., Drew D. 1999, Irish methodologies for karst aquifer protection. In: Beek B (ed) Hydrogeology and engineering geology of sinkholes and karst. Balkema, Rotterdam, pp 267-272.

Engel B., Navulur K., Cooper B., Hahn L. 1996, Estimating Groundwater Vulnerability to Non-Point Source Pollution from Nitrates and

Pesticides on a Regional Scale. In: K. Kovar and H. P. Nachtnebel, Eds., Application of Geographic Information Systems in Hydrology and Water Resources Management, IAHS Press, Wallingford, pp. 521-526. http://www.iahs.info/redbooks/235.htm

Edoulati N., Boutaleb S., Bettar I., Ouchbani A. 2013, Contributions of Chemical and Isotopic Tools for Understanding the Groundwater Modes Recharge and Flow in the Lower Cretaceous Aquifer in the Moroccan Sahara. J Warer Resour Protec 5, pp. 183-199. doi:l0.4236/jwarp.2013.52020

Ettazarini S. 2006, Groundwater pollution risk mapping for the Eocene aquifer of the Oum ErRabia Basin, Morocco. Environ. Geol., 51, 341-34 7

Foster S.S.D. 1987, Fundamental concepts in aquifer vulnerability, pollution risk and protection strategy. In: van Duijvenbooden W, van Waegeningh HG (eds) Proceedings and information in vulnerability of soil and ground-water to pollutants, vol 38. TNO Committee on Hydrological Research, The Hague, pp 69-86

Fritch T.G., Mcknight C.L., Yeldennan J.C., Arnold J.G. 2000, An aquifer vulnerability assessment of the Paluxy aquifer, central Texas, USA, using GIS and a modified DRASTIC approach. J. Environ. Manag., 25, 337-345

Ighbal J., Gorai A.X., Katpatal Y.B., Pathak G. 2014, Development of GIS-basod fuzzy pattern recognition model (modified DRA. STIC model) for groundwater vulnerability to pollution assessment. Int. J. Environ. Sci. Techno., 12, 3161-3174. doi: 10.1007/s13762-014-0693-x

Ghazavi R., Vali A.B., Eslamian S. 2010, Impact of flood spreading on infiltration rate and soil properties. Water Resour. Manag., 14, 2781-2793

Ghazavi R., Thomas Z., Hamon Y., Merot P. 2011, Soil water movement under a bottomland hedgerow during contrasting meteorological conditions. Hydro. Process., 25, 9-30

Ghazavi R., Vali A.B., Eslamian S. 2012, Impact of flood spreading on groundwater level variation and groundwater quality in an arid environment. Water Resour. Manag., 26, 1651-1663

Gogu R.C., Dassargues A. 2000, Current trends and future challenges in ground-water vulnerability assessment using overlay and index methods. Environ. Geol., 39, 549-559

Huan H., Wang J., Teng Y. 2012, Assessment and validation of groundwater vulnerability to nitrate based on a modified DRASTIC model: a case study in Jilin City of northeast China. Sci., Total Environ., 440, 14-23

Javadi S, Kavehkar N, Mousavizadeh MH, Mohammadi K., 2011, Modification of DRASTIC model to map groundwater vulnerability to pollution using nitrate measurements in agricultural areas. J Agric Sci Technol 13, 239–249.

Kazakis N., Voudouris K., 2011, Comparison of three applied methods of groundwater vulnerability mapping: A case study from the Florina basin, Northern Greece. In Advances in the research of aquatic environment, (pp. 359-367). Springer, Berlin, Heidelberg.

Mahvi A.H., Nouri J., Babael A.A., Nabizadeh R. 2005, Agricultural activities impact on groundwater nitrate pollution. Int. J. Environ. Sci. Techno., 2, 41-47

Minville M., Krau S., Brissette F., Leconte R. 2010, Behaviour and performance of a water resource system in Quebec (Canada) under adapted operating policies in a climate change context. Water Resour. Manag., 24, 1333-1352

Mueller N.C., Braun J., Bruns J., Černík M., Rissing P., Rickerby D., Nowack B. 2012, Application of nanoscale zero valent iron (NZVI) for groundwater remediation in Europe. Environ. Sci. Poll. Research., 19, 550-558.

National Research Council 1993, Groundwater vulnerability assessment, contaminant potential under conditions of uncertainty. National Academy Press, Washington, DC

Odukoya A.M., Abimbola A.F. 2010, Contamination assessment of surface and groundwater within and around two dumpsites. Int. J. Environ. Sci. Techno., 7, 367-376

Oiste A.M. 2014. Groundwater quality assessment in urban environment. Int. J. Environ. Sci. Technol., 11, 2095-2102

Pathak P., Chourasia A.K., Wani S.P., Sudi R. 2013, Multiple Impact of Integrated Watershed Management in Low Rainfall SemiArid Region: A Case Study from Eastern Rajasthan, India. J. Water Resour .Protect., 5, 27-36. doi:l0.4236/jwarp.2013.51004

Philes C.J. 2004, The Geostatistical Modeling of Spatial Variability and Its Applications. Thesis, University Pierre et Marie Curie, Paris 71 pp.

Polemio, M., Casarano, D. and Limoni, P.P., 2009. Karstic aquifer vulnerability assessment methods and results at a test site (Apulia, southern Italy). Natural Hazards and Earth System Sciences.

Rahman A. 2008. A GIS based DRASTIC model for assessing groundwater vulnerability in shallow aquifer in Aligarh, India. Appl. Geography., 28, 32-53. doi:l0.l016/j.apgeog.2007.07.008

Ribeiro L. 2000, Desenvolvimento de um ı´ndice para avaliar a susceptibilidade, ERSHA-CVRM, 8 pp.

Saatsaz M., Sulaiman W.N. 2011, GIS DRAS TIC model for groundwater vulnerability estimation of Astaneh-Kouchesfahan plain, Northern Iran. Int. J. Water, 6, 250-254

Shukla S., Mostaghimi S., Shanholt V.O., Collins M.C., Ross B.B. 2000, A county level assessment of ground water contamination by pesticides. Ground. Water Monit. Rev., 20, 104-119

Sophocleous M.A. 1991, Combining the Soil Water Balance and 475 Water Level fluctuation Methods to Estimate Natural Groundwater Recharge: Practical Aspects. J. Hydro., 124, 229-241 doi:l0.1016/0022-1694(91)90016-B

Tadesse A., Bosona T., Gebresenbet G. 2013, Rural Water Supply Management and Sustainability: The Case of Adama Area, Ethiopia. J. Water. Resour. Protect., **5**, 208-221. doi:1O.4236/jwatp.2013.52022

Teixeira J., Chaminé H.I., Marques J.E., *et al.* 2015, A comprehensive analysis of groundwater resources using GIS and multicriteria tools (Caldas da Cavaca, Central Portugal): environmental issues. Environ. Earth. Sci., 73, 2699-2715.

Van Stempvoort D., Ewert L., Wassenaar L. 1992, AVI: a method for groundwater protection mapping in the Prairie Provinces of Canada. Prairie Provinces Water Board Report, 1-14, Regina, SK

Vrba J., Zoporozec A. 1994, Guidebook on mapping groundwater vulnerability. Heise

Wen X, Wu J, Si J 2008. A GIS-based DRASTIC model for assessing shallow groundwater vulnerability in the Zhangye Basin, northwestern China. Environ. Geol., 57, 1435-1442

Witczak S., Duda R., Zurek A. 2004, The Polish Concept of Groundwater Vulnerability Mapping. In: Witkowski A.J., Kowalczyk A., Vrba J. Eds., Groundwater Vulnerability Assessment and Mapping, Internarional Conference of Groundwater Vulnerability Assessment and Mapping, U stron., pp. 62-76.

Geofísica Internacional (2018) 57-3: 175-195

Original paper

Application of magnetic method on the Argentine continental shelf between 35ºS and 48ºS

María A. Arecco*, Patricia A. Larocca, Francisco Ruiz, Armando T. Canero and Víctor A. Ramos

Received: July 04, 2017; accepted: March 20, 2018; published on line: July 02, 2018

Resumen

Se analizaron las anomalías del Campo Magnético Total a partir de datos de una red global, con el propósito de contribuir al conocimiento y caracterización de la plataforma continental argentina (35ºS hasta 48ºS). Para ello se utilizaron técnicas de realce, como la señal analítica, el ángulo tilt, y la segunda derivada vertical. Se calcularon las profundidades de las fuentes magnéticas a partir del método de deconvolución de Euler y el modelado de inversión gravimétrica 2D. A partir de los resultados filtrados del TMA se identificaron grandes zonas de fractura de transferencia. La segunda derivada vertical mostró patrones de alta frecuencia en las anomalías G y Tona, así como también en la serie de anomalías M y alineamientos de fondo oceánico, mostrando el carácter volcánico y episódico de los mismos. El método de deconvolución de Euler permitió localizar fuentes magnéticas discontinuas a lo largo del antiguo cinturón Dom Feliciano-Lavalleja, cuyas profundidades van desde 5000 a 8000 m. Se obtuvieron pocas soluciones tipo diques, escalones de falla en las zonas de fallas de transferencia y el borde entre corteza continental y oceánica. Se localizaron fuentes en la serie-M a profundidades entre 8000 y 12000 m. También, este método permitió calcular las profundidades de la conspicua anomalía Tona entre 8000 y 20000 m. Además, a partir de un modelo de inversión gravimétrico 2-D aplicado sobre un perfil con dirección NE, se identificó un cuerpo máfico-ultramáfico a lo largo de la sutura Patagonia-Gondwana hasta casi la superficie. Este cuerpo podría ser una imbricación de la sutura emplazada en rocas del basamento.

Palabras clave: Plataforma Continental Argentina; Anomalía Magnética Tona; Magnetometría; Interpretaciones magnéticas corticales: Terreno Patagonia.

M. A. Arecco*
P. A. Larocca
Instituto de Geodesia y Geofísica Aplicadas
Facultad de Ingeniería
Universidad de Buenos Aires
Av. Las Heras 2214
Buenos Aires, Argentina
**Corresponding author: marecco@fi.uba.ar*

F. Ruiz,
Instituto Geofísico Sismológico Volponi
Facultad de Ciencias Exactas Físicas y Naturales
Universidad Nacional de San Juan
Ruta 12 Km 17, Jardín de los Poetas, Rivadavia
San Juan, Argentina

A. T. Canero
Departamento de Física
Facultad de Ingeniería
Universidad de Buenos Aires
Paseo Colón 850
Buenos Aires, Argentina

V. A. Ramos
Instituto de Estudios Andinos
CONICET- Facultad de Ciencias Exactas y Naturales
Universidad de Buenos Aires
Intendente Güiraldes 2160
Buenos Aires, Argentina

María A. Arecco
Escuela de Ciencias del Mar
Instituto Universitario Naval, Armada Argentina
Av. Antártida Argentina 821
Buenos Aires, Argentina

Abstract

The total magnetic anomaly (TMA) from a global grid was analysed in order to characterize the magnetic features of the Argentine continental shelf (35ºS to 48ºS) and to expand the current knowledge of such area. TMA amplitudes within the study area were mathematically filtered and enhanced using various techniques including the analytic signal method, the tilt angle method and the second vertical derivative method. In order to estimate the depths of the magnetic sources on the Tona anomaly and the continental edge, the Euler deconvolution method and a 2-D gravimetric inversion model were applied. The TMA filtering results were used to observe and identify large transform zones such as the Río de la Plata system, the Salado, Ventana, Colorado and Malvinas zones, and other minor systems such as the Rawson transform zones. The San José and El Cortijo crustal sutures were also outlined using the applied methods, and it was possible to map and identify a change in orientation of the Ventania-Cape Fold Belt. The tilt angle method revealed high-frequency patterns in the oceanic crust as a result of its volcanic nature. The second vertical derivative method exhibited high-frequency patterns in the G and Tona anomalies, the M-series magnetic anomalies and oceanic bottom alignments, revealing their volcanic and episodic character through a large and complex distribution of blocks at the continental-oceanic boundary. Discontinuous linear magnetic sources were observed along the ancient Dom Feliciano-Lavalleja shear belt, most of which were calculated by Euler deconvolution to be located at depths of approximately 5000–8000 m. On transform zones, inner alignments and continental-oceanic boundaries, few dipoles associated with fault steps and dykes were identified. The sources of the M-series anomalies were located at depths of 8000–12000 m, whereas abundant deeper sources were identified for the Deseado and Somuncurá massifs and the Mar Argentino rise. The Euler deconvolution method was used to calculate a source depth range for the conspicuous Tona anomaly of 8000–20000 m. In addition, a 2-D gravimetric inversion model based on a NE-trending profile was used to identify a mafic body along the Patagonia-Gondwana suture bounded by a sub-surface. This body may be an imbrication of the suture located in basement rocks.

Key words: Argentine Continental Shelf; Patagonia Terrain; Tona Magnetic Anomaly; Crustal Magnetic Interpretations; Marine Geology.

Introduction

The Argentine continental shelf has a number of distinguishing attributes with a structural history characterized by plate breakup, heat flow and magmatic activity, which have shaped its current tectonic features. The study of magnetic anomalies reveals the structural and lithologic complexity of crustal rocks, providing a window into the geological history of various sectors of the continent, mainly ancient deep-crustal formations whose seismic structures are unclear due to subsequent tectonic and metamorphic activity. The total magnetic anomaly (TMA) of an area allows the main crustal structures, faults, dykes, transform zones and edges or contacts to be rapidly located and characterized (Lefort *et al.,* 1988). Therefore, by utilizing the results of filtering techniques, it is possible to analyse the structure of the Argentine continental shelf, the main offshore basin structures and the continental edge.

Several authors have conducted research in this area, including gravimetric studies of the continental-oceanic boundary (Arecco *et al.,* 2016 *a, b*) and magnetic studies of the continental crust (Ghidella *et al.,* 2005, Max *et al.,* 1999). In addition, investigations such as isostatic compensation and geoid undulation studies in the Claromecó basin (Ruiz and Introcaso, 2011), tectonic studies of the El Cortijo suture zone (Chernicoff *et al.,* 2014; Pángaro *et al*., 2011; Pángaro and Ramos, 2012), seismic studies of margin segmentation (Franke *et al*., 2007) and palaeomagnetic studies (Rapalini, 2005) have been carried out, among other authors.

In this paper, TMA amplitudes were mathematically filtered in the study area and enhanced using various techniques including the analytic signal method (AS), the tilt angle method (TDR) and the second vertical derivative method (SVD), each of which has various advantages in different geologic situations. Applying multiple methods to the same anomaly area improved the reliability of the results. In order to calculate the depths of the magnetic sources in the basement and the crust the Euler deconvolution method was used. In addition, with the aim of creating a tectonic model of the Tona magnetic anomaly sources, 2-D gravimetric modelling was performed based on a transverse profile to the anomaly.

The objective of this study was to carry out a regional magnetic survey of the Argentine continental shelf and its continental margins, including the continental-oceanic boundary (COB) up to the oceanic crust between latitudes of approximately 35ºS and 48ºS. The study area was separated into two smaller zones, the northern (35ºS–41ºS) and the southern (41ºS–48ºS). In this work, one source of total magnetic anomaly was used, a newest global grid EMAG2 satellite grid (Meyer *et al.,* 2016).

Geological setting

The regional structural configuration of the Argentine continental shelf is composed of the Río de la Plata craton located southeast of South America, which extends from the Piedra Alta terrane in Uruguay in the north to the Colorado basin in the south (Pankhurst *et al*., 2003; Cingolani, 2011; Pángaro and Ramos, 2012). This craton is bounded to the east by the Dom Feliciano Belt (Fragoso-Cesar, 1980) and further to the south by the COB (Figure 1 A) (Arecco *et al*., 2016 *a*).

The Archean and Proterozoic-age La Plata Craton by gneisses and meta-igneous complexes is characterized (Ramos, 2008). Accretion occurred along its southern margin involving an amalgamated collage of primarily non-magnetic or weakly magnetic sediments and the metamorphic and igneous micro-continent that forms the Patagonia Platform. Large areas of this crust may have been stabilized during Neoproterozoic to early Palaeozoic times (Tankard *et al*., 1995), but compressional tectonics associated with accretion ceased only during the late Gondwanian orogeny, close to the Upper Palaeozoic (Ramos, 1996).

The Río de la Plata Craton comprises a series of continental blocks that, during the Trans-Amazonian orogeny, were amalgamated (Ramos, 1996). It consists of a series of arc granitoids associated with subduction

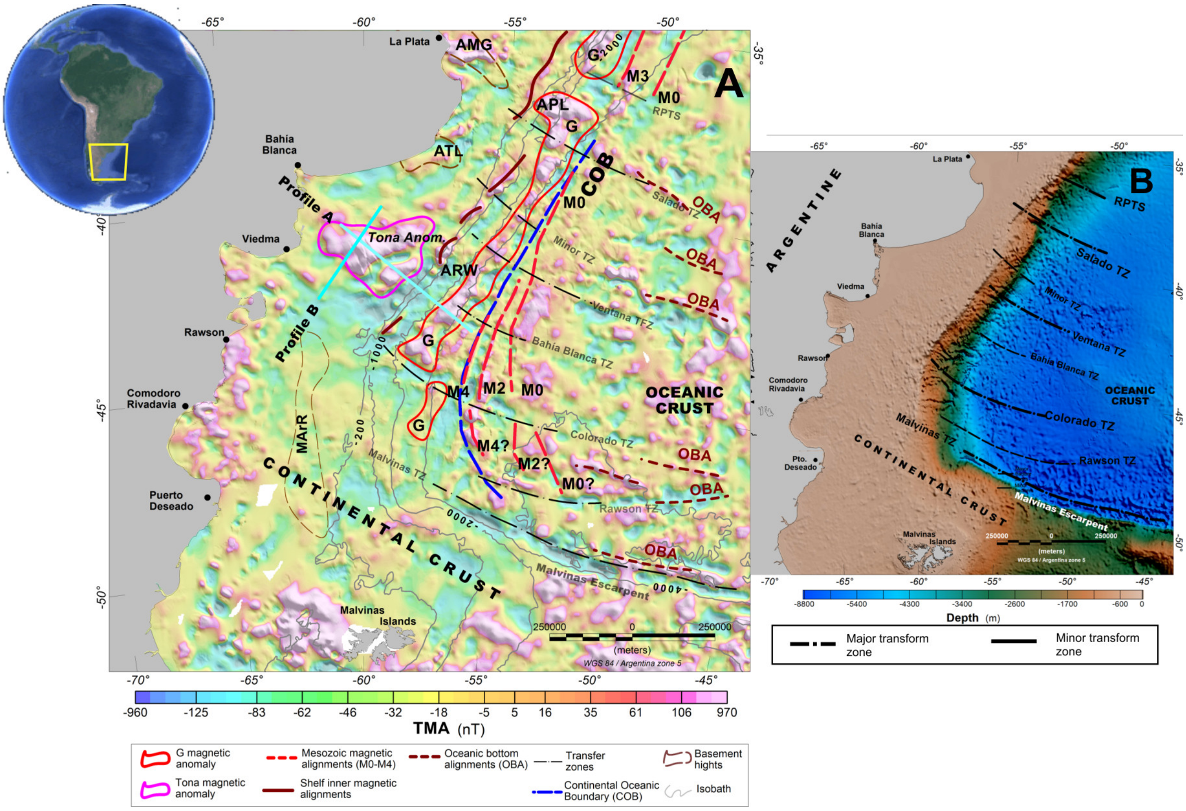

Figure 1. Total-magnetic-field anomaly (TMA) map from the global grid (Meyer *et al*., 2016) (A) and bathymetric global grid map (Amante and Eakins, 2009) (B). In Figure A, the location of profiles through Tona anomaly is marked in cyan lines. TMA map shows the most relevant magnetic anomalies, M0- M4, related to the COB (dashed blue line) and the larger magnetic anomaly, G anomaly (red shut up curve). In Figure B, the main transform zones are depicted. Abbreviations: **COB**: continental–oceanic boundary; **G:** G magnetic anomaly; **M0-M4**: Mesozoic series alignments; **Tona Anom.**: Tona magnetic anomaly; **OBA**: oceanic bottom magnetic alignments; **Salado TZ**: Salado transform zone; **Colorado TZ**: Colorado transform zone; **Rawson TZ**: Rawson transform zone; **Malvinas TZ**: Malvinas transform zone.

preserved in the region of Tandilia (Dalla Salda and Francese, 1985; Dalla Salda, 1987). The granitoid ages range from 2100–1900 Ma in the Tandilia region (Varela *et al*., 1988) (Figure 2). El Cortijo suture runs WNW and is aligned with the northern boundary of the Tandilia terrane (Teruggi *et al.,* 1989, 1988 en el listado de referencias CHECAR;, Cingolani and Dalla Salda, 2000; Cingolani *et al.,* 2010; Chernicoff *et al.,* 2014). At the local scale, El Cortijo suture zone is often E–W-trending. At this scale, WNW-trending tholeiitic dykes (TTD) of Statherian age are seen to cross-cut the Rhyacian El Cortijo suture zone (Chernicoff *et al.,* 2014) (Figure 2). Small magnetic highs that are spatially associated with El Cortijo suture zone are related to unexposed basic ophiolitic bodies related to those present in El Cortijo Formation (Chernicoff *et al.,* 2014).

Several authors have interpreted the presence of a suture related to the collision of the Patagonia terrain (Ramos, 2008; Rapalini, 2005; López de Lucchi *et al.*, 2010, Pángaro and Ramos, 2012) (Figure 2).

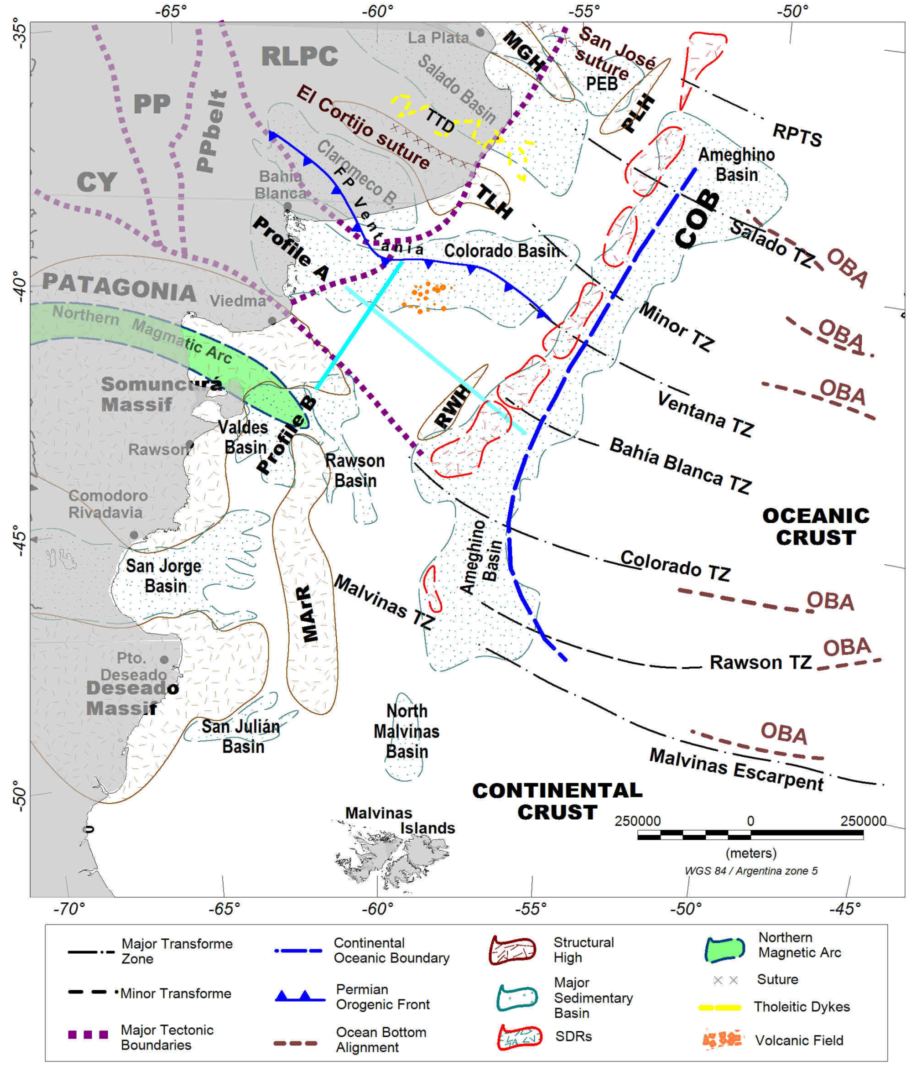

Figure 2. Distribution of the main tectonic structures on the Argentine continental shelf beyond the continental oceanic boundary (COB). The locations of major tectonic boundaries (Pángaro and Ramos, 2012), the Ventania–Cape Fold Belt (Pángaro and Ramos, 2012; Paton *et al.,* 2016), the northern magmatic arc (Ramos, 2008), the COB and oceanic bottom alignments (Arecco *et al*., 2016 *a)*, structural highs and basins (see text for references) are indicated. The main transform zones from Franke *et al*. (2007) and SDR wedges according to Hinz *et al*. (1999) are shown. The Rawson TZ is presented in this work. Abbreviations: **CY**: Cuyania terrain; **PP**: Pampia terrain; **PPbelt**: Pampia belt; **RLPC**: Río de La Plata craton; **Ventania FB**: Ventania Fold Belt; **PEB**: Punta del Este basin; **MGH**: Martín García basement high; **PLH**: del Plata basement high; **TLH**: Tandil basement high; **RWH**: Rawson basement high; **MArR**: Mar Argentino Ridge; **OBA**: ocean bottom alignment.

The passive continental volcanic margin of Argentina began in the Late Jurassic/Early Cretaceous (~130 Ma) during the last stages of fragmentation of the supercontinent Gondwana, which propagated from south to north. This opening lasted from ca. 137 Ma to 126 Ma (Austin and Uchupi, 1982; Rabinowitz and LaBrecque, 1979) and involved a complex combination of rifting and faulting before and during the breakup of Western Gondwana. This continental margin can be considered a lower-plate passive margin type (LPPM) with the upper-plate passive margin (UPPM) corresponding to the conjugate African margin. The main features characterizing the LPPM-type Argentine continental shelf are expansive shelves, coastal plains in the continental terrace, well-developed half-graben systems, external peripheral ridge systems, and a lack of well-developed basic magmatism, and the presence of extensive rhyolitic plateaux (Ramos, 1996).

The Argentina continental shelf, which begins south of the Colorado River, is one of the best-developed rhyolitic plateaux in the world (Ramos, 1996) with rhyolites corresponding to pre-rift or early-rift types associated with passive margins (Malumián and Ramos, 1984; Kay *et al.,* 1989; Ramos, 1996). The Patagonia microplate is considered to have been independent from Gondwana in the Early to Middle Palaeozoic before it underwent a frontal collision with Gondwana in the Late Palaeozoic, producing folding and thrusting at the Sierra de la Ventana fold system, SW of Buenos Aires (Ramos, 1988, 2008; Rapallini, 2005) (Figure 2).

The G anomaly is considered the biggest among anomalies from Atlantic Ocean opening (Rabinowitz and LaBrecque, 1979); it was drawn in red enclosing positive-negative values because the magnetic field is bipolar (Figure 1 A). Older Mesozoic alignments (M4–M0 off the coast of Argentina) from about 130 to 114 Ma and the G anomaly on conjugate margin offsets (Rabinowitz and LaBrecque, 1979) have been identified from the maximum-minimum zones (warm-cold colors) aligned to the continental margin on updated data (Figure 1 A).

The Tona magnetic anomaly (Ghidella *et al*., 1995) has been identified from its triangular shape between 40ºS and 42ºS (Figure 1A). These is one of several features that have been identified in the Argentine continental shelf, along with the Martín García basement high (MGH) and the Tandil (TLH) and Rawson (RWH) high zones as well as inner alignments oriented sub-parallel to the G anomaly, among others. Regarding the Tona magnetic anomaly, Zambrano (1974) and Urien and Zambrano (1974) stated that "the mesozoic eruptives, so widespread in the Patagonia and western Argentina, are not known to occur in the Colorado basin. They appear on the surface, to wedge out near the southern boundary without reaching the basin itself". Pángaro *et al*. (2011) identified two NE-oriented, NW-dipping deeply rooted shear zones that were mapped all the way to the Moho using wide-angle seismic reflection lines. These shear zones lie to the north of the Tona anomaly. The eastern shear zone is associated with a volcanic field composed of presumably hundreds of volcanoes of Late Cretaceous age, and the south ends of both zones lie just above the northern edge of the Tona anomaly, which could be associated with that volcanic field (Figure 2).

According to Max *et al.* (1999), the northern region (35ºS–42ºS) of the continental crust includes the structural magnetic domain of the Río de la Plata craton (RLPC) and the marginal sub-domain of the La Plata (LPDM) domain that was tectonically reworked during accretion (Somuncurá Massif). These authors affirm that the oceanic crust (OC) contains the M-series and a quiet zone of crust. The RLPC comprises a series of continental blocks that were amalgamated during the Trans-Amazonian orogeny. The sutures run subparallel to San José and El Cortijo and separate the continental blocks of Florida, Buenos Aires and Tandil (Dalla Salda *et al.,* 1988; Teruggi *et al.,* 1988; Ramos *et al.,* 1996).

According to Arecco *et al*. (2016 *a, b*) and Pizarro *et al*. (2016) the continental oceanic transition (COT) and the COB have distinguishing tectonic features, as has been shown in its studies, 2D and 3D gravimetric models, above the Argentine basin and continental boundary (Figure 2). Arecco *et al*. (2016 *a*) showed by 2-D gravimetric models that the continental crustal thinning begins on the continental and transitional crust, where the greatest sedimentary thickness are located, the basaltic wedge series (SDRs), the zone of intrusive magmatic dykes, and the underplated body, till the COB. The 3D model results allowed to obtain the boundaries of the Argentina Basin revealing gravimetric aspects related to the morphology and constitution of the upper crust in the continental margin (Pizarro *et al*. 2016).

In addition, a series of marine basins that resulted from the South Atlantic Ocean opening can be observed in the continental shelf. Among the most important of these are the Punta del Este, the Salado, the Claromecó, the Colorado, the Valdés, the Rawson San Jorge and the San Julián basins (Figure 2). The half-graben systems on the shelf are strongly controlled by basement features, allowing the shelf to divide into two distinctive sectors by the Patagonic boundary (Figure 2). The northern region of the Río Colorado Salado, Colorado and Claromecó basins was partially developed on the Río de La Plata Craton in the province of Buenos Aires (Dalla Salda *et al.,* 1988; Franke *et al.,* 2007).

The southern region (40°S–48ºS) of the continental crust includes the Somuncurá and Deseado massifs, the northern magmatic arc (Ramos, 2008), slim SDRs and the Valdes, Rawson, Ameghino and San Jorge basins in front of the COB (Figure 2). The Tona magnetic anomaly is large in amplitude but low in frequency; this is in marked contrast to the magnetic pattern over the southern zone, which includes the San Jorge, Valdés and Rawson basins (Figure 1). According to Ghidella *et al*. (1995), "this anomaly was possibly caused by lava flows through detachment faults formed in the rifting process and that these flows seem to have been accumulated against a barrier imposed perhaps by the implications of the Colorado discontinuity". Most of the magnetic oceanic bottom alignments (OBA) are parallel to the TZs, which coincide with the ocean floor spreading direction. Additionally, the magnetic OBAs coincide with the gravimetric OBAs (Arecco *et al*., 2016 *a*).

Several authors such as Zambrano (1974), Introcaso and Ramos (1984), Tavella and Wright (1996), Fryklund *et al*. (1996) and Introcaso *et al*. (2008) have discussed the geology of these basins, originated during a major rifting event in the Late Jurassic and Early Cretaceous, among others. In the southern region of the Río de la Plata craton is the Gondwanides mountain belt, which was produced as a result of the late Palaeozoic collision of the Patagonia terrane with the continental margin of Gondwana (Ramos *et al.,* 2014) (Figure 2). The southern part of the Colorado River marks the edge of an important area of acid volcanism, but also an area structurally dominated by meridian-parallel half-grabens, as observed in the Valdés and Rawson basins (Marinelli and Franzin, 1996). In the south, transverse structures are found corresponding to the marine section of the San Jorge basin (Baldi and Nevistic, 1996, Sylwan, 2001). The Somuncurá massif adjacent to the shelf contains a series of outcrops of lava and pyroclastic flows of rhyolitic composition associated with granitic porphyry. Recent dating work performed by Riley *et al*. (2016) in rocks from the Marifil Formation yielded similar ages. The northern sector of the Somuncura massif is considered to be a magmatic arc that was active along the northern edge of the plate prior to collision between the Patagonia block with Gondwana (Ramos, 2004, 2008). OBAs in the oceanic crust have been identified from TMA anomalies, as well as from gravimetric anomalies and through the application of enhancement techniques (Arecco *et al.,* 2016 *a, b*).

Methodology

The main TMA magnetic data source is the EMAG2 satellite grid, which is available as a digital file at https://data.noaa.gov/dataset/emag2-earth-magnetic-anomaly-grid-2-arc-minute-resolution (Figure 1 A). These data are available with a grid spacing of 2 arc-min (~ 4 km in the study area). This grid has been compiled from satellite data, ship and airborne magnetic measurements according to Meyer *et al.* (2016).

Enhancement techniques used include the analytic signal (AS), the tilt angle (TDR) and the second vertical derivative (SVD) methods, as well as 3-D Euler deconvolution to obtain the location and depth of the faults or dykes (edges or contacts) of the main tectonic structures. Finally, a 2-D Euler deconvolution, and 2-D gravimetric model were applied on a transverse profile to Tona anomaly for obtaining causative source depth.

Analytic Signal

The 2D technique developed by Nabighian (1972) was applied to magnetic potential fields. The author later generalized the analytic signal (AS) from 2D to 3D (Nabighian, 1984). This technique indicates the relative maxima at the contact between bodies with different magnetic susceptibilities. In particular, the analytic signal module $|AS|$, also termed the total gradient (Nabighian *et al.,* 2005), has been used to detect maxima at the contact between bodies with different magnetic susceptibilities. The amplitude of the $|AS|$ module in 3D is given by (1)

$$|AS| = \sqrt{\frac{dTMA}{dx}^{2} + \frac{dTMA}{dy}^{2} + \frac{dTMA}{dz}^{2}} \quad (1)$$

where $\frac{dTMA}{dx}, \frac{dTMA}{dy}$ are the horizontal derivatives and $\frac{dTMA}{dz}$ is the vertical derivative of the TMA. Each $|AS|$ maximum indicates a contact between bodies of high magnetic susceptibility contrast.

Tilt angle (TDR)

The enhancement technique introduced by Miller and Singh (1994) to detect contacts when applied to the Total Magnetic Field grid (Verduzco *et al.,* 2004) provides greater resolution of the edges with respect to those shown by the AS. This filter is able to detect depth sources masked by high-amplitude interference from superficial magnetized bodies. The tilt angle (TDR) is given by expression (2)

$$TDR = \tan^{-1} \frac{VDR}{THDR} \tag{2}$$

where VDR and THDR are the first horizontal and the vertical derivative of the TMA, respectively (Verduzco *et al.,* 2004). A TDR value of zero indicates an edge or contact. Due to the nature of the tangent function, all resulting angles are in the range between $-\pi/2$ and $\pi/2$ (Cooper and Cowan 2006), so that the details of other contacts whose angles are not close to zero are lost.

Second vertical derivative

The second vertical derivative (SVD) is the vertical gradient of the first vertical derivative, which is physically equivalent to measuring the magnetic field simultaneously at two vertical points, one above the other, by subtracting the respective values and dividing the result by the vertical spatial separation between the measuring points (Blakely, 1996). In the wavenumber domain, the 2nd-order vertical derivative is given by (3)

$$A' = A(k)\left|k\right|^2 \tag{3}$$

where *A(k)* is the amplitude at a wavenumber *k* ($k = 2\pi/\lambda$) and λ is the wavelength (Blakely, 1996). The result enhances relatively high frequencies in contrast to low frequencies. The vertical derivative exaggerates the signal of the upper-level sources producing magnetic anomalies. This property is the basis for applying the derivative, which eliminates the regional effects of long wavelengths and enhances the effects of shallow surface bodies. Implementation of the second vertical derivative requires good quality data as the enhancement of high frequencies may result in increased noise (Milligan and Gunn, 1997).

Euler deconvolution method

The Euler deconvolution method provides the location and depth of the magnetic source tops. The Euler deconvolution method for estimating the depths of magnetic sources is based on the concept that magnetic fields are homogeneous functions of the source coordinates and therefore satisfy the Euler equation. This equation can therefore be solved parametrically to determine the source locations. This method has found widespread application as the theoretical basis for the inversion of large magnetic and gravity data sets in terms of simple sources in the shape of steps, spheres or cylinders (Thompson, 1982; Reid *et al.,* 1990; 2003; Salem and Smith, 2005). When the structural index and estimated depth are combined with geologic information, they can be used to identify and estimate the depths of a wide variety of geologic structures such as faults, magnetic contacts, dykes and extrusions, among others (Thompson, 1982).

The Euler deconvolution method is based on the Euler homogeneity equation, which can be written in 2D in the form

$$\left(x - x_0\right)\frac{\partial TMA}{\partial x} + \left(z - z_0\right)\frac{\partial TMA}{\partial z} + \eta TMA = 0 \tag{4}$$

where the total magnetic field anomaly (*TMA*) is due to a magnetic source located at (x_0, z_0) and η is a structural index (SI) (Table 1) related to the simple source geometry. The only unknown quantities in equation (4) are x_0, z_0 and η. The depth and location along the profile are represented by the coordinates while η represents the type of source.

To solve Euler's equation, horizontal and vertical potential field gradients are required, which were calculated in the frequency domain (Gunn, 1975). It has been observed that depth estimates that are obtained from magnetic data are more accurate if the reduced to pole (RTP) magnetic field is used (Thomson, 1982).

Table 1. Structural indices in 2D and more common symbols used to represent the indices.

Structural index	Simple model	Symbol
1.0	Fault or contact	+
2.0	dike	×
2.5	dipoles	□
3.0	sphere	^

2-D model inversion

In spite of ambiguity that the inversion of the gravimetry presents, for the construction of a tectonic model, the realization of tectonic models based on the inversion of gravimetric models is efficient. To overcome the non-uniqueness problem, it is possible to invert gravimetric data with a priori information about the crustal structure to provide additional constraints, such as discontinuities from seismic refraction studies or seismic horizons interpreted from multichannel seismic profiles (Nabighian *et al*., 2005). In the inversion performed for the 2-D gravimetric model in this study, a structure based on simple crustal blocks was assumed, from previous works (Pángaro and Ramos, 2012; Ramos *et al*., 2014). For this purpose the Grav-Modeler program, based on Talwani *et al*. (1959) and developed by the Geotools software division of AOA Geophysics Inc. and Lacoste & Romberg, was used.

Results

The differences in magnetic susceptibility of structures such as faults or steps, dykes or sills generate different magnetic responses. For the purpose of differentiate geological structures in the crystalline basement and upper crust enhancement techniques of magnetic anomalies were used. In order to display the results more clearly, the study area was divided into two zones (35ºS–42ºS and 40°S–48ºS) as shown in Figures 3, 4 and 5. The results of the 3-D Euler deconvolution can be seen in Figure 6. Additionally, in order to identify the sources responsible for the Tona anomaly, two cross-sectional profiles, A and B, were made. Profile A was oriented in the NW–SE direction and was processed by an Euler deconvolution performed in 2D (Figure 7). Profile B was made in the NE–SW direction, and was used to create a 2-D gravimetric model (Figure 8).

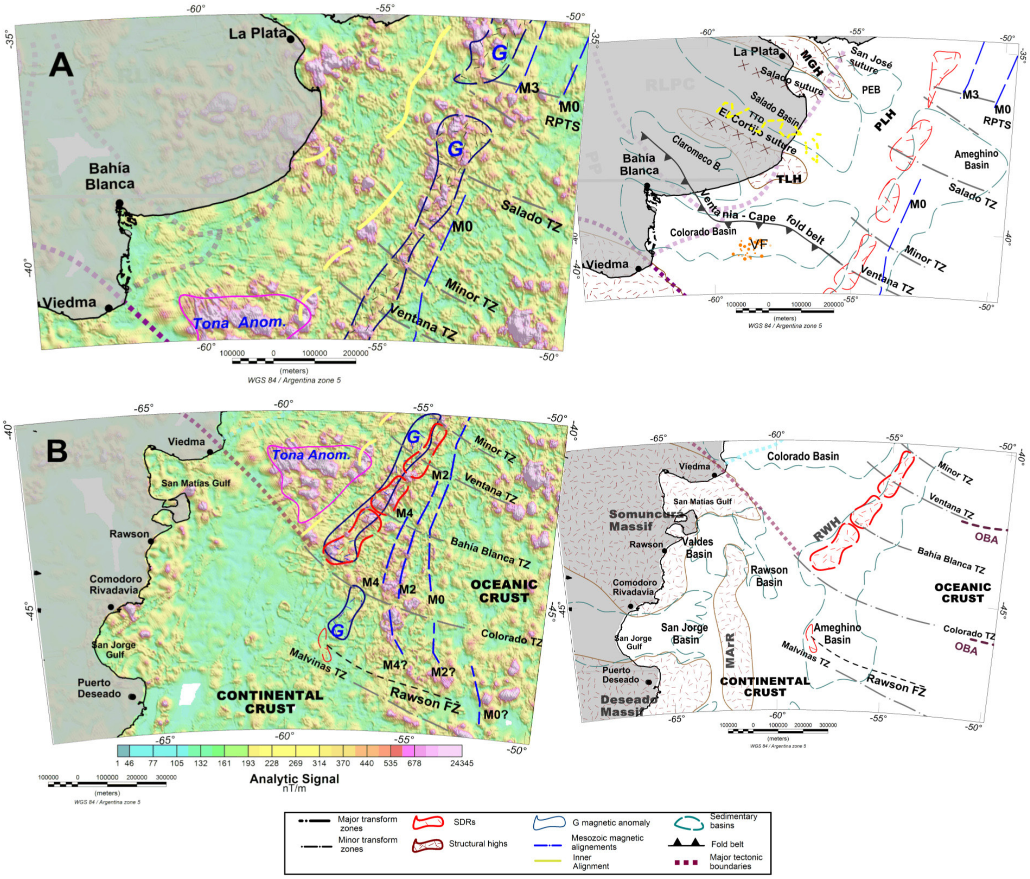

Figure 3. Analytic signal maps of the northern zone (A) and the southern zone (B). The respective geologic maps are located to the right of the AS maps. The Rawson transfer zone is enhanced and presented in the analytic signal map. Magnetic alignments were identified using enhancement techniques. For references of geological structures, see the title Geological setting. Abbreviations: **RPTS:** Río de la Plata Transform System; **VF:** volcanic field; **PLH:** del Plata high; **MArR:** Mar Argentino Ridge; **TTD:** tholeiitic dykes; **OBA:** ocean bottom alignments. For others references see Figures 1 and 2.

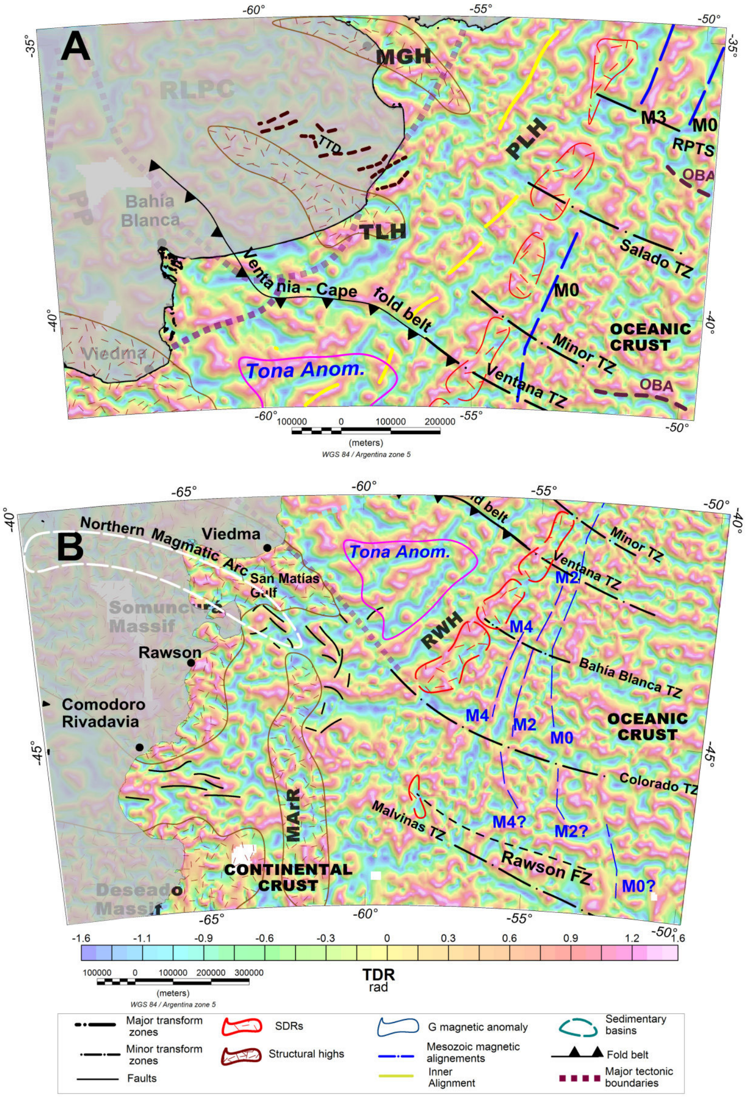

Figure 4. Tilt angle (TDR) maps of the northern zone (A) and the southern zone (B). In the northern zone, various boundaries are enhanced by TDR because the null values indicated edges, as the southern edge of the Colorado basin, the Tandil High, the THD and inner alignments. In the southern zone, the tilt angle enhances the Minor Transform transform zones and some faults in the Valdés, Rawson and San Jorge basins. Abbreviation: **TTD:** tholeiitic dykes. For others references see Figures 1 and 2.

Analytic signal

The analytic signal shows the magnetic contact responses by high values (magenta) (Figures 3 A; B). Structures associated with crystalline basement such as the Martín García and Rawson basement highs can been seen, while the Tandil basement high appears less distinct. In addition, the AS depicts an eastward shift of the G anomaly in the Río de La Plata Transform System zone understanding of a control of system about G anomaly (Figure 3A). The Tona anomaly appears as a triangular magnetic high with its somewhat subparallel edge to the magnetic G anomaly to the east, Patagonia boundary to the south and Colorado Basin to the north. Note that, the Tona anomaly exhibits long wavelengths that prevail over short wavelengths, i.e. its sources probably are deep. In Figure 3B, alternating alignments with very high values (magenta) and low values (green) can be identified subparallel to the continental margin representing the Mesozoic seafloor spreading alignments M0–M4 (Rabinovich and LaBrecque, 1979). A detailed analysis of the analytic signal map (AS) corresponding to the northern region shows NE–SW alignments with high values between 1000 and 500 nT/m corresponding to the continental edge (Figure 3A).

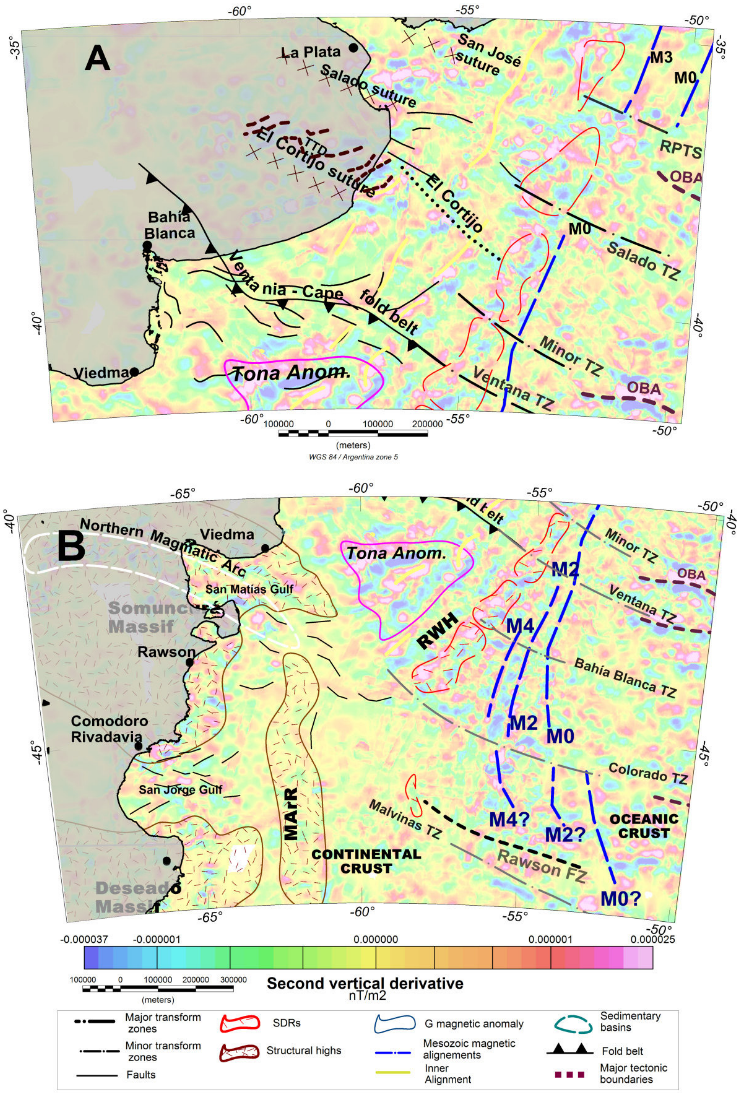

Figure 5. Second vertical derivative (SVD) map of the northern zone (A) and the southern zone (B). In the northern zone, a pattern of high frequency is seen in the continental crust, such as in the basement high of the Martin García and Tandil basins, and in the areas of the G and Tona anomalies and the TTD. SVD exhibits a rough and broken pattern in areas of the oceanic crust such as the Mesozoic alignments and the OBA. Abbreviation: **TTD:** tholeiitic dykes. For others references see Figures 1 and 2.

The Salado basin is described as aulacogenic rift basin, and exhibits a NW–SE-oriented fault pattern (Ramos, 1996; Urien and Zambrano, 1974) (Figure 3 A). The southern edge displays different values ranging from 200 to 800 nT/m, while the northern edge borders the Martín García Precambrian outcrop threshold (Ramos, 1996; Urien and Zambrano, 1974) reaching values up to 1000 nT/m. The eastern edge is represented by a series of faults in the Plata High (Ramos, 1996) with values of up to 1200 nT/m. The AS shows that the Martín García basement high controls the features of the Salado and Punta del Este basins (Ramos, 1996). The north slope of the Punta del Este basin is controlled by WNW-ESE alignements orientated parallel to the San José suture (Ramos, 1996), which is bounded to the east by the G magnetic anomaly and to the north by the Martín García basement high.

North of El Cortijo suture in the continental zone, the AS reveals a sheet-complex with a NW–SE orientation controlled by the Salado transform zone. This area of WNW-trending tholeiitic dykes (TTD) (Chernicoff *et al.*, 2014) extends towards the shelf and beyond the coast and changes to a predominantly N–S orientation due to a rotation associated with the onset of the

Figure 6. 3-D Euler deconvolution fault maps of the northern zone (A) and the southern zone (B). Depths of the faults are represented by green circles. The circle's size is related to the depth of the source. Abbreviation: **SI:** structural index. For others references see Figures 1 and 2.

South Atlantic opening (yellow lines) (Figure 3 A). In contrast, parallel to the Salado transform zone (Salado TZ) and the Río de la Plata system (RPTS), the AS displays thin transform zones that influence most of the G anomaly, as can be seen in the Minor TZ and the Patagonia-Gondwana suture.

On the southern edge of the Colorado Basin, the AS displays higher values in the range of 1200–2000 nT/m (warm colors), which reveal the deepest volcanic sources coinciding with the Tona magnetic anomaly to the northeastern of the Somuncurá massif. The Tona anomaly borders a volcanic basement high comprised of deep volcanic rocks, so the amplitude of the SA indicates a deep souce of the volcanic field toward the ocean bottom.. The offshore Somuncurá Massif on the continental shelf (Ramos, 1996) has similar characteristics to the onland Somuncurá Massif, which is part of Patagonia (Río Negro and central Chubut). Therefore, the Tona anomaly represents the boundary of the offshore massif on the continental shelf. This massif contains a series of outcrops of lava and pyroclastic rhyolitic flows associated with granitic porphyries. Given its lateral extent of several hundred kilometers in diameter, the formation of this massif could be related to asthenospheric hot-spot activity that partially melted the upper crust during an extensive period of pre-rift magmatism associated with the initial opening of Southern Atlantic (Rapella and Pankhurst, 1993).

The Rawson structural high (RWH), which controls the southeastern edge of the Colorado Basin, reaches values of 2000 nT/m. The western edge of the Colorado basin is parallel to the continental edge, with structural highs reaching values from 800 to 1000 nT/m. The northern edge of this basin exhibits values of 100 to 200 nT/m (cold colours), whereas the submerged area in front of the coast between Bahia Blanca and Viedma exhibits the lowest values in the study area, around 50 nT/m. Low anomalies are seen along the northern edge because this area is in contact with the Palaeozoic Claromecó basin, which is a sediment-sediment transition rather than the sediment-intrusive transition seen in the south and the east (Ruiz and Introcaso, 2011).

The more prominent features in the southern region (Figure 3B) include the Somuncurá and Deseado massifs, Mesozoic magnetic anomalies and the Malvinas transform zone. These features display values from 1500 to 2000 nT/m. In this region the G magnetic alignment is sub-parallel to the continental edge and is interrupted at 44ºS and at 45ºS by the Colorado TZ and the Rawson TZ, respectively. An arc-shaped high-frequency pattern with a primaryily E–W orientation (~41ºS) can be identified from the continent to the Golfo San Matías, which is then interrupted by the Colorado TZ (Figure 3B).

The N and S edges of the San Jorge basin exhibit the highest values in the basin, reaching approximately 400 nT/m. No information for the eastern edge of the basin is available. The AS indicates that the features at the edges of these basins are controlled to the north by the Somuncurá massif, to the east by the Colorado TZ and in between by the Mar Argentino Ridge (MArR) (Rolleri, 1972). The AS does not show the extensive faulting typical of basins formed in the mid-to-late Jurasic during rifting between South America and Africa. A fan pattern can be observed in the magnetic alignments, along with a shift to the east due to the opening of the South Atlantic Ocean. The Rawson transform zone extends eastward parallel to the Colorado Transform zone in the south. This transform zone controls the Mesozoic alignments (M4 and M2) north of the Malvinas Transform zone.

Tilt angle

The tilt map resulted in improved determination of edges, contacts or faults identified in the AS, such as the basin axis extension, the shape and extension of sutures, the El Cortijo TZ and minor and the RPTS (Figure 4A). The tilt angle can discriminate between oceanic and continental crust by the high-frequency pattern in oceanic crust. The tilt angle map of the northern zone delineates various sources and provides information about the northern and southern edges of the Punta del Este basin. In addition, the southern and eastern edges of the Colorado basin are clearly marked, as well as the southern edge of the Claromecó basin. Moreover, the basin axes of the Punta del Este, Salado and Claromecó basins can be clearly observed. In the oceanic crust, TDR enables identification of the M3 alignment, although TDR does not allow OBAs to be clearly identified (Arecco *et al.,* 2016 *a*). However, the TDR application did enhance the outline and extension of El Cortijo suture from the continental shelf to the edge through its influence on the G anomaly. Furthermore, high frequencies on the inner side allowed identification of fractured blocks as a result of the amalgamation of the continental blocks that comprise the suture surrounded by the extended El Cortijo suture to the NW. El Cortijo suture is highlighted in the WNW–ESE direction in the TDR map, along with TTD of Statherian age. The Patagonia-Gondwana suture is clearly demarcated up to the G anomaly and the tilt angle map shows oblique alignments in the general direction of the Patagonia terrain tectonic edge. Between the G anomaly and the shoreline, inner alignments sub-parallel to the margin can be seen that are controlled by the Salado, Ventana and minor transform. These inner alignments were probably activated by the opening of the South Atlantic Ocean.

In the southern area, null values are observed along the eastern and southern edges of the San Jorge Basin, and the northern and southern edges of the Rawson and Valdés basins are clearly marked (Figure 4B). Using this enhancement technique, the magnetic G anomaly and the NE–SW-orientated parallel magnetic alignments M4, M2 and M0 can be recognised as high-frequency alignments. South of the Colorado TZ, an eastward shift in these main alignments can be observed where the G prolongation is clearly identifiable by the change to a N–S orientation. Similarly, a change in the orientation of the Mesozoic M4, M2 and M0 alignments can be observed parallel to G (Figure 4B). Above this continental crust, the Rawson TZ is seen to limit the southward continuation of the G anomaly as well as that of the Mesozoic magnetic alignements running parallel to the Colorado TZ and the Malvinas TZ (Figure 4B). Therefore it can be concluded that the Rawson TZ was activated during the opening of the Atlantic Ocean. Above the oceanic crust, oceanic bottom alignements (OBA) can be identified, thus confirming the expansion direction in the oceanic bottom region (together with the orientation of transform zones).

Second vertical derivative

The main features highlighted in the results of the SVD implementation are associations between weak zones, like cortical faults (San José and El Cortijo sutures), or the magmatic arc in the Nordpatagonic massif (Figures 5A and 5B). Magnetic fabric edges are highlighted by a high-frequency pattern, as in the G and Tona anomalies. Additionally, it was possible to distinguish two types of organization in the patterns of the SVD frequencies between the continental and the oceanic crust. In the oceanic crust, a magnetic fabric with high-frequency patterns was observed with particularly clear alignments subparallel to the edges such as in the G, M0, M2 and M4 alignments. These are crossed by transform zones perpendicular to the crustal boundary, some of which are associated with transform zones (Salado and Colorado TZ). A heterogeneous fabric was observed in the continental crust, where low-frequency patterns are associated with large structures.

In the Tona anomaly, the magnetic fabrics appear as a series of maxima and minima alignments with NE–SW orientations. Intrusive dykes of magmatic material can be better seen in the NW–SE profile across the Tona anomaly (Figure 7). To the north of the Salado basin, the SVD depicts the edges of the Martín Garcia Precambrian basement by a high-frequency pattern (Figure 5A). As seen in the analytic signal (AS), the high-frequency pattern in the G anomaly is interrupted by the RPTS, while in the SVD map, a group of contacts displaced to the east were observed that were likely activated during the Atlantic Ocean opening (Figure 6A).

The SVD map allows TTD contacts of the Statherian age to be clearly identified due to a greater contrast between alignments running transverse to El Cortijo suture, which are bounded to the North by the Salado basin and to the South by the Tandil Highs (TLH) (Figure 5A). In the southern area (Figure 5B), the SVD highlights the G anomaly, M0–M4 and the Somuncurá massif contacts as a pattern of high frequencies. These fan-shaped Mesozoic series alignments appear to be bounded to the south by the Colorado TZ, while in the southern Colorado TZ the G anomaly and Mesozoic alignments M0–M4 appear as a disorganized high-frequency pattern strongly controlled in between by the Colorado TZ and tge Rawson TZ, which is not visible in the AS and TDR maps. In the southern area (Figure 5B), SVD allows the contact between the western edge of the Rawson basin and the Precambrian basement of the Mar Argentino ridge (MArR) to be seen, as well as contacts underlying failed rift structures.

Although all the techniques of highlight identified the edges or contact magnetic sources, the Second Vertical Derivative, highlighted them with higher resolution.

3-D Euler deconvolution results

A 3-D Euler standard deconvolution was applied to the magnetic field anomalies in order to provide information about the location and depth of faults and dykes or sills. For the study area, the Euler deconvolution was calculated with two structural indices (SI), SI=0 and SI=1, which correspond to faults and dykes or sills respectively. It was calculated with window sizes of 5000, 12000 and 20000 m, and all depth solutions with error estimate smaller than 15 % tolerance were accepted using the algorithm of Extended Euler provided by GETECH based on Mushayandebvu *et al*. (2001).

Euler's solutions are represented as circles, faults (green circles) and dykes (orange circles); the circle's diameter is related to the depth of the source, the greater the diameter, the bigger the depth (Figure 6).

The deepest faults, between 14,000 and 18,000 m depth, appear where the opening tectonic movement left the most evident features such as, to the north, in the M0 and M3 mesozoic magnetic alignment zones, and in the transform zone of the Salado and in the Río de la Plata transform system (RPTS) (Figure 6). Others, as deep as the previous ones, occurred within the basins of Salado, Colorado, Rawson, Valdés and San Jorge, confirming their stretching patterns (Figure 6). Along the Rawson Basin, the Ventania-Cape fold belt and the Tona anomaly, there are faults or steps, perhaps denoting the accretion of the Patagonia to Gondwana terrain around 8000 m deep. Steps less than 6000 m deep are visible in the Martín García, del Plata and Tandil basament highs, while in the Rawson high they reached more than 14000 m (Figure 6). Traces of tectonic activity are denoted in San Jose and El Cortijo sutures, and other faults or steps less than 2000 m in the Punta del Este basin (PEB), and scattered solutions indicate the eastern edges of these basins at approximately 1500–2500 m (Figure 6).

The dykes reveal volcanic activity, so it is consistent to find solutions in areas such as sea floor expansion or transform zones. In this work dike's solutions or sills were found very deep to more than 14000 m deep, that probably are associated to the zones of opening of the South Atlantic Ocean, like the alignments of the Mesozoic M0-M4, and to the basaltic wedges SDR. Also, there are numerous dykes at 10000 -12000 m, in the Northern Magmatic Arc, Somuncurá massif, the zone of the Tona anomaly and basament high, this last separates the Valdés and Rawson basins.

Most dyke solutions are very deep at around 10000–16000 m below sea level. Few solutions reach 3500 m. Dyke solutions located in the continental crust such as the G anomaly next to the Republic of Uruguay, the areas south of the Tandil high and in the Colorado, Claromecó and Salado basins and the Tona anomaly reach 14000 m (Figure 7A). Estimated source depths in the Somuncura massif, the Northern Magmatic Arc (Ramos, 2008) and the MArR reach ~16000 m (Figure 7).

Numerous solutions are present at 40ºS–48ºS near the Mesozoic magnetic alignments (M0, M2 and M4) between depths of 11000 and 8500 m, corresponding to the magnetic fabric of seafloor spreading. These solutions agree with the high-frequency patterns in the SVD map. They seem to be controlled by minor, Ventana, Rawson, Colorado and Malvinas transform zones (Figure 7A).

Inside the San Jorge, Rawson and Valdes basins, some faults were detected at various depths from 500 to 2000 m. Deeper sources can be observed in the Deseado massif at 3500 m depth (Figure 7B).

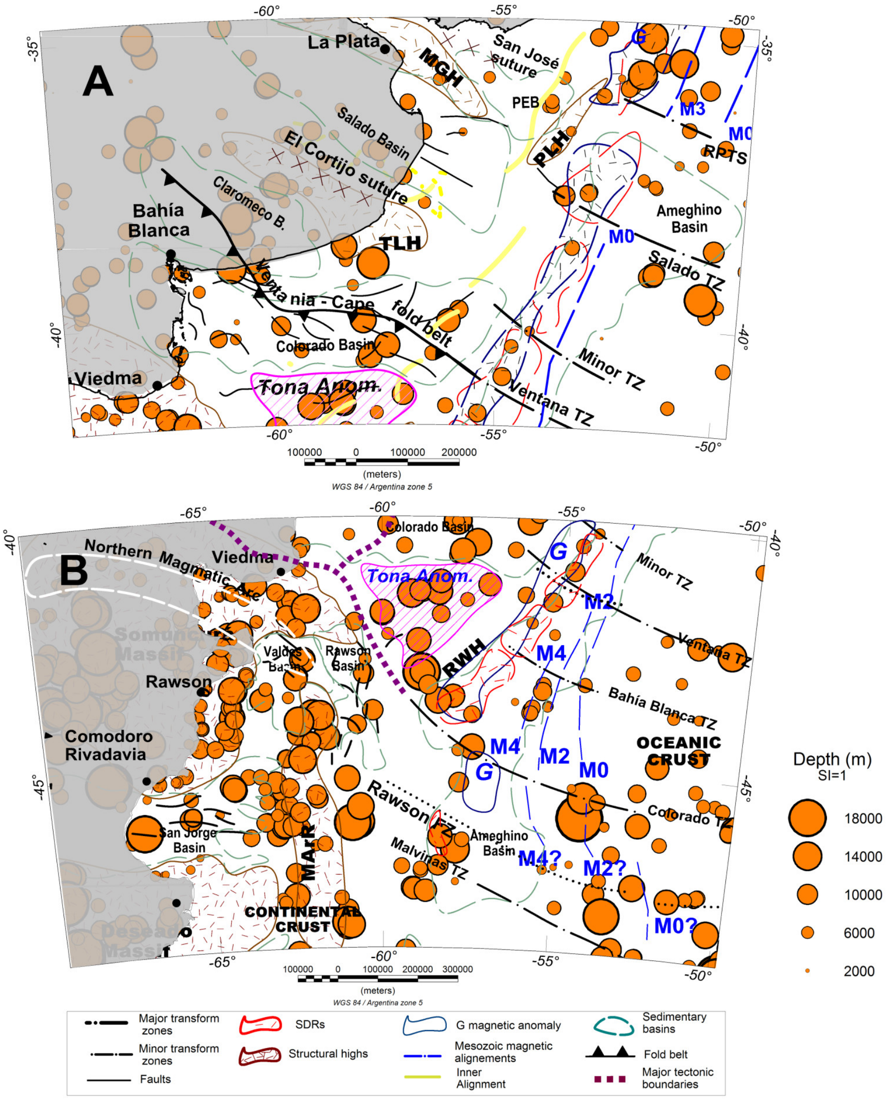

Figure 7. 3-D Euler deconvolution dyke maps of the northern zone (A) and the southern zone (B). Depths of the dykes are represented by orange circles. The circle size is related to the depth of the source. Abbreviation: **SI:** structural index. For others references see Figures 1 and 2.

However, it should be noticed that the Euler source faults are the result of a simple mathematical model and do not necessarily indicate the presence of real geological faults or contacts, for example, in the sea sources deeper than 12000 m. Consequently, it should be taken into account that all Euler calculations only depict real distributions of magnetic material in those cases supported by geological and geophysical models such as basement highs, volcanism or basaltic flows.

2-D Euler deconvolution of Tona anomaly

In order to perform a detailed analysis of the structures comprising the Tona anomaly and the G anomaly up to the COT (profile A, see location in Figure 1A) a 2-D Euler deconvolution was applied. To find the solutions corresponding to faults or steps and dykes or sills, the equation of Euler's deconvolution in 2D was solved using the software presented by Durrehim and Cooper (1998). The structural indices used were, SI= 1 and SI= 2 with windows of 7000, 9000 and 15000 m; the faults and the dykes were identified by the (+) and (×) symbols respectively.

The TMA (black line) and the reduction to pole (RTP) profiles (red dashed line) are shown in the top of Figure 8 from which the zones of the Tona magnetic anomaly and the G magnetic anomaly (green arrows) were identified. The lower part of the figure shows the calculated solutions for faults (+) and dykes (×). In addition, the locations encased in green ellipses, solutions associated with the subplated bodies were marked and within the yellow ellipses, the dykes related to the base of the SDRs were identified in the COT zone. Besides, the solutions, such as contacts with the SDRs (1000 - 5000 m) or basement highs (2000 - 5000 m) coincided with seismic studies (Hinz *et al*., 1999).

The Euler solutions interpreted were calculated considering a window width of 7000 m, as shown in the lower part of Figure 8. Most of the shallow solutions under the Tona magnetic anomaly, are located at 1000 m depth, in coincidence with the crystalline basement according to Ewing *et al*. (1963). However, considering the amplitude and wavelength of the reduction to the pole, the most probable solutions are the deepest ones, greater than 10000 m depth.

Moreover, the observed solutions between 1000 and 10000 m depth are associated with dykes and intra crustal chimneys of volcanic material caused by lava flows that filtered up towards the seafloor due to greater tectonic activity.

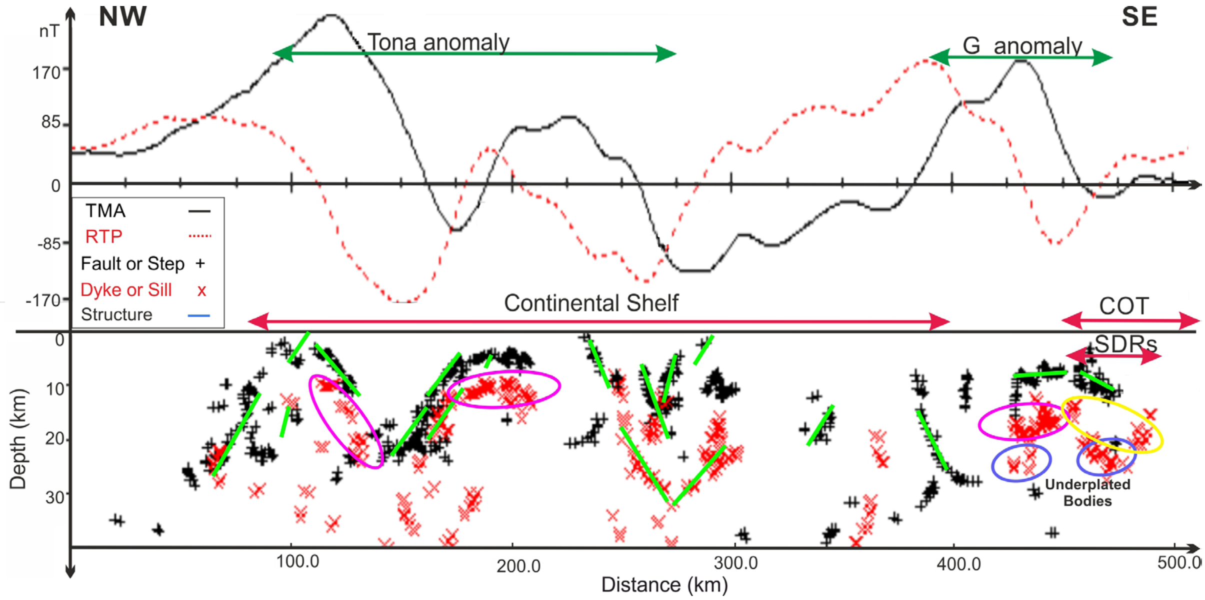

Figure 8. Profile A through the Tona anomaly and the G anomaly. Upper part: TMA and RTP are shown. Lower part: Euler deconvolution solutions are interpreted. The interpreted green lines show the solutions of likely faults and dykes. Ellipses show particular structures, such as underbodies (in blue), feeding dykes zone (in yellow) or dykes/sills under Tona and G anomalies (in magenta). Abbreviations: **COT:** continental oceanic transition; **SDRs:** seaward-dipping reflector series (see location of profile A in Figure 1A).

2-D gravimetric inversion model of Tona anomaly

The 2-D gravimetric model, applied to the Tona anomaly's area of influence (profile B, see location in Figure 1A), was a technique that contributed to the explanation of the causative sources of the conspicuous Tona anomaly. Together with the magnetic field analyses it was used to deduce the tectonic conformation of the Patagonia Suture (Figures 9 A; B). To overcome the non-uniqueness problem, a 2-D gravimetric inversion model can be applied with a priori crustal structure information as a constraint. This 2-D gravimetric inversion model is taken from a structural cross section of the Gondwanides of northern Patagonia, taken from a small portion of a study of the Palaeozoic Ventania System (Ramos *et al.*, 2014). The interland region developed in the present-day Somuncurá massif with exhumed late Palaeozoic arc-granitoids is shown, as well as the Ventania System with its fold and thrust belt and the associated Colorado basin. The lower part of Figure 9B shows the magnetic profile (black line), the observed gravimetric profile (green circles) and the calculated profile (blue line). The lower part of Figure 9 shows the 2-D gravimetric inversion model. This model represents a new interpretation of the blocks that may generate the Tona anomaly.

From left to right in the 2-D model are the continental block of Patagonia and the ancient suture with the Gondwana continent (Patagonia-Gondwana suture). Downwards, the 2-D model displays alternating large sedimentary layers termed Palaeozoic sediments (possible

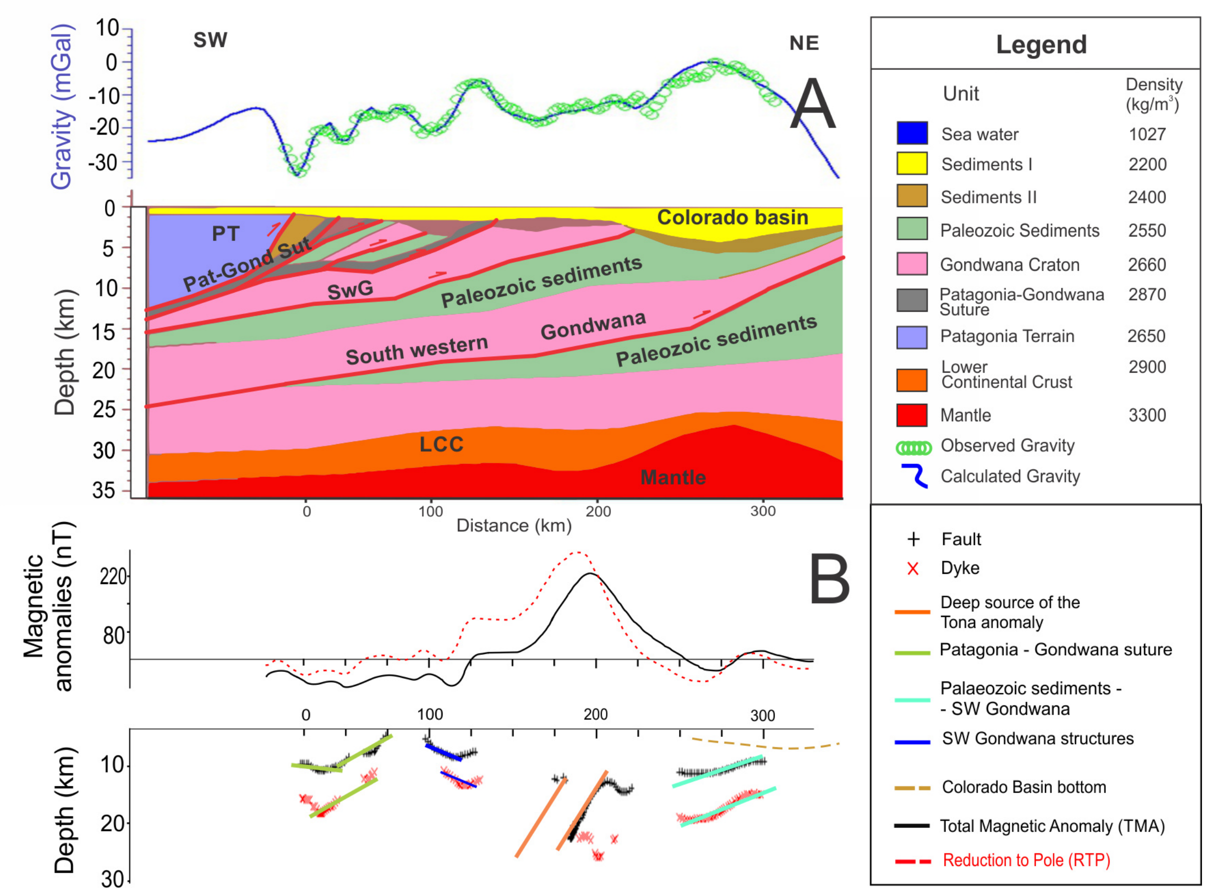

Figure 9. Profile B through the Tona anomaly. 2-D gravimetric model (A) and magnetic deconvolution (B). In Figure A, the observed free air anomaly (green circles) and calculated gravity (blue line) were depicted on top. The gravimetric model's rms is ±2.5 mGal. The density values used in the 2-D gravimetric model are listed in the legend. Red lines highlight the contours of the failed Patagonian suture (see profile B location in Figure 1A). In Figure B, Euler deconvolution solutions, contacts/faults by (+) and dykes/sills by (x) are represented. The interpreted lines are according to failures Patagonia-Gondwana Suture and others failures. Abbreviations: **PT:** Patagonia Terrain; **Pat-Gond Sut:** Patagonia-Gondwana suture; **SwG:** South western Gondwana; **LCC:** Lower continental crust.

accretionary wedges) and detachment faults generated during the accretion phase. The 2-D gravimetric inversion model indicates the presence of a sub-horizontal dyke of volcanic material from the Patagonia-Gondwana suture running parallel to detachment faults that formed during the Patagonia accretion process

The deconvolution of Euler 2-D, applied to the throught profile (profile B) to the magnetic anomaly Tona contributed to obtain the depth of the causative structures (faults and dykes) under the area of influence of the conspicuous Tona anomaly. This method, joint with the 2-D gravimetric inversion, allowed finding a sustainable model of the deep structures of the Tona anomaly.

The gravimetric profile shows a high on the Colorado basin, which is produced by the rise of Mohorovičić discontinuity. The density contrast between the continental crust and the mantle is enough to provoke it. This phenomenon has been studied by Introcaso (1980, 2003) in the Salado and Colorado aulacogenic basins.

Conclusions

The magnetic method presented here, based on a combination of enhancement techniques and 3-D Euler deconvolution, have been used for rapid identification of the main structures on the Argentine continental shelf between 35ºS–48ºS. In addition, 2D studies were used to determine the depths of the blocks that generate the Tona anomaly.

The older Mesozoic alignment series (M4–M0) off Argentina (from ~130 to 114 Ma) and the G anomaly were identified and re-mapped according to modern data. By using techniques applied to TMA in oceanic crust, OBA, major transform zones, minor transform zones and new transform zone such as the Rawson was able to be accurately identified. The use of different techniques, including 3-D Euler standard deconvolution, allowed to highlight various aspects of each of these structures, such as the shallowness, depth, size, trend and extension. 3-D Euler deconvolution provided the depths of the causative sources of the features such as TTD, crystalline basement highs, the Tona anomaly, inner alignments main faults and some basin edges were accurately identified on the Argentine continental crust.

Both the AS and TDR clearly displayed contacts between the highest magnetic susceptibility contrasts such as the G anomaly, which is controlled by the RPTS, Salado, and Colorado transform zones as a result of Gondwana break-up. By applying AS, TDR and SVD it was possible to view the individual M-series features more distinctly between the Colorado and Rawson transform zones in the area from 35ºS to 42ºS. This separation results from extension during the break-up of Gondwana. Moreover, on the TDR and AS maps some basin contours were defined very efficiently, and as well as the main transform zones (Salado, Colorado, Ventana), minor transform zone (Rawson), and structural highs such as the Martín García, Tandil, del Plata, Rawson and Mar Argentino Rise were similarly effectively imaged.

Another key result of this study is the expression of the Palaeozoic Northern Magmatic arc of Patagonia based on the analytical signal and tilt angle. This late Palaeozoic arc is related to northward displacement of the Patagonia terrain prior to its collision with western Gondwana. This zone of weakness controlled the inception of the offshore Colorado basin during Mesozoic times and may have controlled the extension of the Colorado transform zone into the oceanic crust.

These results agree with previous studies based on seismic and gravimetric methods conducted in the Argentine continental passive volcanic margin region; for example, the delineation of the continental shelf edge by significant volcanic activity evidenced by the series of SDR wedges. These were identified in all the techniques employed and were especially marked in the 2-D Euler deconvolution solutions, which indicated SDR depths between 7000 and 9000 m according to Hinz *et al.* (1999).

The results, from the standard Euler 3-D deconvolution, provided information above the distribution of the deep faults in the Ventania-Cape fold-belt, that presented faults whose depth reached 6000-8000 m and dykes or sills around 14000 m deep; these probably are associated to the zones of accretion with Gondwana. Along the western edge of the Ameghino basin, both faults and dykes achieve depths from 2000 to 8000 m. These results are in good agreement with SVD as they display high-frequency patterns in the G anomaly and in the COT (depths from 2000 to 2500 m). In the Plata and Tandil basement highs the faults depths range from approximately 6000 to 10000 m. Moreover, the SDV and 3-D Euler deconvolution results were found to coincide because deeper sources (10000–14000 m) were calculated from the 3-D-Euler deconvolution in areas where the SDV exhibits high-frequency patterns, such as the G and Tona anomalies, the M series, the Martín García and Tandil basement highs and the Somuncurá massif. This can be clearly seen in the northern magmatic arc and the inner alignments in some OBA. El Cortijo and Tandil sutures have some dykes and faults solutions deeper than 3000 m. These dykes are generally depicted in the results of all enhancement techniques.

In the Tona anomaly, the 2-D Euler deconvolution displayed few sources sub-parallel to the south edge of the Colorado basin for SI=0 and 1. However, sources sub-parallel to the continental edge displayed high frequencies, indicating deep sources, while the COT exhibited scattered high-frequency patterns.

The Tona anomaly is visible on the TDR map as the combined product of a deep source and a shallow one. One of them lies parallel to the margin and the other is parallel to the southern edge of the Colorado basin. The application of the Euler method to a 2-D profile revealed details about the depths of the sources responsible for the Tona anomaly up to the margin, which yielded better SDR depth results that are consistent with seismic-gravitational studies. The 2-D Euler method was used to calculate source depths of 8000–20000 m for the conspicuous Tona anomaly from a NW-trending profile.

In addition, a 2-D gravimetric inversion model based on a NE-trending profile was used to identify a mafic body along the Patagonia-Gondwana suture bounded by a sub-surface. This body may be an imbrication of the suture located in basement rocks.

Acknowledgements

To the following institutions, the Instituto de Geodesia y Geofísica Aplicadas (IGGA), School of Engineering of the Universidad de Buenos Aires, Instituto Geofísico Sismológico Volponi (IGSV) from the School of Physical and Natural Sciences of the Universidad Nacional de San Juan and the Instituto Universitario Naval (INUN), which have provided financial support for the Project PID Project B-ESCM - Caracterización geofisica y geodésica de la plataforma, borde continental y Cuenca Argentina a través del análisis de datos oceanográficos y métodos potenciales en el Océano Atlántico Sur (60ºW - 40ºW).

References

Amante, C., Eakins, B.W., 2009. ETOPO1 1 Arc-Minute Global Relief Model Procedures, Data Sources and Analysis. *NOAA Technical Memorandum NESDIS NGDC* -24, National Geophysical Data Center*, NOAA*, doi:10.7289/V5C8276M.

Arecco, M.A., Ruiz, F., Pizarro, G., Giménez, M. Martínez, M.P., Ramos, V.A., 2016 *a*. Gravimetric determination of the continental–oceanic boundary of the Argentine continental margin (from 36◦S to 50◦S), *Geophys. J. Int.,* 204, 366–385*.*

Arecco, M.A., Larocca, P.A., Oreiro, F., Pizarro, G., Ruiz, F., 2016 *b*. Estudio del margen continental argentino para la determinación del límite entre corteza oceánica y continental (desde 40ºS hasta 44ºS) a partir de métodos geomagnéticos. *Latinmag Letters*, Volume 6, Special Issue, Proceedings São Paulo, Brasil, A03, 1-7.

Austin, J.A., Uchupi, E., 1982. Continental–Oceanic crustal transition of southwest Africa. *AAPG Bull*. 66 (9): 1328–1347.

Baldi, J.E., Nevistic, V.A., 1996. Cuenca costa afuera del golfo San Jorge. Ramos, V. y Turic, M. (Eds.), XIII Congreso Geológico Argentino y III Congreso de Exploración de Hidrocarburos, Asociación Geológica Argentina e Instituto Argentino del Petróleo y el Gas, Relatorio (10): 171-192, Buenos Aires.

Blakely, R. 1996. Potential theory in gravity and magnetic applications. Cambridge University Press, London, 461pp.

Chernicoff, C.J., Zappettini, E.O., Peroni J., 2014. The Rhyacian El Cortijo suture zone: Aeromagnetic signature and insights for the geodynamic evolution of the southwestern Rio de la Plata craton, Argentina. *Geoscience Frontiers*, (5): 43–52.

Cingolani, C.A., 2011, The Tandilia System of Argentina as a southern extension of the Río de la Plata craton: An overview: *International Journal of Earth Sciences*, v. 100, p. 221–242. doi:10.1007/s00531-010-0611-5

Cingolani, C.A. and Dalla Salda, L., 2000. Buenos Aires cratonic region. In: Cordani, U., Milani, E., Thomaz Filho, A., Campos, D. (Eds.), Tectonic Evolution of South America. Proceedings 31st International Geological Congress, Río de Janeiro, pp. 139–146.

Cingolani, C.A., Santos, J.O.S., Griffin, W., 2010. New insights of the Palaeoproterozoic basement of Tandilia belt, Río de la Plata craton, Argentina: first Hf isotope studies on zircon crystals. In: Symposium GEOSUR, Extended Abstract, Mar del Plata, pp. 21–24.

Cooper, G.R.J. and Cowan, D.R., 2006. Enhancing potential field data using filters based on the local phase. *Comput. Geosci*., (32): 1585–1591.

Dalla Salda, L.H., Bossi, J. y Cingolani, C.A. 1988. The Rio de la Plata cratonic region of southwestern Gondwana. Episodes, 11, (4): 263-269.

Dalla Salda, L., 1987. Basement tectonics of the southern Pampean Ranges. *Tectonics* 6(3): 249-260.

Dalla Salda, L. and Francese, J., 1985. Los granitoides de Tandil. In: 1° Jornadas Geológicas Bonaerenses, Comisión Investigaciones Científicas de la provincia de Buenos Aires: 845-861, La Plata.

Dalla Salda, L.H., Bossi, J. y Cingolani, C.A. 1988. The Rio de la Plata cratonic region of southwestern Gondwana. Episodes, 11 (4): 263-269.

Durrehim, R.J. and Cooper, G.R.J., 1998. EULDEP: a program for the Euler deconvolution of magnetic and gravity data. *Computers & Geosciences* 24, (6): 545-550.

Ewing, M., Ludwig, W.J., Ewing, J.I., 1963. Geophysical investigations in the submerged Argentine coastal plain. Part 1. Buenos Aires to Peninsula Valdez. *Geological Society of America Bulletin*, (74): 275–292.

Fragoso-Cesar, A.R.S., 1980. O Cráton do Rio de la Plata e o Cinturão Dom Feliciano no Escudo Uruguaio-Sul-Riograndense. In: Congresso Brasileiro de Geologia, 31 SBG, vol. 5. Anais, Camboriú, 2879-2892.

Franke, D., Neben, S., Ladage, S., Schreckenberger, B., Hinz, K., 2007. Margin segmentation and volcano-tectonic architecture along the volcanic margin off Argentina/Uruguay, South Atlantic. *Marine Geology*, Vol. 244 (1-4): 46–67.

Fryklund, B., Marshall, A., Stevens, J., 1996. Cuenca del Colorado. In: Ramos, V. y Turic, M. (Eds.), XIII Congreso Geológico Argentino y III Congreso de Exploración de Hidrocarburos, Asociación Geológica Argentina e Instituto Argentino del Petróleo y el Gas, Relatorio (8): 135–158.

Ghidella, M.E., Chernicoff, C.J., Köhn, J., Kostadinoff, J., Gianibelli, J. C., 2005. Anomalías magnéticas en la provincia de Buenos Aires: compilación digital y principales unidades estructurales. In 15º Congreso Geológico Argentino, Cabaleri N., Cingolani, C.A, Linares, E., López de Luchi, M.G., Ostera, H.A. and Panarello, H.O. (eds.). In CD-ROM, Nº 161, 8 pp.

Gunn, P., 1975. Linear transformations of gravity and magnetic fields. *Geophysical Prospecting*, 23 (2): 300–312.

Hinz, K., Neben, S., Schreckenberger, B., Roeser, H.A., Block, M., Goncalves De Souza, K., and Meyer, H., 1999. The Argentine continental margin north of 48ºS: sedimentary successions, volcanic activity during breakup, *Marine and Petroleum Geology*, (16): 1–25.

Introcaso, A. 1980. A gravimetric interpretation of the Salado Basin (Argentina), *Bollettino di Geofisica Teorica ed Applicata*, 22, (87): 187-200.

Introcaso, A. 2003. Significativa descompensación isostática en la Cuenca del Colorado (República Argentina). *Revista de la Asociación Geológica Argentina*, 58 (3): 474-478.

Introcaso, A., Ghidella, M.E., Ruiz, F., Crovetto, C.B., Introcaso, B., Paterlini, C.M., 2008. Métodos gravi-magnetométricos modernos para analizar las características estructurales de la plataforma continental argentina. *Geoacta*, (33): 1-20.

Introcaso, A and Ramos, V.A, 1984. La cuenca del Salado. Un modelo de evolución aulacogénica. In: 9° Congreso Geológico Argentino. Actas (3): 27-46.

Kay, S.M., Ramos, V.A. Mpodozis, C., Sruoga, P., 1989. Late Paleozoic Jurassics silicic magmatism at the Gondwana margin: Analogy to the Middle Proterozoic in North America? *Geology*, (17): 324-328.

Lefort, J.P., Max, M.D., Roussel, J., 1988. The north-west boundary of Gondwanaland and its relationship with two satellite sutures Geophysical evidence. Evolution of the Caledonide-Appalachian Orogen. *Geol. Soc. Lond. Spec. Pub.,* (38): 49-60.

López de Lucchi, M.G., Rapalini, A.E., Tomezzoli, R.N., 2010. Magnetic fabric and microstructures of Late Paleozoic granitoids from the North Patagonian Massif: evidence of a collision between Patagonia and Gondwana? *Tectonophysics.* 494 (1-2): 118-137.

Malumián, N. and Ramos, V., 1984. Magmatic intervals, transgression-regression cycles and oceanic events in the Cretaceous and Terceary of southern South *America, Earth Planet. Sc. Let.* (67): 228-237.

Marinelli, R.V., Franzin, H.J., 1996. Cuencas de Rawson y península Valdés. In: Ramos, V. y Turic, M. (Eds.), XIII Congreso Geológico Argentino y III Congreso de Exploración de Hidrocarburos, Asociación Geológica Argentina e Instituto Argentino del Petróleo y el Gas, Relatorio (9):159-169.

Max, M.D., Ghidella, M.E., Kovacs, L., Paterlini, M., Valladares, J.A., 1999. Geology of the mainland Argentine continental shelf and margin from aeromagnetic survey. *Marine Petroleum Geology*, (16): 41-64.

Meyer, B., Saltus R., Chulliat A., 2016. EMAG2: Earth Magnetic Anomaly Grid (2-arc-minute resolution) Version 3. *National Centers for Environmental Information*, NOAA. Model. doi:10.7289/V5H70CVX.

Miller, H.G. and Singh, V., 1994. Potential field tilt-A new concept for location of potential field sources. *J. Appl. Geophys,* (32): 213–217.

Milligan, P.R. and Gunn, P.J., 1997. Enhancement and presentation of airborne geophysical data 1. *Journal of Australian Geology & Geophysics*, 17, (2): 63-75.

Mushayandebvu, M. F., van Driel, P., Reid, A.B., and Fairhead, J.D., 2001, Magnetic source parameters of two-dimensional structures using extended Euler deconvolution: Geophysics, (66): 814-823.

Nabighian, M.N., 1972. The analytic signal of two-dimensional magnetic bodies with polygonal cross section: its properties and use for automated interpretation. *Geophysics*, (37): 507–517.

Nabighian, M.N., 1984. Toward a three-dimensional automatic interpretation of potential field data via generalized Hilbert transforms: fundamental relations, *Geophysics*, (49): 780–786.

Nabighian, M.N, Grauch, V.J.S., Li, Y., Peirce, J.W., Phillips, J.D., Ruder, M.E., 2005. The historical development of the magnetic method in exploration. *Geohphysics*, (70), 6: P33ND-61ND.

Pankhurst, R.J., Ramos, A., Linares, E., 2003. Antiquity of the Río de la Plata Craton in Tandilia, southern Buenos Aires province, Argentina. *Journal of South American Earth Sciences,* 16 (1): 5-13.

Pángaro, F., Ramos, V.A., Kohler, G., 2011. Las cuencas del Colorado y Salado: nueva interpretación sobre su origen y su impacto en la configuración del Gondwana durante el paleozoico. In: XVIII Congreso Geológico Argentino, Neuquén. Abstracts on CD, 117-118.

Pángaro, F. and Ramos, V.A., 2012. Paleozoic crustal blocks of onshore and offshore central Argentina: New pieces of the southwestern Gondwana collage and their role in the accretion of Patagonia and the evolution of Mesozoic south Atlantic sedimentary basins. *Marine and Petroleum Geology*, (37): 162-183.

Paton, D.A., Mortimer, E.J. Hodgson, N., Van Der Spuy, D., 2016. The missing piece of the South Atlantic jigsaw: when continental break-up ignores crustal heterogeneity, Lyell Collection, The Geological Society of London. Special Publications.

Pizarro, G, Arecco, M.A. Ruiz, F., Ghidella, M. 2016. Modelado 3D por inversión gravimétrica de cuencas off shore de Argentina. *Geoacta*, 40, (2): 11-27.

Rabinowitz, P.D., LaBrecque, J., 1979. The Mesozoic South Atlantic Ocean and evolution of its continental margins. *J. Geophys. Res*., (84): 5973-6002.

Ramos, V.A., 1988. Late Proterozoic-Early Paleozoic of South America - a Collisional History. Episodes, 11, (3): (168-174).

Ramos, V.A., Riccardi, A.C. y Rolleri, E.O., 2004. Límites naturales del norte de la Patagonia. Revista de la Asociación Geológica Argentina, 59 (4): 785-786.

Ramos, V.A., 1996. Evolución tectónica de la Plataforma Continental, Geología y Recursos de la Plataforma Continental, In: Ramos, V. y Turic, M. (Eds.), Relatorio del XIII Congreso Geológico Argentino y III Congreso de Exploración de Hidrocarburos, Asociación Geológica Argentina e Instituto Argentino del Petróleo y el Gas, Relatorio (21): 385-404.

Ramos, V.A., 2008. Patagonia: A paleozoic continent adrift? *Journal of South American Earth Sciences,* (26): 235–251.

Ramos, V.A., Chemale, F., Naipauer, M., Pazos, P.J., 2014. A provenance study of the

Paleozoic Ventania System (Argentina): Transient complex sources from Western and Eastern Gondwana, *Gondwana Research*, (26): 719–740.

Rapallini, A., 2005. The accretionary history of Southern South America from the latest Proterozoic to the Late Palaeozoic: some palaeomagnetic Constraints, Terrane Processes at the Margins of Gondwana, *Geological Society of London, Special Publication*, (246): 305-328.

Rapella, C., Pankhurst, R., 1993. El volcanismo riolítico del noreste de la Patagonia: Un evento meso-jurásico de corta duración y origen profundo. In: XII Congreso Geológico Argentino y II Congreso de Exploración de Hidrocarburos, Actas (4): 179-188, Mendoza.

Reid, A.B., Allsop, J., Granser, H., Millett, A., Somerton, I., 1990. Magnetic interpretation in three dimensions using Euler Deconvolution. *Geophysics* 55, (1): 80-91.

Reid, A.B., Fitz Gerald, D., McInerney, P., 2003. Euler deconvolution of gravity data. In: Society of Exploration Geophysicists (SEG), Annual Meeting, 580-583, New Orleans, 13-18 September.

Riley, T. R., Flowerdew, M. J., Pankhurst, R. J., Curtis, M. L., Millar, I. L., Fanning, C. M. and Whitehouse, M. J. 2016. Early Jurassic magmatism on the Antarctic Peninsula and potential correlation with the Subcordilleran plutonic belt of Patagonia. *Journal of the Geological Society,* (174): 365-376, doi:10.1144/jgs_2016-053.

Rolleri, E.O., 1972. Acerca de la dorsal del Mar Argentino y su posible significado geológico. IN: V Congreso Geol. Arg., Actas (4): 203-220.

Ruiz, F. and Introcaso, A., 2011. Study of the Claromecó basin from gravity, magnetic and geoid ondulation charts. *Boletín del Instituto de Fisiografía y Geología*, 79-81.

Salem, A. and Smith, R., 2005. Depth and structural index from normalized local wavenumber of 2-D magnetic anomalies. *Geophysical Prospecting*, (53): 83–89.

Sylwan, C., 2001. Geology of the Golfo San Jorge Basin, Argentina. *Journal of Iberian Geology*, (27): 123-157.

Talwani, M., J. L. Worzel, and M. Landisman, 1959. Rapid gravity computations for two-dimensional bodies with application to the Mendocino submarine fracture zone. J. Geophys. Res., 64: 49-59.

Tankard, A. J., Uliana, M. A., Welsink, H. J., Ramos, V. A., Turic, M., França, A. B., Milani, E. J., de Brito Neves, B. B., Eyles, N., Skarmeta, J., Santa Ana, Wiens, F., Cirbian, M., Lopez, O. P., De Wit, G. J. B., Machacha, T. and McG. Miller, R., 1995. Structural and Tectonic Controls of Basin Evolution in Southwestern Gondwana during the Phanerozoic. AAPG Special Volumes. In: Tankard A. J., Suárez Soruco, R. & Welsink, H. J., (Eds.), Petroleum basins of South America. Am. Assoc. Pet. Geol. Mem., (62): 5-52.

Tavella, G.F. and Wrigth, C., 1996. Cuenca del Salado, Geología y Recursos de la Plataforma Continental. In: Ramos, V. y Turic, M. (Eds.), Relatorio del XIII Congreso Geológico Argentino y III Congreso de Exploración de Hidrocarburos, Asociación Geológica Argentina e Instituto Argentino del Petróleo y el Gas, Relatorio (6): 95-116.

Teruggi, M.E., Leguizamón, M.A., and Ramos, V.A., 1988, Metamorfitas de bajo grado con afinidades oceánicas en el basamento de Tandil: Su implicancia geotectónica, Provincia de Buenos Aires, *Revista Asociación Geológica Argentina*, 43, (3): 366–374.

Thompson, D.T., 1982. EDULDPH: A new technique for making computer-assisted depth estimates from magnetic data. *Geophysics*, 47, (1): 31–37.

Urien, C.M. and Zambrano, J.J., 1974. The Geology of the Basins of the Argentine Continental Margin and Malvinas Plateau, The South Atlantic, ed. Springer, 135-169.

Varela, R., Cingolani, C., Dalla Salda, L., 1988. Geocronología Rb/Sr en granitoides del basamento de Tandil, provincia de Buenos Aires. In: 2ª Jornadas Geológicas bonaerenses. Resúmenes: 291-304, Bahía Blanca.

Verduzco, B., Fairhead, J.D., Green, C.M., MacKenzie, C., 2004. New insights to magnetic derivatives for structural mapping. *Leading Edge*, (23): 116–119.

Zambrano J.J., 1974, Cuencas sedimentarias en el subsuelo de la provincia de Buenos Aires y zonas adyacentes. *Revista de la Asociación Geológica Argentina*, 29, (4): 443-469.

Geofísica Internacional (2018) 57-3: 177-187

Original paper

Soil gas radon measurements for investigating the actual status of seismic quiescence along the bounding fault of the Ghab pull-apart basin in western Syria

Mohamed Al-Hilal* and Mohamad K. Abdul-Wahed

Received: October 17, 2017; accepted: May 22, 2018; published on line: July 02, 2018

Resumen

El propósito de este trabajo consistió en investigar posibles cambios de radón relacionados con la zona de falla que pudieran mostrar alguna relación con la tectónica local a lo largo de la zona de falla de la cuenca de Ghab. A pesar de su actividad histórica, la falla de Ghab presenta actualmente una falta de actividad sísmica con un periodo largo de quietud sísmica. Se escogieron 7 sitios para realizar muestreos de radón utilizando un equipo ALPHAGUARD. El valor promedio normal de radón de fondo se obtuvo con medidas realizadas lejos de la zona de influencia de la falla. Se definió un rango estadístico de variaciones anómalas de radón con límites marcados por el valor promedio mas/menos dos desviaciones estándar (X+/- 2DS). Los resultados iniciales muestran incrementos de radón en las estaciones de monitoreo a lo largo de la zona de falla con picos 4-5 veces mayores que el nivel de fondo. Aunque estas concentraciones anómalas relativamente grandes podrían confirmar la utilidad del radón como un posible indicador para trazar los límites de la falla, no prueban necesariamente una relación con la actividad tectónica del área. Sin embargo, estos incrementos de radón podrían indicar una evidencia de zonas con mayor permeabilidad asociadas a la deformación de la estructura en la zona de ruptura.

Palabras clave: Radón en suelo, zona de falla, Cuenca de desplazamiento de Ghab, quietud sismica, Siria.

Abstract

The aim of the present work was to investigate possible spatial fault-related radon changes, which could reveal some important features related to the active nature of local tectonics along the bounding fault of the Ghab basin. Despite its active historical record, the Ghab fault is presently characterized by apparent lack of earthquake activity with a temporal period of seismic quiescence. Seven sites were selected to perform soil radon sampling along the fault using an AlphaGUARD radon monitor. The average background of normal radon emission from local soil and rocks was established apart from the tectonic influence of the fault zone. A statistical range of anomalous radon variation was defined by the limits of the mean value plus/minus two standard deviations (X±2SD). The initial results revealed high radon increases in the sampled stations along the fault zone, with peak values about 4-5 times above the background level. Although such relatively anomalous concentrations may confirm the usefulness of soil gas radon as a possible indicator for tracing the basin-bounding fault, they do not necessarily prove a definite relation with actual active tectonics in the area. However, these increases may possibly indicate evidences of enhanced radon response to a higher permeability medium associated with the deformed structure of the rupture zone.

Key words: Soil gas radon, Fault zone, Ghab pull-apart basin, Seismic quiescence, Syria.

Mohamed Al Hilal*
Mohamad K. Abdul-Wahed
Department of Geology
Atomic Energy Commission of Syria
P.O box 6091, Damascus, Syria
*Corresponding author: cscientific3@aec.org.sy

Introduction

The Dead Sea fault system (DSFS) represents a prominent strike-slip transform structure in the eastern Mediterranean region. The system has been regarded as an active plate boundary formed by the separation of the Arabian plate (east) from the African plate (west) in mid-Cenozoic (Barazangi *et al*., 1993). As a remarkably important structural feature, the DSFS has become the focus of attention for many researchers who studied its seismotectonic evolution and paleoseismic history using different approaches (Darkal *et al*., 1990; Devyatkin *et al*., 1997; Ambraseys and Jackson, 1998; Brew *et al*., 2001; Gomez *et al*., 2003). However, Megrhaoui *et al*. (2003) found that the seismic behavior of the northern DSFS seems to pass currently through a quiescent period with a seismic gap of ~830 yr without any occurrence of major earthquakes. Moreover, Abdul-Wahed and Al-Tahan (2010) pointed out that the seismicity of Syria is actually characterized by a very limited number of focal mechanisms with apparent low level seismicity. Accordingly, they concluded that the earthquake activity in the country is presently distinguished by producing a little number of low magnitude seismic events. Although the prevailing period of seismic quiescence implies that the system has been seismically inactive in the last few centuries, and this might be a sign of high level of seismic hazard in the region due to a probable potential strain accumulation (Ambraseys and Barazangi, 1989).

Considering the peculiarity of the Ghab depression as a distinctive pull-apart basin of the northern DSFS, it seems very important to explore the observed status of seismic quiescence prevailing over such tectonically vital area. One encouraging technique for achieving this goal is probably the use of soil gas radon measurement, which has been recognized as a significant natural tracer for characterizing the structure of subsurface faults in several tectonic regions throughout the world (King *et al*., 1996; Baubron *et al*., 2002; Steinitz *et al*., 2015). Thus, considerable information concerning the trend and location of the fault, besides understanding the nature of its tectonic activity, could be obtained through analyzing the distribution pattern of radon emission in the survey area (Etiope *et al*., 2002; Al-Hilal and Abdul-Wahed, 2016). Accordingly, the main objective of this study is to check whether the bounding fault of the Ghab pull-apart basin shows any spatial tectonically-induced radon anomalies that might be useful for mapping out the trend of the fault, and providing further information concerning the current active status of its local tectonics.

The study area

Geologic and tectonic settings

The DSFS location, local seismicity and the study area are shown in Figures 1 and 2. The Ghab depression (~55 × 15 km), located along the eastern flank of the Syrian Coastal Mountains Range, is a flat marshy trough that is filled by thick horizontal Pliocene lacustrine sediments (Ponikarov, 1966; Devyatkin *et al*., 1997). The prevailing Pliocene sediments consist basically of marls, calcareous marls and clays alternating with sandstones and well cemented conglomerate beds at depth. The Pliocene is covered by a thin sheet of Quaternary (Pleistocene and Holocene) formations, which are represented mainly by unconsolidated deposits including reddish and dark clays, sandy loams, pebbles, flood plain and alluvial fans of fleeting valley deposits. The Paleogene rocks (Middle Eocene) are outcropped in the northeast border of the Ghab basin, where they are composed essentially of soft chalky and nummulitic limestone, clayey limestone and marls. Cretaceous rocks (Cr 2), which outcrop directly in the eastern edge of the study depression, are commonly formed by limestone and dolomite rocks that are struck by a number of distinct faults and fractures (Figure 3).

Tectonically, the Ghab depression represents a deep pull-apart basin that developed through the structural evolution of the northern DSFS since Pliocene (Ponikarov, 1966). To the south of the study area, the main fault merges with Missyaf narrow segment (~60 km long) which extends between the Boqeia pull-apart basin (south) and the Ghab depression (north) (Figure 4). Missyaf fault splays northward into two distinctive segments bounding the Ghab trough from western and eastern flanks, and thus forming the general framework of its actual structure. Brew *et al*. (2001) defined the Ghab pull-apart basin as a Pliocene-Recent tectonic feature that was formed as a deep structure opened in response to a complex mechanism of a left-step movement in the northern DSFS. Unlike the eastern side, the western border of the Ghab basin is hardly defined because it is hidden by the accumulation of various mass-wasting materials, and is mostly concealed below some large blocks detached from the flank of the adjoining coastal range. However, the general margins of the Ghab depression are sufficiently outlined by a series of faults with distinct blocks and scarps along which the central part of the main basin is subsided (Figure 3).

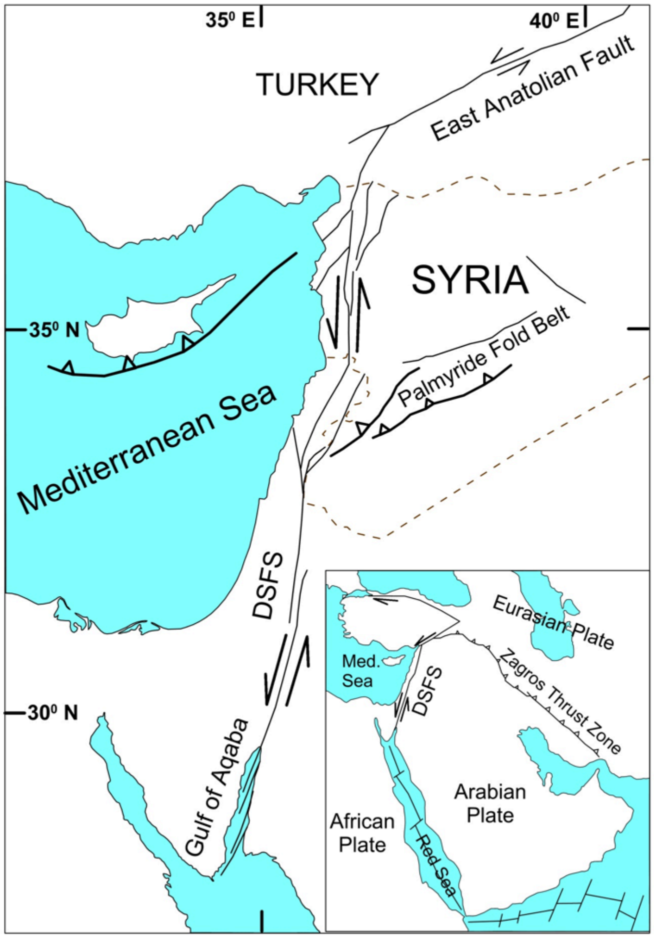

Figure 1. Regional tectonic map showing the location of Syria relative to the Arabian, African and Eurasian plates.

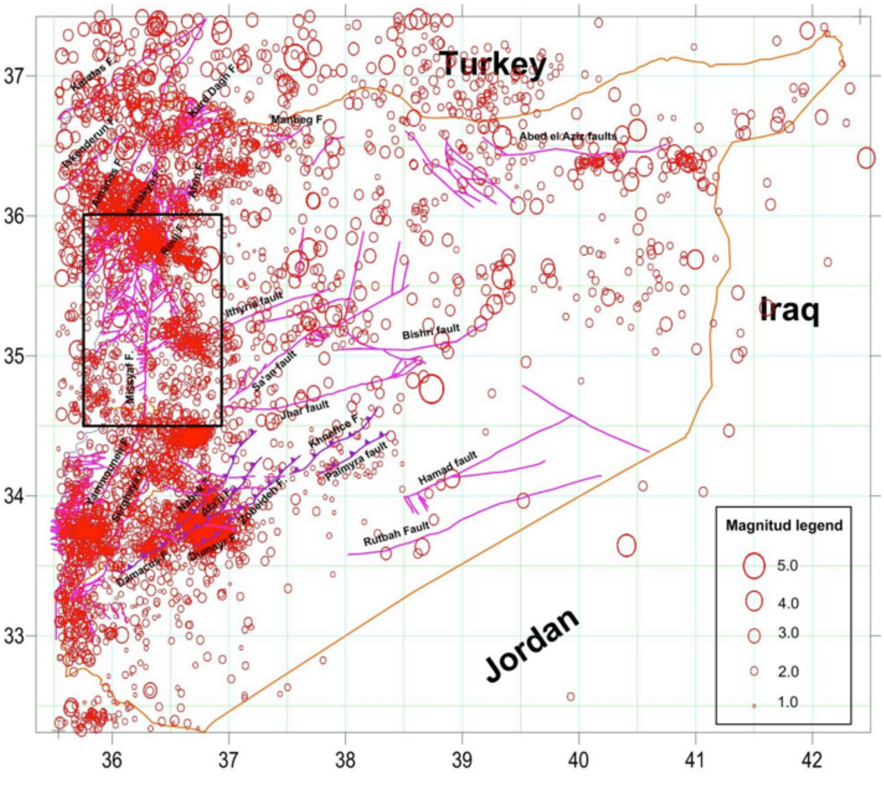

Figure 2. Instrumental seismic activity in Syria during the period (1995-2012). The *rectangle* indicates the location of the present study area.

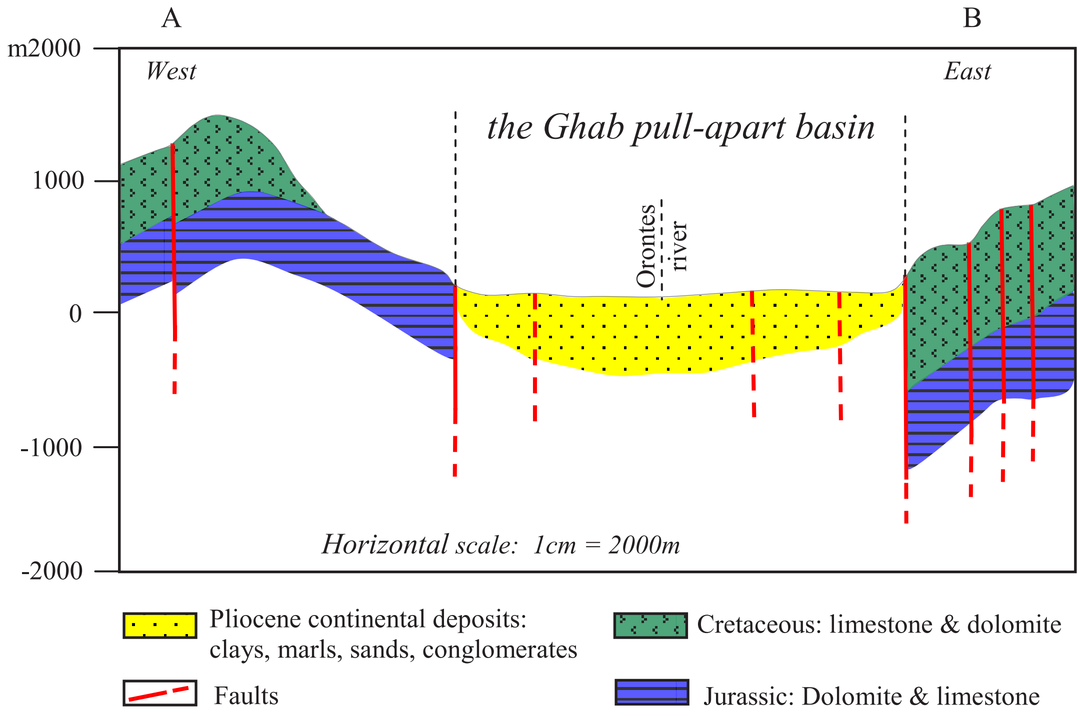

Figure 3. Geological cross-section across the Ghab pull-apart basin.

Seismic activity

The lack of seismicity which characterized the main fault segments of the northern DSFS such as the Missyaf and Ghab faults throughout the last century is still observed during the recent time (Figure 2). Although the study region had been historically considered as a seismogenic source of numerous moderate-to-large earthquakes in the past, it currently shows an apparent status of seismic quiescence (Meghraoui, 2015). On other words, the lack of major seismic events with Mw > 6.0 on most segments of the main fault system in the last century appears to be incompatible with its historical catalogue (Ambraseys and Jackson, 1998). Analysis of data from the Syrian National Seismological Network (SNSN) revealed that the seismic activity along most segments of the northern DSFS in Syria produce a little number of low magnitude seismic events (Abdul-Wahed and Al-Tahan, 2010). Additionally, the distribution of epicenters of earthquakes in the region has shown that the instrumental seismicity along both the Ghab and Missyaf segments is very low (Figure 2). Moreover, historical and recent seismic data of Syria provide evidence indicating that the seismicity in the concerned region tends to fade out with time through the last millennium.

Materials and methods

Radon monitoring stations

The locations of radon monitoring sites were chosen in accordance with the convenience and accessibility to the surveyed area, besides extensive geological and tectonic field investigations. Accordingly, seven soil gas radon monitoring stations were determined within four main locations, namely Asharneh, Afamia, Al-Taka and Qatroon all of which are located along the bounding fault of the Ghab basin (Figure 4). The first three stations were established at Asharneh area and the next two stations were set up at Afamia, besides one station for each of Al-Taka and Qatroon sites. The radon stations of Asharneh and Qatroon are located on the southern and northern ends of the Ghab trough respectively, while the other two stations (Afamia and Al-Taka) are situated along the eastern fault boundary of the Ghab depression. However, the western margin of the Ghab basin seems to be not appropriate for carrying out radon measurements because no surface expression could be identified along the western fault boundary, except in the far north where the Qatroon village is located. This obstacle along the western boundary of the study basin is mostly related to the rough topographic relief due to the burial by mass-wasting and accumulations of very large rocky blocks from the adjoining mountain ranges. An additional station for determining the normal level of radon background in the region was chosen near Sqelbieh town, which is located over a stable plateau at ~20 km to the east of the Ghab basin, away from any tectonic influence of the fault zone (Figure 4). Finally, all monitoring stations including the background area are characterized by similar lithological facies of Pliocene continental deposits that are covered by a thin unconsolidated weathered horizon of recent formations.

Radon measurements

Radon (^{222}Rn) is a naturally occurring radioactive gas that is constantly generated through the decay series of uranium (^{238}U), with a half-life of 3.82 days. It is a noble, colorless, odorless and tasteless gaseous element present almost everywhere on the Earth's crust. The unique properties of radon make it an important tracer which can be used for investigating some geotectonic processes that may induce gas movement in the ground. Thus, considerable information concerning the trend and location of the fault, besides understanding the nature of its tectonic activity, could be obtained through analyzing the distribution pattern of radon emission in the survey area (King *et al*., 1996; Al-Hilal and Al- Ali, 2010; Richon *et al*., 2010)

In this work, the measurements of radon concentration in soil gas were achieved through an method, using a portable AlphaGUARD PQ2000 Pro radon monitor. In practice, at

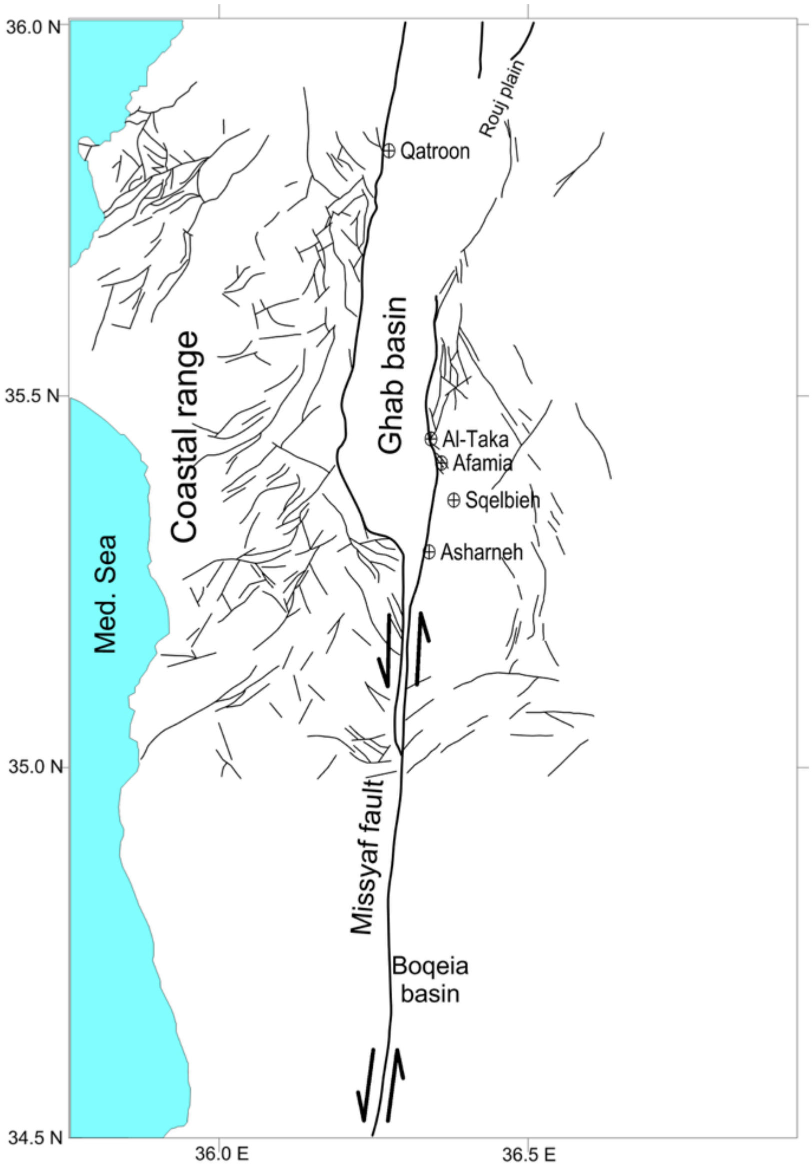

Figure 4. Locations of radon monitoring stations along the bounding fault of the Ghab pull-apart basin.

each measuring point a hole of 75cm deep and 2cm diameter was drilled in the ground and the soil probe inserted into the hole. With the system tightened from all sides, the soil gas radon is automatically drawn out into the ionization chamber of the instrument with a steady continuous pumping rate of 0.3L/min. As radon level in soil usually shows an initial growth before it is stabilized, the radon activities were registered in 10-min intervals over about one hour period, at each sampling point. Consequently, an average value of radon in soil concentration (Bq m^{-3}) can be measured with fairly good confidence.

Statistical analysis of radon data

Soil gas radon data were statistically analyzed in order to define their common distribution in the monitoring stations and to enable the separation between normal radon concentrations from other anomalous or geotectonic related values (Table 1). The analysis includes the calculation of minimum, maximum, mean value (X), standard deviation (SD) and the coefficient of variability (CV%), which reflects the extent of radon homogeneity in the soil. The CV is considered to be reversely proportional with the degree of radon dispersion pattern, and it is generally calculated through the following formula:

$$CV\% = (SD/X) \text{ x } 100$$

Table 1 summarizes the basic statistical characteristics of the resultant radon concentrations in soil which have been measured at seven monitoring stations that are distributed along the bounding fault of the Ghab basin. In order to avoid possible effects of meteorological variables on soil radon concentration, the survey was fulfilled under comparable weather conditions during the years 2010 and 2011. Besides, the normal background level (BG) of soil radon activity in the study area was established in a separate stationary site that is located apart from the tectonic influence of the fault (Figure 4). On this basis, the average BG of radon production was estimated as ~5000 Bq m^{-3}, whereas, radon measurement along the rupture zone of the fault showed relatively higher concentrations, with peak values of about 4 to 5 times higher than the average BG level. In view of that, two separate groups of soil radon concentration values were identified (Figure 5). The first represents the background population indicated by a red solid curve and characterized by low average value of ~5000 Bq m^{-3}. While the second group points to the anomalous population marked by relatively higher values (4–5 times higher than the BG level), and it is defined by a range of the mean value plus-minus two standard deviation (X±2SD). Radon data of this range is regarded important because they are spatially consistent with the trace of the fault rupture, and thus they could be considered as anomalous or geotectonic related values. Meanwhile, it is worth mentioning that the geology of the study region, including the Ghab area and its surroundings, is commonly marked by a general decrease of radioactivity level because of the lack of any natural radioactive source such as igneous acidic rocks. Hence, the estimated BG level of radon activity in the concerned region was found to be fairly low (~5000 Bq m^{-3}). Such relatively low radon concentration might be referred to the low corresponding values of radium (^{226}Ra) content found in nine soil samples taken from the same sites where the radon measurements were carried out. The collected samples were dried, sieved and chemically analyzed for determining ^{226}Ra content in soil using gamma-ray spectrometry technique. Although some samples revealed low radium values ranging from 12.00±1.50 to 14.28±2.95 Bq kg $^{-1}$, most of the analysis results were below the detection level (BDL), where DL =12 Bq kg^{-1}.

Table 1. Statistical characteristics of soil gas radon concentrations measured along the bounding fault of the Ghab pull-apart basin in western Syria.

Monitoring Sites	**Soil / rock Types**	**No. of sampling**	**Radon Data (Bq/m3)**				
			Min.	**Max.**	**Mean**	**SD**	**CV%**
Asharneh	Recent sandy loams, clays, pebbles	33	16750	29000	23200	3484	15
Afamia	Clays, loams, sands, limestone	22	16802	26270	22128	2908	13
Al-Taka	Clays, loams, sands, limestone	11	17234	25788	21542	2774	13
Qatroon	Clays, marls, sandstone, limestone	11	16558	23860	21504	2528	13
Background Area	Pliocene continental deposits: clays, marls, conglomerate	11	4721	5355	5000	-	-

Results and discussion

The results of soil gas radon measurements revealed comparable concentration values. The average radon concentration was found to be 23200 Bq m^{-3}, with a standard deviation of 3484 for Asharneh station; 22128 Bq m^{-3}, with a standard deviation of 2908 for Afamia station; 21542 Bq m^{-3}, with a standard deviation of 2774 for Al-Taka station and 21504 Bq m^{-3}, with a standard deviation of 2528 for Qatroon station (Table 1). For this set of radon data, the range of anomalous radon variations was estimated to be within the limits of the mean value plus and minus two standard deviations (X±2SD). According to Figure 5, it can be noticed that radon concentrations in all monitoring stations seem to be compatible, and they show almost similar variations with remarkable increases of radon values in comparison with the background level. Furthermore, considering the BG radon level in the survey area (~5000 Bq m^{-3}), a wide range of differences can be observed between the values of anomalous radon measured along the basin-bounding fault, and the BG. In other words, the value of "signal-to-background ratio" was found to vary between 4 and 5. All fault-related radon concentration values appeared to be lye within X±2SD. The "signal-to-background ratio" may reveal a possible spatial relationship with the trend of the underlying deep-seated faulted structure. The appearance of such distinct anomalous radon signals could be attributed to the presence of deformed geologic medium associated with a high permeable zone along the detected rupture zone. Also, they may indicate the occurrence of upward flow of deep soil gases which probably provide a driving mechanism that enhance the emanation of radon through openings and fractures up to the earth surface. However, it is worth to mention that applying radon technique in a seismogenic region does not essentially imply that it is possible to refer any radon peak or anomaly to a specific seismic event or active fault. Hence, there is always a probability of error or false prediction connected with this type of analysis. In principle, radon is transported through the ground either by underground water or by carrier soil gases, such as CO_2, CH_4 and He. Yet, the mechanism of radon migration in both cases greatly relies on the degree of soil permeability and the extent of deformation and fracturing in rocks, regardless of their geotectonic activity (Etiope *et al*., 2002; Lopez *et al*., 2016). In fact, there are many cases in which the level of soil gas radon concentrations, measured over tectonically deformed structures or fault zones, displayed abnormal variations whether the fault was active or inactive. Al-Hilal and Abdul-Wahed (2016) found that permeability properties rather than local tectonic activity seemed to be the main causes controlling the emissions of high radon production along the Damascus fault. Moreover, Lopez *et al*. (2016) mentioned that the emanation of soil radon, measured in west Texas, is mainly related to the transport properties of the geologic medium and not to deeper seismic activity. Additionally, while conducting radon measurements in groundwater along the Serghaya fault in SW Syria, Al-Hilal (2016) found that anomalous radon signature is not necessarily a reflection of active tectonics along the fault, but is most likely an evidence of radon response to the groundwater table fluctuations due to high precipitations. Furthermore, Mojzes *et al*. (2017) deduced that soil radon activity, measured across the assumed fault line in central Slovakia, did not reflect any sign of active local tectonics, but simply indicates the presence of contact zone between different types of rocks. Nevertheless, the correlation between the rate of soil gas radon emission and the position and trend of buried faults or hidden tectonic lineaments has been repeatedly raised through numerous studies in the last decades (King *et al*., 1996; Baubron *et al*., 2002; Steinitz *et al*., 2015). However, the concept of employing radon to serve as a potential sensitive tracer for evaluating the geodynamic activity of faults is a complex issue requiring primarily full understanding of the seismotectonic setting in the surveyed region. Besides, it is important to define the type of movement along the fault and its extension within the Earth's crust, and determine whether it is related to deep-rooted structure or just a superficial fracture. Furthermore, radon may exhibit different concentration values with respect to various types of rocks. Thus, particular attention should be given to the local geology and the prevailing rock/soil types in the survey area, especially when interpreting the data of spatial fault-associated radon anomalies.

With reference to the Ghab basin, where the present study has taken place, it is important to remember some distinctive features and geotectonic characteristics of the basin structure. First, the outer boundary of the Ghab pull-apart basin displays a strike-slip fault movement, which developed as part of a major sinistral transform along the northern DSFS in Syria. Second, the fault represents a remarkable deep-rooted structure that opened in response to a left step motion in the DSFS during the Pliocene and Holocene. Third, it has been demonstrated that the Ghab fault accommodates a significant part of active deformation along the Arabian-African plate boundary (Barazangi *et al*., 1993; Brew *et al*., 2001; Gomez *et al*., 2003). On the other hand, despite all the aforesaid tectonic field evidences, the record of instrumental seismicity of the concerned region including the Ghab and Missyaf fault segments appears quite poor with evident lack of important earthquake activity in the past century. Besides, GPS survey which was recently completed in western Syria has shown unexpected results revealing average geodetic velocity less than 0.6 mm/year, which seems quite a low value compared with the southern part of the DSFS (Alchalbi *et al*., 2010). These observations may be referred to the thought that the northern DSFS is actually passing through a temporal period of seismic quiescence. Thus, the low observed average of slip rate velocity and the scarceness of major earthquake occurrences along most segments of the northern DSFS in the last centuries appear to be in contradiction with the historical catalogue of the system (Ambraseys and Jackson, 1998).

Figure 5 shows notable radon increases with evident anomalous signatures trending in accordance with the trace of the fault zone. Such high radon signals are likely due to the presence of upward flow of soil gases through a permeable geological structure associated with the fault zone. This finding is consistent with the main purpose of this work, which aimed basically at attesting the sensitivity of soil gas radon as a potential tool to characterize fault structure. Although the ultimate results confirmed the existence of spatial relationship between the general trend of radon emissions and the probable trace of the rupture zone, the magnitude of soil radon values do not seem sufficient to determine the active nature of local tectonics along the concerned fault. In other words, considering the concentration values of the measured soil gas radon in this

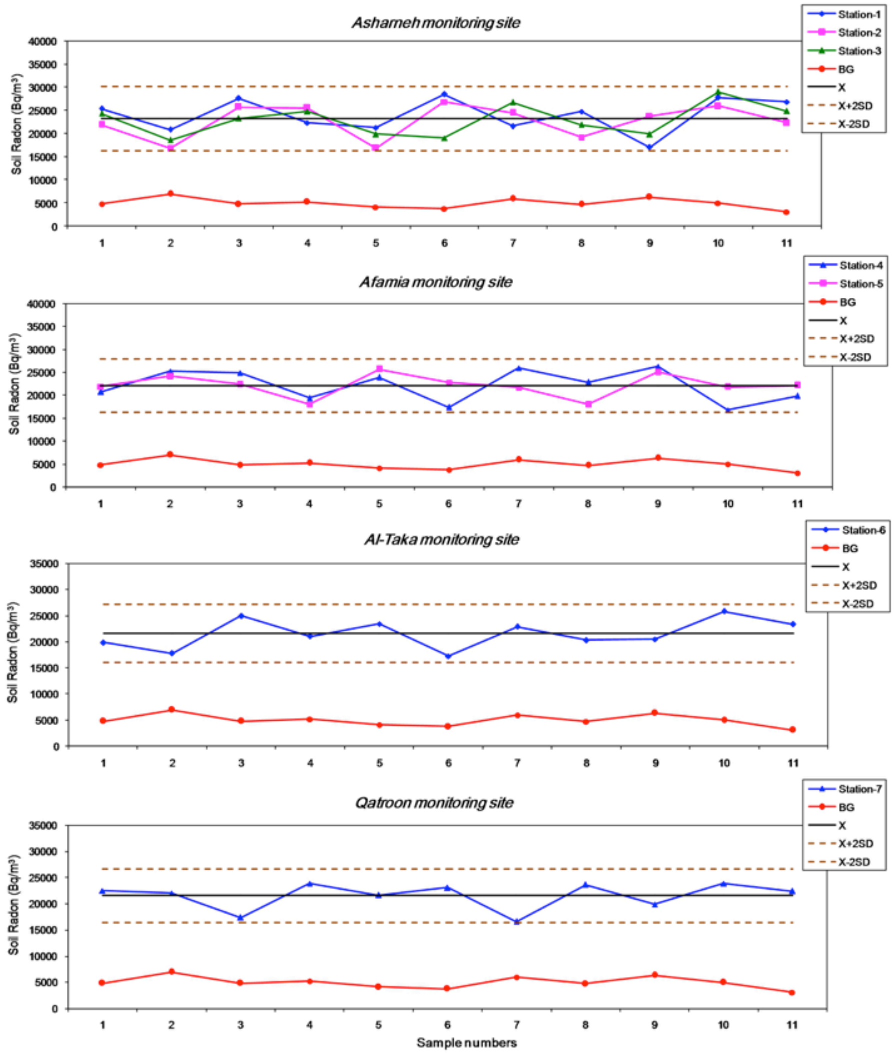

Figure 5. Soil gas radon variations measured at seven stations distributed along the bounding fault of the Ghab basin. (BG): background level; (X): mean value; (X±2SD): mean value plus-minus two standard deviations.

survey, it can be inferred that the general level of radon activity is relatively moderate with peak values of about 4-5 times higher than the estimated BG level. These moderate radon values appear to be in a general agreement with the recently obtained data of the near-field GPS measurements that show low level of slip-rate velocities along the plate boundary of the northern DSFS. Moreover, the modest levels of our soil gas radon concentration appear to be in harmony with the present day status of seismic quiescence, and they might be explained by the assumption of probable continued accumulation of interseismic strain along the fault system.

Concerning the CV value which indicates the degree of radon homogeneity as a variable element in soil, a higher CV implies a lower degree of homogeneity and vice versa. As shown in Table 1, it can be noticed that the level of CV for the measured soil gas radon data appears quite low, with values ranging between 13-15%, and this reflects high homogeneity degree of soil gas radon. Such distinctive homogeneous level is most likely related to the compatible distribution and similar variations of soil gas radon concentration in all sampled stations along the fault zone. This result may possibly indicate that the selected sites of soil gas radon measurements are particularly located right on the trace of the assumed fault axis, which almost extends along the outer margin of the Ghab pull-apart basin. Lastly, from the perspective of the regional earthquake hazard assessment, the actual period of seismic quiescence and the apparent lack of instrumental seismicity may not reflect the realistic hazardous nature of the studied fault zone. On the contrary, they might be a precursory sign of probable high level of potential seismic hazard, particularly in terms of earthquake cycle and continual strain accumulation along the fault system.

Conclusion

Soil radon survey was carried out, during 2010 and 2011, in seven selected sites that are distributed along the bounding fault of the Ghab pull-apart basin in western Syria. The study region is presently marked by a temporal period of seismic quiescence with apparent lack of instrumental seismicity. The results of soil radon data presented herein revealed two separate levels, one represents the background level and the other indicates a distinctive group of anomalous values defined by the limits of the mean value plus-minus two standard deviations. The values of high radon anomalies showed evidences of spatial increases trending in accordance with the assumed trace of the concerned fault. This finding may suggest the usefulness of using soil gas radon technique as a sensitive indicator for mapping out underlying tectonic structures. Although these observations may point out that abnormal radon emissions could provide evidence of a spatial relationship with the trend and location of the rupture zone, they do not seem sufficient enough to demonstrate a reliable assessment regarding the active tectonic nature of the fault. In other words, the moderate level of radon concentration measured in this work seems to be consistent with the current status of seismic quiescence in the region and appears in a general agreement with the low level of slip-rate velocity obtained by the GPS investigations in NW Syria. Hence, such prevailing seismic conditions may possibly influence the rate of soil gas radon release and thereby reduce its level along the bounding fault of the Ghab basin. Finally, considering the viewpoint of regional seismic hazard, it is believed that the prevailing seismic quiescence which exceptionally characterized the system during the last century may indicate that the northern DSFS is presently locked and is accumulating interseismic strain. If so, this could be a warning sign for probable occurrence of large-magnitude earthquakes in the future.

Acknowledgement

The authors wish to express their thanks and gratitude to Professor I. Othman, Director General of the AECS, for his constant encouragement. We would like also to thank Dr. Z. Kattan, Head of the Geology Department of AECS, for his support. We thankfully acknowledge the anonymous reviewers for their valuable suggestions that considerably improved the quality of the paper.

References

Abdul-Wahed M. K., & Al-Tahan I., 2010, Preliminary outlining of the seismological active zones in Syria, Annals of geophysics, 53, 4, PP. 1-9.

Alchalbi, A., Daoud, M., Gomez, F., McClusky, S., Reilinger, R., Romeyeh, M.A., Alsouod, A., Yassminh, R., Ballani, B., Darawcheh, R., 2010, Crustal deformation in northwestern Arabia from GPS measurements in Syria: slow slip rate along the northern Dead Sea fault. Geophys J Int. 180:125–135. doi:10.1111/j.1365- 246X.2009.04431.x

Al-Hilal M., 2016, Establishing the range of background for radon variations in groundwater along the Serghaya fault in southwestern

Syria. Geof?sica Internacional 55-4:215–225. DOI: 10.19155/geofint.2016.055.4.3

Al-Hilal M., Abdul-Wahed MK., 2016, Tectonic and geologic influences on soil gas radon emission along the western extension of Damascus fault, Syria. Environmental Earth Sciences 75(23):1-11. DOI: 10.1007/s12665-016-6292-z

Al-Hilal M., Al-Ali A., 2010, The role of soil gas radon survey in exploring unknown subsurface faults at Afamia B Dam, Syria. Radiat Meas 45:219–224.

Ambraseys N.N., and Jackson J.A., 1998, Faulting associated with historical and recent earthquakes in the Eastern Mediterranean region. Geophys. J. Int. 133(2):390–406

Ambraseys, N.N. and Barazangi, M. 1989, The 1759 earthquake in the Bekaa valley: implications for earthquake hazard assessment in the eastern Mediterranean region. Journal of Geophysical Research, 94, 4007–4013.

Barazangi, M., Seber, D., Chaimov, T., Best, J., Li tak, R., Saad, D. and Sawaf, T., 1993, Tectonic evolution of the northern Arabian plate in western Syria. Recent Evolution and Seismicity of the Mediterranean Region, E. Boschi *et al*.(eds.), PP.117-140.

Baubron, J.C., Rigo, A., Toutain, J.P., 2002, Soil gas profiles as a tool to characterize active tectonic areas: the Jaut Pass example (Pyrenees, France). Earth Planet Sci. Lett. 196, 69-81.

Brew G, Lupa J, Barazangi M, Sawaf T, Al Imam A, Zaza T., 2001, Tectonic and geological evolution of Syria. J Geol Soc Lond 158:665–674 Bulletin of the Syrian National Seismological Network (SNSN), (1995-2012), National Earthquake Center, Ministry of Petroleum and mineral resources, Syrian Arab Republic.

Darkal, , A.N., Krauss, M., and Ruske, R., 1990, The Levant fault zone: An outline of its structure, evolution and regional relationships, Z. Geol. Wiss. Berlin 186, 549–562.

Devyatkin, E. V., Dodonov, A. E., Sharkov, E. V., Zykin, V. S., Simakova, A. N., Khatib, K. and H. Nseir, H., 1997, The El-Ghab Rift Depression in Syria: Its Structure, Stratigraphy, and History of Development. Stratigraphy and Geological Correlation, Vol. 5, No. 4, 1997, pp. 362–374.

Etiope G. and Martinelli G., 2002, Migration of carrier and trace gases in the geosphere: an overview. Physics of the Earth and Planetary Interiors, 129, 185-204.

Gomez F, Meghraoui M, Darkal AN, Hijazi F, Mouty M, Suleiman Y, Sbeinati R, Darawcheh R, Al- Ghazzi R, Barazangi M., 2003, Holocene faulting and earthquake recurrence along the Serghaya branch of the Dead Sea fault system in Syria and Lebanon. Geophys J Int 153:658–674

King, C.Y., King, Bi-Shia, Evans, W.C., 1996, Spatial radon anomalies on active faults in California. Applied Geochemistry 11: 497–510.

López J. A., Dena Ornelas O., Sajo-Bohus L., Rodríguez G., Chavarría I., 2016, Correlation Between Underground Radon Gas and Dormant Geological Faults. Journal of Nuclear Physics, Material Sciences, Radiation and Applications Vol-4, No-1, August 2016 pp. 265–275. DOI: 10.15415/jnp.2016.41025

Meghraoui M., 2015, Paleoseismic History of the Dead Sea Fault Zone. Encyclopedia of Earthquake Engineering, DOI 10.1007/978-3-642-36197-5_40-1

Meghraoui M., Francisco Gomez, Reda Sbeinati, Jerome Van der Woerd, Michel Mouty, Abdul Nasser Darkal, Youssef Radwan, Ihsan Layyous, Haithem Al Najjar, Ryad Darawcheh, Fouad Hijazi, Riad Al-Ghazzi, Muawia Barazangi, 2003, Evidence for 830 years of seismic quiescence from palaeoseismology, archaeoseismology and historical seismicity along the Dead Sea fault in Syria. Earth and Planetary Science Letters 210, 35-52 18

Mojzes Andrej, Frantisek Marko, Barbara Porubcanova, Andrea Bartosova, 2017, Radon measurements in an area of tectonic zone: A case study in Central Slovakia. Journal of Environmental Radioactivity 166 (2017) 278-288

Ponikarov, V. P., 1966, The geology of Syria. Explanatory Notes on the Geological Map of Syria, scale 1:200 000. Sheets I-37-XIX and I-36-XXIV, Ministry of Industry, Damascus, Syrian Arab Republic.

Richon, P., Klinger, Y., Tapponnier, P., Li, Ch.-X., Van Der Woerd, J., Perrier, F., 2010, Measuring radon flux across active faults: Relevance of excavating and possibility of satellite discharges. Radiat. Meas. 45, 211-218.

Steinitz, G., Piatibratova, O., and Malik, U., 2015, Observations on the spatio-temporal patterns of radon along the western fault of the Dead Sea Transform, NW Dead Sea. Eur. Phys. J. Special Topics 224, 629–639, DOI: 10.1140/epjst/e2015-02396-8

Geofísica Internacional (2018) 57-3: 189-203

Original paper

Geoelectrical Combined Sounding-Profiling Configuration for Characterizing the Sedimentary Phosphatic Environment in Al-Sharquieh Deposits Mine in Syria

Jamal Asfahani

Received: December 06, 2017; accepted: May 11, 2018; published on line: July 02, 2018

Resumen

En este trabajo se propone y adapta la configuración geoeléctrica combinada sondeo-perfil para caracterizar el entorno fosfato-sedimentario en la mina Al-Sharquieh, Siria. El electrodo C en el arreglo propuesto de tres electrodos no está fijo en el infinito, sino que se modificó brevemente y es móvil, donde OA=OB=OC=AB/2. La transformación del gradiente también se modificó para tomar en cuenta la pequeña modificación geométrica del arreglo de los tres electrodos. El trabajo muestra varias formas útiles para representar los datos de resistividad obtenidos con esta adaptación. Las medidas convencionales de resistividad ρ_{AB} aparentemente tradicionales, tienen baja resolución, contrariamente a la transformación del gradiente que muestra, en todos los ejemplos analizados, alta resolución en todas direcciones. La transformación del gradiente es muy sensible a los márgenes verticales de las variaciones litológicas, de las zonas fracturadas y de falla, y por lo tanto puede utilizarse como una herramienta cualitativamente útil para interpretar los datos tradicionales de Sondeo Vertical Eléctrico (VES). Se puede obtener un máximo de información geoeléctrica cuando ρ_{AB}, la transformación del gradiente y $\rho_{AC/}$ ρ_{BC} se interpretan conjuntamente, tal como se presenta en este trabajo. Las variaciones litológicas del entorno de fosfato sedimentario en la mina de Al-Sharquieh se caracterizan utilizando el método propuesto de tres electrodos. Su eficacia puede probarse en varias aplicaciones en exploración minera y estructural..

Palabras clave: Configuración combinada perfil-sondeo; VES; Fosfato; Mina Al-Sharquieh; Siria.

Abstract

Geoelectrical combined sounding-profiling configuration is adapted and proposed in this research for characterizing the sedimentary phosphatic environment in Al-Sharquieh deposit mine in Syria. The electrode C in the proposed three-electrode array is not fixed at the infinity, but is slightly modified and movable, where OA=OB=OC=AB/2. The gradient transformation is also modified to take into account the slight geometry modification of the three-electrode array. The paper shows different useful ways for representing the acquired resistivity data resulting from using such an adapted configuration. The conventional apparent traditional resistivity measurements ρ_{AB} have a poor resolution as compared with the gradient transformation, which shows in all the analyzed examples high resolution in all directions. Gradient transformation is moreover very sensible to the vertical boundaries of lithological variations, to the fractured and faulted zones, and can be therefore used as a qualitative helpful tool for interpreting traditional Vertical Electrical Sounding (VES) data. A maximum of geoelectical information can be gained when ρ_{AB}, gradient transformation, and $\rho_{AC/}$ ρ_{BC} are integrally interpreted as presented in this paper. The lithological variations of the sedimentary phosphatic environment in Al-Sharquieh deposit mine are characterized by using the proposed three-electrode array. Its efficient use can be advised in different applications in mineral and structural explorations.

Key words: Combined Sounding-Profiling Configuration; VES; Phosphate; Al-Sharquieh Mine; Syria.

J. Asfahani*
Atomic Energy Commission of Syria
Geology Department
P.O.Box. 6091, Damascus- Syria
*Corresponding author: jasfahani@aec.org.sy

Introduction

The electrical resistivity techniques are assumed to be of considerable importance especially for subsurface mineral and structural exploration because of very high resistivity contrasts among the lithological units, controlled study depth, and ease of field operations. One of those techniques is the vertical electrical sounding technique (VES). Although, different approaches have been already proposed for interpreting field VES measurements, confusion arises however in selecting the suitable approach for the quantitative VES interpretation. Each and every approach has some merits and demerits, hence no single interpretative method can give satisfactory results in all subsurface conditions. Efforts are therefore concentrated on improving and developing different appropriate interpretative techniques for interpreting the measured VES data. The selection of the appropriate VES interpretative technique depends on the lithology if it is simple or complex, and on the resistivity contrast in the study region (Asfahani, 2016). Considerable modifications on the traditional VES configurations themselves have been carried out in order to get as much as possible information with high resolution about the lithology of subsurface structures. The geoelectrical configuration, the survey direction and line spacing and the electrode spacing must be chosen as judiciously as we can to get the optimum geoelectrical results.

Different geoelectrical approaches such as the asymmetrical mirrored three-electrode arrays AMN and MNB have been consequently proposed and used in various presentations to detect different targets (Karous, 1982). Those approaches proved that two-sided three electrode configurations are more suitable than the classical full array (Schlumberger, Wenner) over a complex geology (Candansayar and Basokur, 2001). Karous and Pernu (1985) combined the sounding and profiling techniques by means of AMN and MNB half-Schlumberger arrays, and introduced a fast and approximate data processing technique named as 'gradient (G) transformation' to identify thin conductors. They proved the ability of this combined technique in detecting vertical contacts, such as dykes and steeply dipping faults. The profiling curves' inequality observed between the values of apparent resistivity by applying AMN and MNB array can be used to locate a resistivity heterogeneity along a given studied profile (Candansayar *et al*., 1999).

Schulz and Tezkan (1988) recorded simultaneously the Schlumberger and half-configurations to examine the dimensionality of the subsurface, and pointed out the superior resolving ability of two sided half-Schlumberger array. Hafizi (1998) detected fractures in a hard rock area using combined resistivity profiling and square array techniques. Candansayar and Basokur (2001) applied two sided three-electrode array to reveal small-scale targets. They examined the inversion results of 2-D of both traditional and asymmetrical apparent resistivity data. The inversion of 2-D of the two-sided three-electrode apparent resistivity data determines accurately the burial depth, the size, and location of the target. This findings proved that the three-electrode array has better resolution for detection of small targets compared to its four-electrode counterpart and dipole-dipole data.

The electrical resistivity methods have been introduced while prospecting for phosphatic resources in Syria (Asfahani and Mohammed, 2000). Traditional Vertical Electrical Sounding (VES) measurements using Schlumberger array were applied in Al-Sharquieh phosphate mine, and interpreted by different interpretative techniques (Asfahani and Mohammed, 2000; Asfahani, 2010). It was indicated that the task was made difficult by both the limitations of those techniques themselves and the complexity of the lithological section in the studied area.

Interpretation problems, such as non-uniqueness or suppression show that different geoelectrical input models can produce the same output model curve, and hence gives rise to ambiguity. Often the best-fitting model curve presents a good estimate of the true resistivity, since there are few options for generating alternate well-fitted curves. In other cases, however, the non-uniqueness is so complex, that other surveys, such as seismic or test wells are necessary to distinguish the correct structure from others. For example, for thin layers relative to the thickness of the overlying layer, the principle of equivalence will considerably affect the interpretation (Koefoed, 1979). The indication of those thin layers on the VES curve could be even absent due to the suppression principle (Koefoed, 1979). According to the equivalence principle, the thickness and resistivity cannot be determined from a sounding curve, but only their product, where T equivalence exists, or their quotient, where S equivalence holds, A unique interpretation for thickness or resistivity requires that one or the other should be determined using an independent method.

Other serious limitation in such electrical investigations as they fail to distinguish between formations of similar resistivities.

Scale limitations involving electrode spacings, depth of investigation and required resolution are also a drawback for resistivity soundings.

Interpretation of resistivity curves is made by a curve matching technique using master curves (Orellana and Mooney, 1966) for the initial determination of thicknesses and resistivities of corresponding layers (initial approximate model). The parameters of this approximate model were accurately interpreted using an inverse technique program, until a goodness of fit between the field curve and the theoretical regenerated curve was obtained (Zohdy, 1989; Zohdy and Bisdorf, 1989).

Correct quantitative interpretation requires two conditions to be satisfied: first, the calculations must be precise; second, a reasonable geological concept or model must be incorporated in the interpretation process. Disregard of either can have a serious negative impact on the validity of the results of a geoelectrical survey for any locality.

Present-day interpretation procedures are based on the assumption of a one-dimensional (1-D) medium. If this assumption is not satisfied, the interpretation results will be incorrect and a 2-D or 3-D approach must be adapted (Dey and Morrison, 1979).

The facies of phosphate deposits in Al-Sharquieh mine are characterized by very sharp changes in all directions (Asfahani, 2016). The curve matching method (CMM) (Orellana and Mooney, 1966) applied consequently for interpreting traditional VES data related to the study region has a quite poor resolution, such that we cannot identify on the logarithmic plots thin layers buried at depths more than five times their thickness. Many spurious results were produced, that caused difficulties during quantitative interpretation of the VES measurements. Asfahani (2010) modified the traditional geoelectrical Schlumberger configuration, developed and adapted a new structural interpretative approach aimed at enhancing the CMM.

Recently, Asfahani (2016) applied the inverse slope method (ISM) to reinterpret the same (VES) data measured in the Al-Sharquieh phosphate mine. It was found that ISM overcomes both the limitations of the CMM and the complexity of the lithological section.

The main objective of this paper is to apply geoelectrical combined sounding-profiling configuration for characterizing the sedimentary phosphatic rocks in Al-Sharquieh deposits mine in Syria. The combined three-electrode array suggested by Karous and Pernu (1985) is modified, adapted and applied in this work. The electrode C_∞ fixed and planted at the infinity is slightly modified to be movable in this present research, where OA=OB=OC= AB/2. The gradient transformation (G) developed by Karous and Pernu (1985) is consequently modified in order to take into consideration the slight geometry modification of the three-electrode array. The modified gradient transformation (G) under a given station is calculated as a function of AB/2, where the vertical variations of resistivity are traced.

Geological Setting

The Palmyrides is a 350 km long, NE–SW elongated ridge located in central Syria (Figure 1-a). The Southern and Northern Palmyrides are separated by an extensive internally-drained basin called the Daww basin filled with Neogene-Quaternary deposits. In the Palmyrides ridge, a sedimentary sequence from upper Triassic to Neogene is exposed and consists of several lithologic units, including the Soukhneh group. The Soukhneh group divided into two lithological formations (Rmah and Sawwaneh) is characterized by its significant phosphorite deposits and composed mainely of two rock types: calcareous and siliceous rocks. The calcareous rocks are dominated by limestone, marly limestone, limy marl, and marl with characteristic limy balls ranging in size from a few centimeters up to 2 m in diameter. The siliceous rocks are composed of thin-layered flint horizons or flint lenses and nodules. Figure 1-b shows a typical geological column of phosphatic deposits in Central Syria (modified by Jubeli, 1998 in the Reference list).

The phosphatic layers are thick in the central part of the Palmyrides, and thin eastward until they pinch out under the marly deposits of the Arak and Tantour formations. Two principal types A and B of phosphatic deposits exist in Syria (Figure 2-a); type A are related to the phosphates of the Late Cretaceous age, while type B are related to the early Eocene Syrian Desert phosphorites (Ponikarov, 1966). Khneiffis and Al-Sharquieh locations are the main mines in Syria for phosphate extractions (Figure 2-a). The phosphatic deposits in the region are attributed to enrichment processes involving phosphorus and plankton particles, which indicates a paleogeographic evolution related to Cenonian transgression and the subsidence of the Arabian Platform. In addition, the phosphatic deposits are associated with primary and

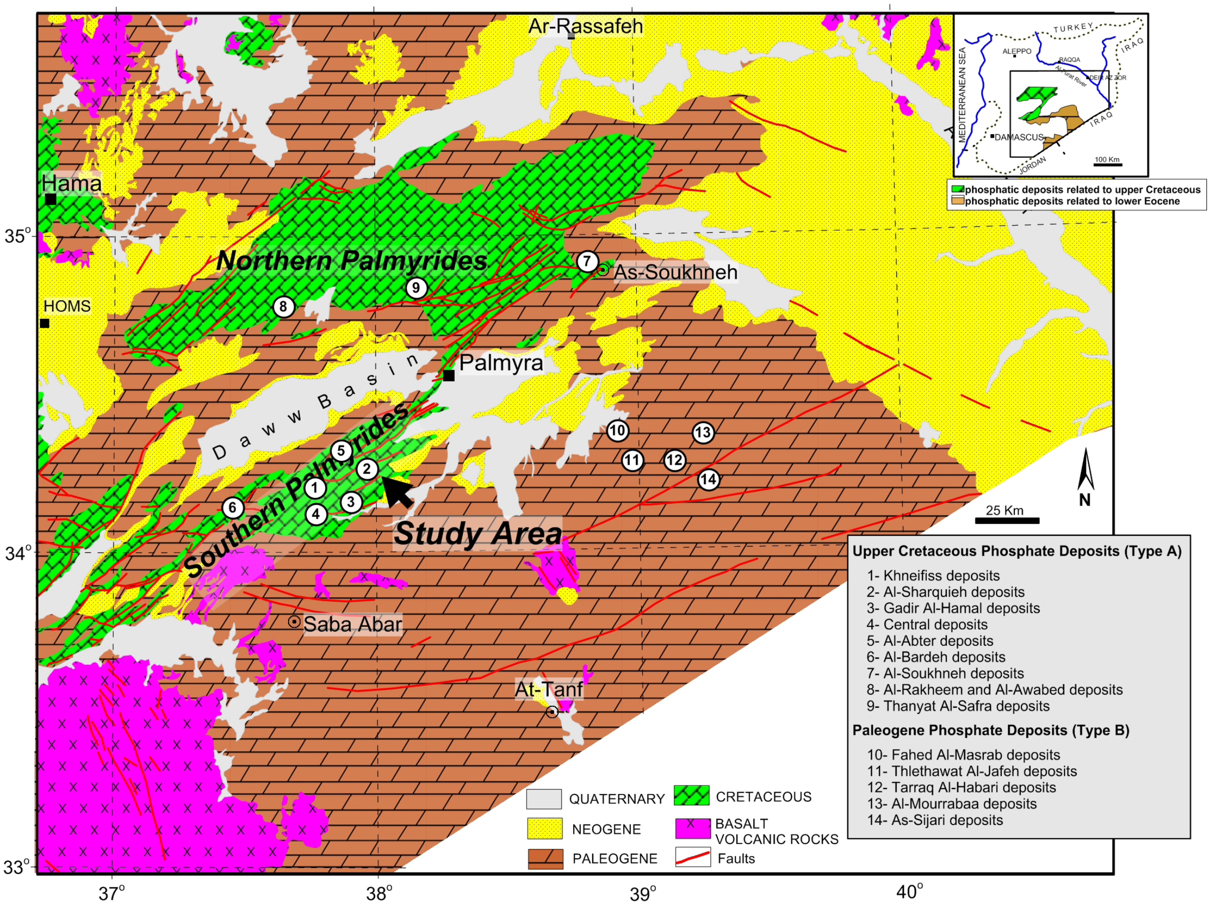

Figure 1-a. Phosphatic deposits in the Palmyrides region of central Syria, including the Al-Sharquieh mine (Asfahani, 2016).

secondary uranium mineralizations. The former are associated with phosphate precipitation while the later fills open cracks and pores, due to surface and subsurface percolation (Abbas, 1987).

The following facies are exposed at Al-Sharquieh mine (Asfahani and Mohamad, 2000):

- alluvial soil with calcareous rocks;
- calcareous clayey rocks accompanied by phosphate;
- phosphatic calcareous rocks;
- fractured dolomite;
- marl with interbedded clay;
- phosphatic sand; and
- cherty layers.

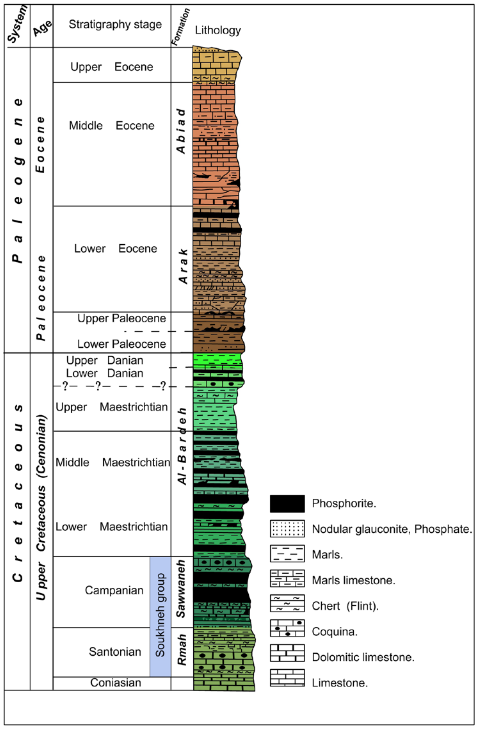

Figure 1-b. Geological column of phosphatic deposits in central Syria.

Description of the combined three electrodes system

The particular array of the three electrodes system is used in this paper as shown in Figure 2. A, B and C represent the electrodes of electrical current, while M and N show the location of the potential electrodes. The current electrodes A and B are planted at the left- and right hand sides of a pair of potential electrodes respectively. Electrode C is located along the line perpendicular to the centre of the measuring profile, where OA=OB=OC=AB/2. Two measurement sequences are executed for each position of potential electrodes. The first apparent resistivity measurements are obtained by applying an electrical current into ground through the C_1, C_2,…, C_n and A_1, A_2,…, A_n electrodes. The measurements are similarly repeated by using the C1, C2,…, C_n and B_1 ,B_2 ,… B_n electrodes. The values of apparent resistivity ρ_{AC} and ρ_{BC} obtained by using C_J-A_J and C_J-B_J current electrodes in pairs respectively constitute the left and right apparent resistivity values corresponding to the same potential electrode pair (M and N). This procedure allows obtaining the resistivity variation as a function of depth (AB/2). Shifting the potential electrodes to the next electrode locations and repeating the same measuring sequence, a set of apparent resistivity values along the measuring line are acquired, and the resistivity section is obtained.

Simultaneous execution of profiling and VES surveys along a given profile results in combined sounding-profiling data, which allows detailed investigations about the study area to be obtained.

The apparent resistivity ρ_{AC} can be defined as:

$$\rho_{AC} = \frac{K_{AC} * V_{AMN}}{I} \qquad (1)$$

where ΔV_{AMN} , is the potential difference between M and N electrodes caused by the current (I) applied through the source (A) and (C) electrodes. The geometric factor, K_{AC} of the array is given by the equation:

$$K_{AC} = \frac{2\pi}{\frac{1}{AM} - \frac{1}{AN} - \frac{1}{CM} + \frac{1}{CN}} \qquad (2)$$

The apparent resistivity ρ_{BC} corresponding to the case where the current is applied through B and C electrodes is obtained in a similar way as for ρ_{AC} , where the geometric factor K_{BC} is equal to K_{AC}, being $CM=CN$.

Considering the conventional application where the current is injected through A and B electrodes, the following equations can be obtained for the apparent resistivity ρ_{AB} :

$$\rho_{AB} = K_{AB} \frac{V_{MN}}{I} \qquad (3)$$

Where $$K_{AC} = K_{BC} = 2K_{AB} \qquad (4)$$

It is noteworthy to mention that apparent resistivity ρ_{AB} can be directly computed from the two other apparent resistivity values ρ_{AC} and ρ_{BC}. This is a direct implication of the superposition rule without actually measuring the potential difference (Karous and Pernu, 1985).

After some algebraic arrangements, equation (4) yields

$$\rho_{AB} = \frac{\rho_{AC} + \rho_{BC}}{2} \qquad (5)$$

thus the resistivity "ρ_{AB}" is called "average apparent resistivity".

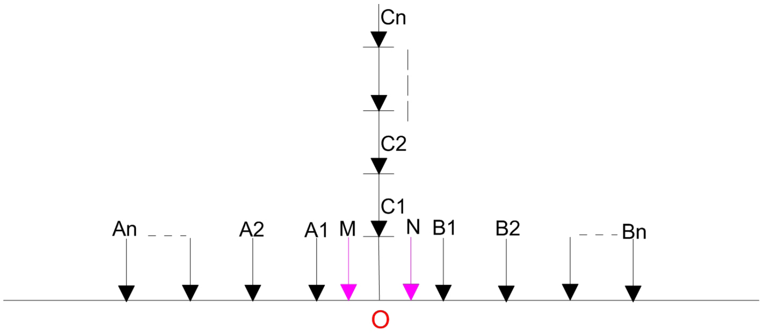

Figure 2. Schema of the combined sounding- profiling configuration (two three electrode configurations AMN and MNB). A, B and C: current electrodes, M and N: potential electrodes, O: configuration center.

The 16 separations of the current electrodes used in this research are: OA=OB=OC=AB/2: 1.13, 1.68 , 2.18 , 3.66 , 4.74 , 6.15 , 7.96 , 10.33 , 13.38 , 17.35 , 22.49 , 37.75 , 48.78, 63.48, 82.27 and 106.6 m. Several geoelectrical field essays have been tested, and aimed at determining the appropriate electrode spacings AB/2 for carrying out shallow VES, where it has been found that the mentioned seperations give good results in concordance with the geology. Those spacing distances were purposely selected and tested to apply shallow combined VES, where more shallow lithological details are required in the studied area. The phosphatic layer is also reached and characterized by such spacing distances. The potential electrode separations were 0.2, 1.5 , and 20 m.

Data acquisition

A database consisting of 45 vertical electrical soundings VES points have been used, measured at the available 45 drilled pits in the study area. At each drilled pit, a lithological description was carried out with a radioactive measurement using the total natural gamma ray technique. Those pits were also measured by applying the shallow VES. The usefulness of those VES in the definition of shallow phosphatic structures is already well established (Asfahani, 2010). The Terrameter SAS 300B with Booster Terrameter SAS 2000 was used to measure the traditional VES, and the combined VES. The resistance ($\Delta V/I$) is directly measured, and apparent resistivities ρ_{AB}, ρ_{AC} and ρ_{BC} are subsequently computed according to equations (1) and (3) (Dobrin, 1976). The apparent resistivity values ρ_{AB}, ρ_{AC} and ρ_{BC} obtained by increasing the electrode spacing about a fixed point were plotted versus half electrode separation AB/2 to establish three field resistivity curves ρ_{AB}, ρ_{AC} and ρ_{BC}.

Gradient transformation (G)

The discrepancy between the values of apparent resistivity ρ_{AC} and ρ_{BC} obtained from the corresponding AMN and MNB configurations may be used to locate a resistivity inhomogeneity along the profile.

Karous and Pernu (1985) defined the gradient transformation "G" as

$$G^i(x) = \frac{\rho_A^i(x)}{\rho_A^{i+1}(x)} + \frac{\rho_B^i(x)}{\rho_B^{i-1}(x)} - 2(i = 2,3,...,L-1) \tag{6}$$

where *x* is AB/2 the spacing along the profile and *L* denotes the key numbers of measurement stations along the profile. All apparent resistivity values in equation (6) are measured for the same AO = BO= AB/2 spacing, where C_∞ is located at infinity. The increasing or decreasing of the G values depends on the discrepancy between the apparent values measured by the AMN and BMN configurations. Thus, the value of G becomes proportional to the resistivity variation in the horizontal direction.

In the present research, the above equation is adapted and slightly modified to calculate the gradient "G" as a function of AB/2, where AO = BO= CO= AB/2 as follows:

$$G(AB/2)_i = \frac{1}{2}\ \frac{\rho_{AC}(AB/2)_{i-1} + \rho_{AC}(AB/2)_i}{\rho_{AC}(AB/2)_{i+1} + \rho_{AC}(AB/2)_{i+2}} + \frac{\rho_{BC}(AB/2)_{i+1} + \rho_{BC}(AB/2)_i}{\rho_{BC}(AB/2)_{i-1} + \rho_{BC}(AB/2)_{i-2}} - 2$$

$$(i=1,2,...,16) \tag{7}$$

The computed "G" in such a case becomes proportional to the resistivity variation in the vertical direction, and is very sensitive to the vertical lithological boundaries. It can be therefore used for interpreting the traditional VES.

A measured line is covered at regular interval Δx (separation between subsequent dipole centers O (x^k)), which is equal to 200 m in the present research. The recording station at a given survey line coordinates three resistivities ρ^k_{AB}, ρ^k_{AC}, and ρ^k_{BC} for a given AB/2. A simultaneous execution of profiling and sounding surveys result in combined sounding- profiling data, which allows us to obtain detailed data about the study area. The measured resistivity data obtained by applying this technique describes the resistivity distribution below the measured line. The resistivity results thus obtained can be presented in the simplest and most instructive form to indicate clearly the true distribution of resistivities under the studied survey line. The profile curves are obtained through plotting the values of resistivities ρ^k_{AB}, ρ^k_{AC}, and ρ^k_{BC} and G^k for a given AB/2 as a function of the station coordinates x^k . At every station x^k, three sounding curves could also be obtained by plotting the apparent resistivities of ρ^k_{AB}, ρ^k_{AC}, and ρ^k_{BC} and G^k as a function of AB/2 as will be shown below.

Ratio (ρ_{AC}/ρ_{BC})

The ratio of ρ_{AC}/ρ_{BC} is also introduced in this research. It is inspired from the resistivity profiling using the Lee configuration aimed towards detecting the locations of the points of non-homogeneity (Asfahani *et al*., 2010), which could be interpreted and attributed to faults and fractures. The Lee configuration includes the use of five electrodes AMONB placed on a straight line on the ground (where OM = ON). Three resistivities were measured by applying this array as follows: traditional resistivity ρ_{MN}, and two other resistivities ρ_{OM} and ρ_{ON}, were measured between OM and ON respectively. The ratio of ρ_{OM}/ρ_{ON} has already been used to characterize the heterogeneity and lithological variations in the studied Qastoon Dam (Asfahani *et al*., 2010). The resistivity ratio of ρ_{OM}/ρ_{ON} = 1, indicates an homogeneous medium between M and N electrodes. Ratio values deviating from 1 reflect a sharp geoelectrical contrast between adjacent media of different electrical characteristics, caused mainly by lithological variations, faults and fractures. In the present paper, the application of the above mentioned rule is adapted for analyzing the ratio of ρ_{AC} / ρ_{BC}, which will be presented in form of profilings and maps. This procedure helps in getting additional lithological and structural information about the heterogeneity and homogeneity of the medium in the studied area. This consequently guides and orients the geochemical explorations towards the heterogeneous phosphatic area, to take samples for analysis .

Results and Discussion

Forty five combined electrical resistivity soundings with the three electrodes configuration were measured at the 45 drilled pits, distributed in the study area along several profiles as presented in Figure 3. At each drilled pit, a radioactive measurement using the total natural gamma ray technique and a shallow combined VES were applied, with providing the lithological description. Such a lithological description is usefully employed for correlating the variations of different geoelectrical parameters obtained by the new shallow combined VES with the lithology as a function of depth. Those variations are also laterally correlated along the different studied profiles in the study area.

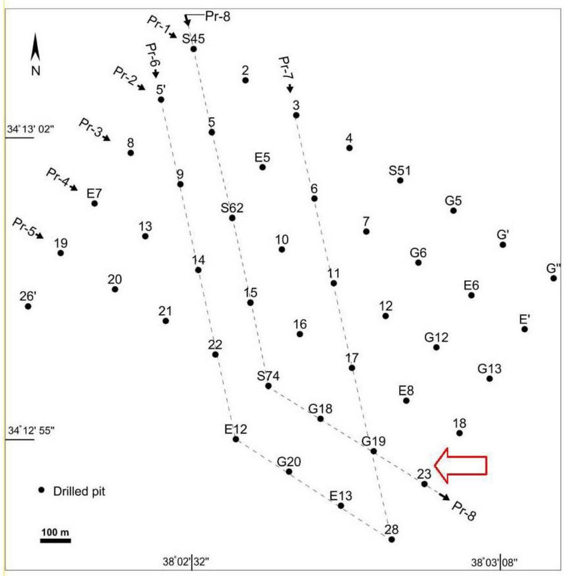

Figure 3. Locations of drilled pits and the combined VES soundings at the Al-Sharquieh mine.

Figure 4 shows the lithological description of pit No. 23 (Figure 3) and the total radioactivity gamma ray measurement taken from the interior of this pit. The radioactivity in this pit reaches its maximum value of 400 cps, which indicates the presence of phosphatic layers. An example of combined geoelectrical VES measurements carried out at the same pit No. 23 is also presented in Figure 5a, where three resistivities are shown: the traditional Schlumberger ρ_{AB}, and both ρ_{AC}, and ρ_{BC}. This figure gives an idea on the behavior of ρ_{AC} and ρ_{BC} as a function of the spacing AB/2, where their variations, as a function of depth, reflect the lithological variations at the studied VES point. Their maximum divergences are located basically in the range of AB/2 between 10 and

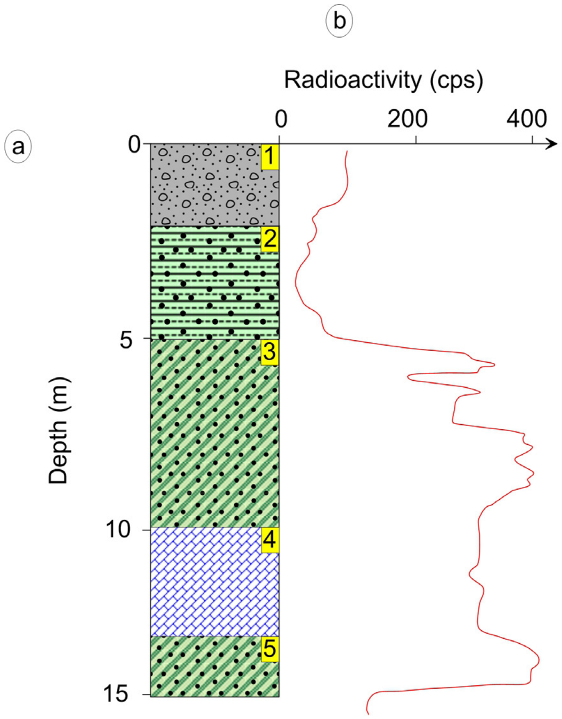

Figure 4. a): Lithological description of pit No:23, b): Natural radioactive gamma measurement at pit No:23. 1: Quaternary alluvium, 2: clay with phosphate, 3: phosphate sand, 4: limestone clay, 5: phosphate sand.

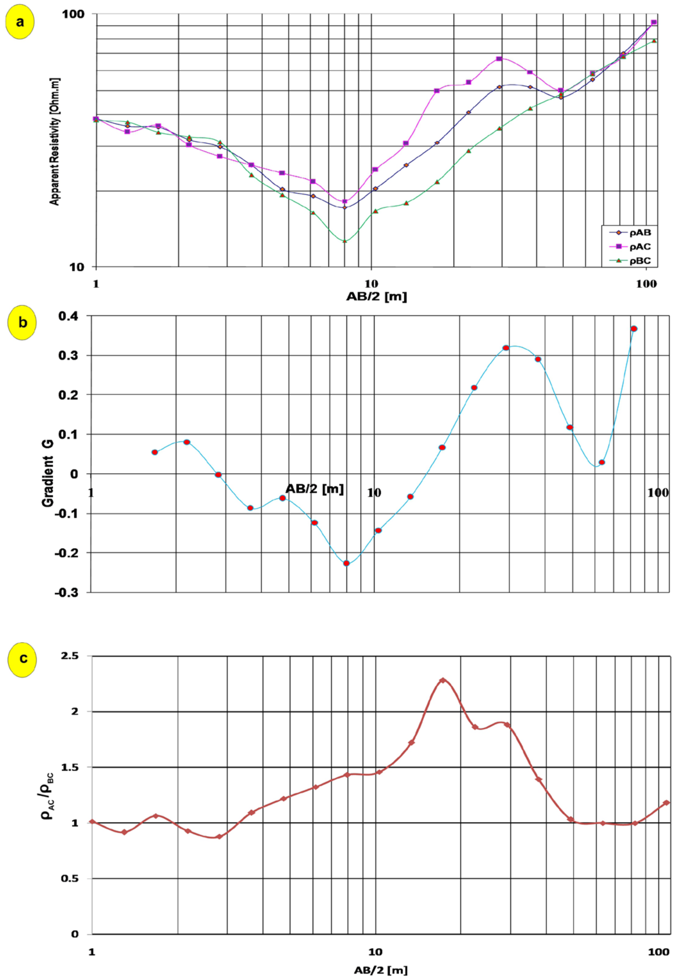

Figure 5. a) Traditional apparent resistivity ρ_{AB}, ρ_{AC}, and ρ_{BC} obtained by the combined VES sounding at pit No:23. b) Gradient G at pit No:23, and c) ratio of ρ_{AC}/ρ_{BC} at pit No:23.

50 m, while their minimum divergences are located in the range of AB/2 between 50 and 106.6 m. The variations of both the gradient (G) and the ratio of (ρ_{AC}/ρ_{BC}) as a function of AB/2 for the pit No. 23 are also shown in Figure 5(b, and c). The analysis of ρ_{AC}/ρ_{BC}) helps in getting more information about the heterogeneity of the medium in the study area in lateral and vertical directions.

Figure 6 shows the vertical variations' maps of the measured traditional apparent resistivity presented as (Log ρ_{AB}), the gradient transformation (G), and the ratio (ρ_{AC}/ρ_{BC}), along profiles Pr-1 and Pr-5 as a function of the spacings AB/2, which vary from 1.13 to 106.6 m. Those maps have been established by using the interpolation Krige technique. It is the most frequently used for spatial interpolation, and based on linear interpolation combined with the mean square estimate error minimization (Krige, 1951). The logarithmic scale is used in this paper, because the original measured resistivity data of the traditional Schlumberger ρ_{AB} for these two profiles indicate only the presence of two resistive and conductive zones, which is difficult to be solely interpreted in geological and lithological terms. In fact, The measured traditional Schlumberger resistivity values ρ_{AB} in the study region have log-normal behavior, and the use of the logarithmic scale improves relatively, in such a case study, the resolution of the traditional resistivity data ρ_{AB}. The resistive and conductive zones are related to the presence of phosphate layers and clays respectively. The electrical resistivity increases with increasing phosphate content, and decreases with increasing clay content (Asfahani and Mohamad, 2000). The highest resistivity values are observed in the study area in the NW direction, where phosphatic beds are thinner and occur at or near surface (Asfahani, 2010).

Both gradient (G) maps of Pr-1 and Pr-5 developed in this paper (Figure 6) clearly show a vertical lithological distinction in the conductive zone of ρ_{AB}, meaning that the (G) parameter has a strong vertical resolution in comparison to the traditional ρ_{AB} of a poor resolution. The results of (G) maps particularly along the Pr-5 are in a remarkable concordance with those already presented and published by Asfahani (2010) (Figure7). The faults and fractured zones shown in all the maps presented in Figure 6 are inferred from Figure 7.

Figure 7 shows the interpretations of shallow VES, distributed along the two Pr-1 and Pr-5 profiles, by using the Pichgin and Habibullaev technique (Pichgin and Habibullaev, 1985) and the concept of the points of non homogeneity (PNH). The positions of the faults and the fractured zones were precisely determined along those two profiles by using the strict rules required according to this technique (Asfahani, 2010).

A clear vertical stratification is observed particularly under VES- G19 and VES-S74, where four different stratified values of gradient (G) reflect the presence of Quaternary alluvium, shaley calcite, altered phosphate rocks, and cherty bed rocks. The fractured zone between VES-22 and VES-G18 along Pr-5, which has been already determined by Asfahani (2010)

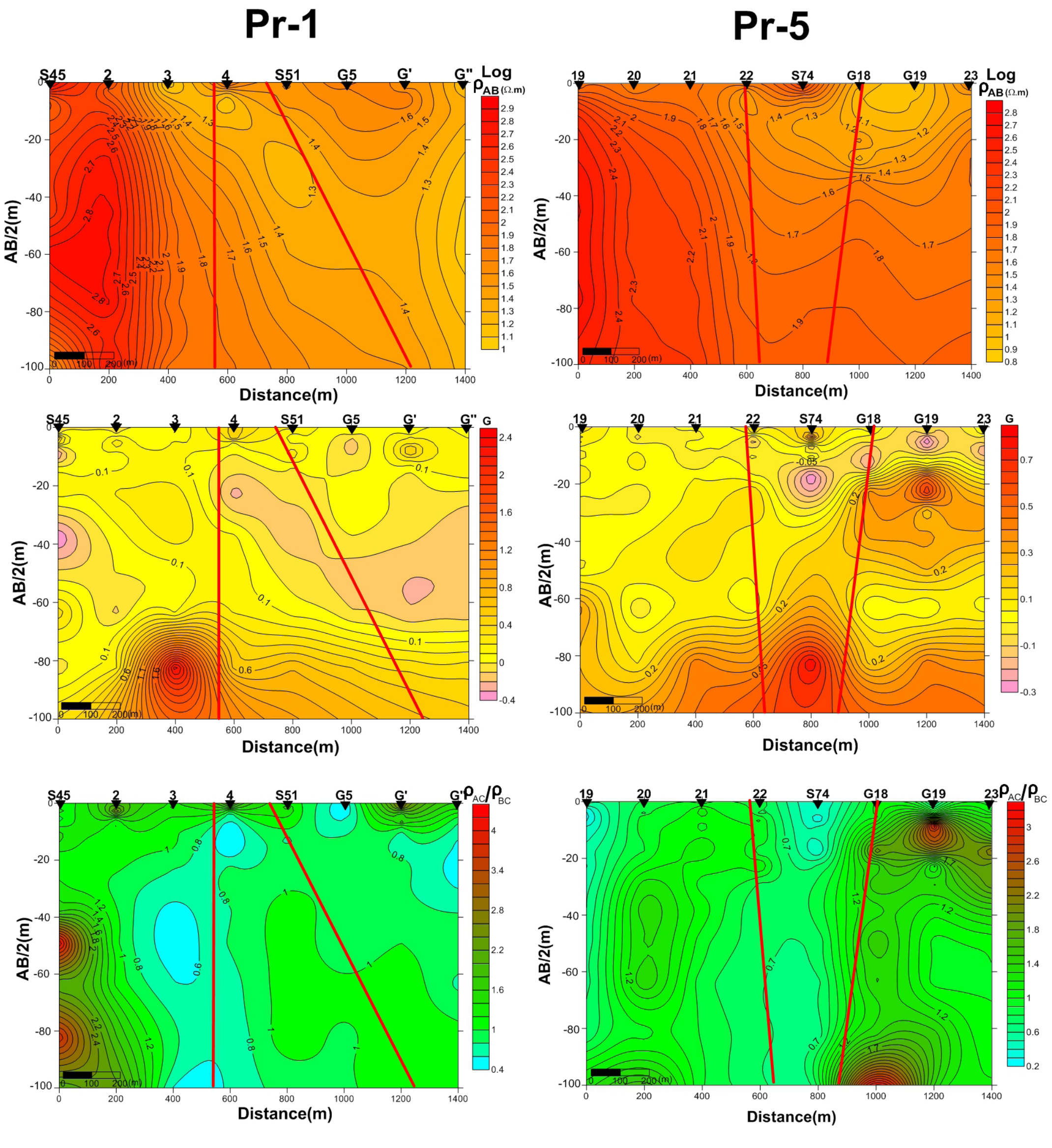

Figure 6. Vertical variation' maps of traditional ρ_{AB} , G, and ρ_{AC}/ρ_{BC} as a function of AB/2 obtained along Pr-1 and Pr-5.

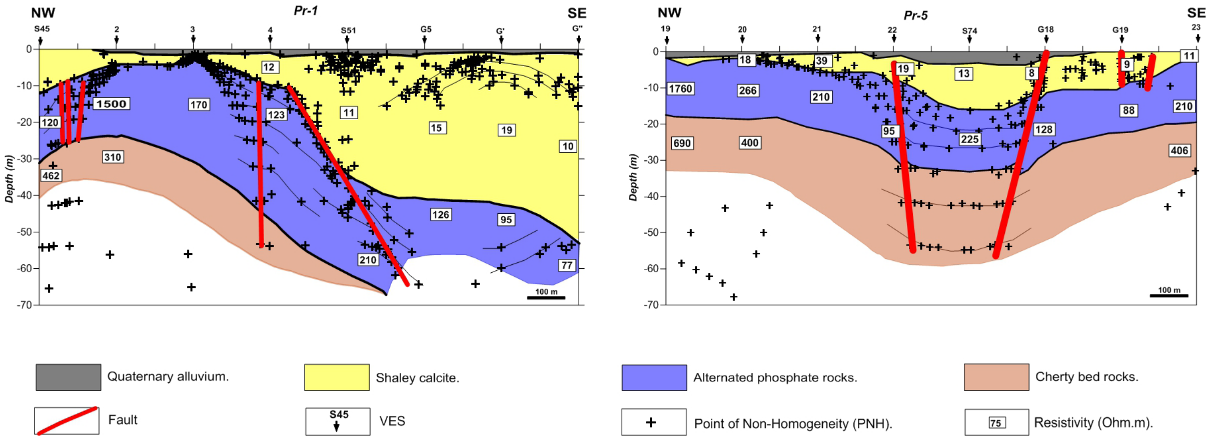

Figure 7. Quantitative interpreted shallow geological cross-sections for traditional VES profiles (Pr-1 and Pr-5) from Al-Sharquieh mine (Asfahani, 2010).

(Figure 7) is clear and also indicated herein by the gradient (G) (Figure 6). The vertical ratio of (ρ_{AC}/ρ_{BC}) map along Pr-5 helps also in getting more information about the lithological and structural variations. The fractured zone between VES-22 and VES-G18 is characterized by a (ρ_{AC}/ρ_{BC}) equal or less than 1. The influence of the already determined fault (Asfahani, 2010) under VES-22 is less clear than the one determined under VES-G18, where high values of the ratio (ρ_{AC}/ρ_{BC}) reaching more than 3.5 are observed under VES- G18, VES- G19 and VES-23 in the SE direction. The comparison between the quantitative interpretation along Pr-1 and Pr-5 (Asfahani, 2010) and the qualitative ones presented in this paper indicate an acceptable similarity between the two different interpretations. This similarity proves the accuracy of the adapted quantitative lithological model shown and presented in Figure 7, and the high resolution of both the gradient (G) and the ratio (ρ_{AC}/ρ_{BC}) (Figure 6). The accuracy of (G) and (ρ_{AC}/ρ_{BC}) facilitates the analysis and the interpretation of the phosphate profiles in the study region, by providing clear lithological differentiations laterally and vertically.

Figures 8 (a and b) show the profiling variations of the measured traditional resistivity data (ρ_{AB}), the gradient (G), and the ratio (ρ_{AC}/ρ_{BC}) along the profile Pr-5 for both spacings AB/2 of 22.49 and 29.15 m. One can easily notice how both the developed parameters (G) and (ρ_{AC}/ρ_{BC}) are more sensitive than the traditional apparent resistivity (ρ_{AB}) parameter to the fractured zone already located between VES-22 and VES-G18 as presented in Figure 7. In fact, (G) and (ρ_{AC}/ρ_{BC}) show a notable decrease in the fractured zone particularly for AB/2 of 22.49 m, while no variations in the values of ρ_{AB} are observed.

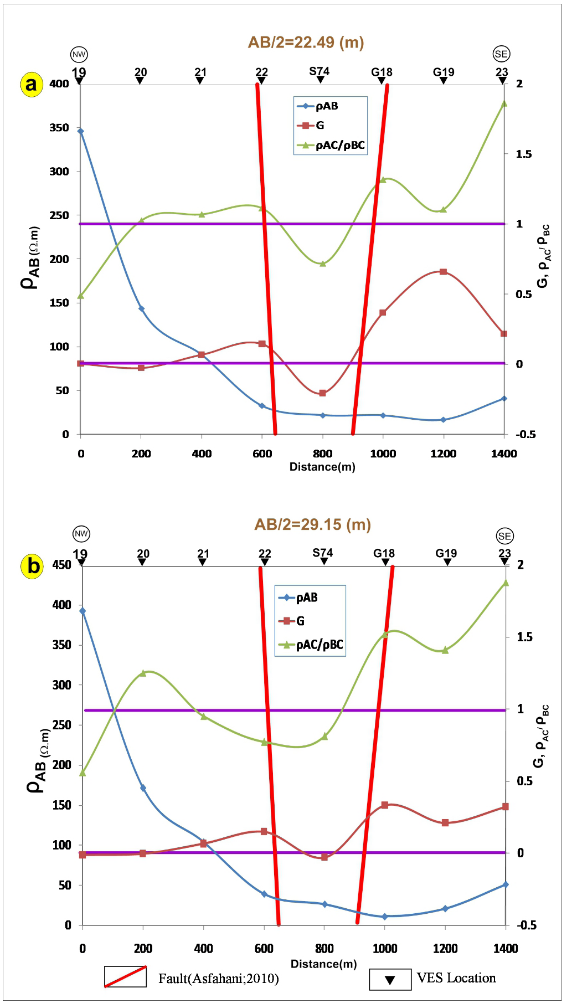

Figure 8. a) Profiling variations of ρ_{AB}, G, and ρ_{AC}/ρ_{BC} along Pr-5 for AB/2 of 22.49 m. b) Profiling variations of ρ_{AB}, G, and ρ_{AC}/ρ_{BC} along Pr-5 for AB/2 of 29.15 m.

Figure 9 shows the variation's maps of traditional apparent resistivity data (Log ρ_{AB}), (G), and (ρ_{AC}/ρ_{BC}) related to the studied area for only different spacings of AB/2 of 3.66, 17.35, 37.78 and 82.28 m. The raw measured resistivity data of ρ_{AB} for AB/2 of 3.66 m indicates in its best case high resistive zone in the NW direction, while the whole study area for this AB/2 is characterized by relatively low resistivity not exceeding 120 Ω.m. The measured resistivity ρ_{AB} being of very low resolution, this explains the reason behind using the logarithmic scale (Log ρ_{AB}) (Figure 9) as discussed above. The use of such a logarithmic scale increases considerably the resolution of the measured resistivity data. The increased resolution of (Log ρ_{AB}) allows better comparisons with other two developed parameters (G) and (ρ_{AC}/ρ_{BC}) to get easily and integrally a complete interpretative picture of the studied profile as presented in Figure 9. The analysis of (G) for this AB/2 of 3.66 m reflects different geological situation, where a positive (G) concentrated on VES 17 is surrounded by negative G, indicating different lithological variations corresponding to this AB/2.

The logarithmic traditional resistivity map of (Log ρ_{AB}) for AB/2 of 17.35 m shows two distinct zones of low and high resistivity. The map of (G) for this AB/2 of 17.35 m shows, in the zone of low resistivity, two positive gradient G concentrated on VES 12 and G19, separated by negative gradient G concentrated on VES 17. The ratio map of (ρ_{AC}/ρ_{BC}) for this AB/2 of 17.35 m shows a high value reaching 3.6 concentrated on VES 17.

The same geological picture is observed while studying the variation's maps of (Log ρ_{AB}), (G), and (ρ_{AC}/ρ_{BC}) for AB/2 of 37.78 m. Nothing is shown on the logarithmic traditional (Log ρ_{AB}) map except two relatively high and low resistivity distributions. The map of (G) for AB/2 of 37.78 m shows clearly a positive distinct structure of G concentrated on VES 17.

The map of (ρ_{AC}/ρ_{BC}) for this AB/2 of 37.78 m shows two high anomalies concentrated on G12 and E13.

The (G) and (ρ_{AC}/ρ_{BC}) maps show good lateral resolutions for the studied area for AB/2 of 82.28 m, in comparison with the logarithmic traditional apparent resistivity (Log ρ_{AB}) map of relatively poor resolution.

It is important to mention in the present case study the small range values of both developed parameters, the gradient (G) and the ratio (ρ_{AC}/ρ_{BC}) for all the established maps, shown in Figure 9, in comparison with the high range values of apparent measured traditional resistivity (ρ_{AB}) . The logarithmic behavior scale for the traditional resistivity (Log ρ_{AB}) values is therefore preferable as compared with the simple linear resistivity scale. In such a logarithmic scale, the resolution of the traditional resistivity maps (Log ρ_{AB}) is relatively better, where acceptable comparisons could be easily made with both maps of (G) and (ρ_{AC}/ρ_{BC}) as presented in Figure 9.

The above comparisons between different parameters of (Log ρ_{AB}) , (G), and (ρ_{AC}/ρ_{BC}) show good examples of the limitations of the traditional lateral and vertical apparent resistivity maps of (ρ_{AB}) if they are used solely. The advantages and the remarkable sensibility and resolution of the developed gradient parameter (G) for the lithological and structural variations in phosphatic environment are well demonstrated and documented.

Figure 10 resumes the structural and geological fence diagram showing lateral variations of the phosphatic layer in the study area at Al-Sharquieh mine. This diagram is obtained through interpreting the shallow Schlumberger configuration with different interpretative methods (Asfahani, 2010). The geological field surveys indicate also that the locations of the identified faults and the fractured zones are characterized by high radioactivity, due to secondary uranium concentrations introduced by ground waters along fracture zones (Asfahani, 2010).

The delineation of the presence of faults and fracture zones through interpreting the shallow Schlumberger resistivity data is an indirect guide for uranium prospecting in such phosphatic environments.

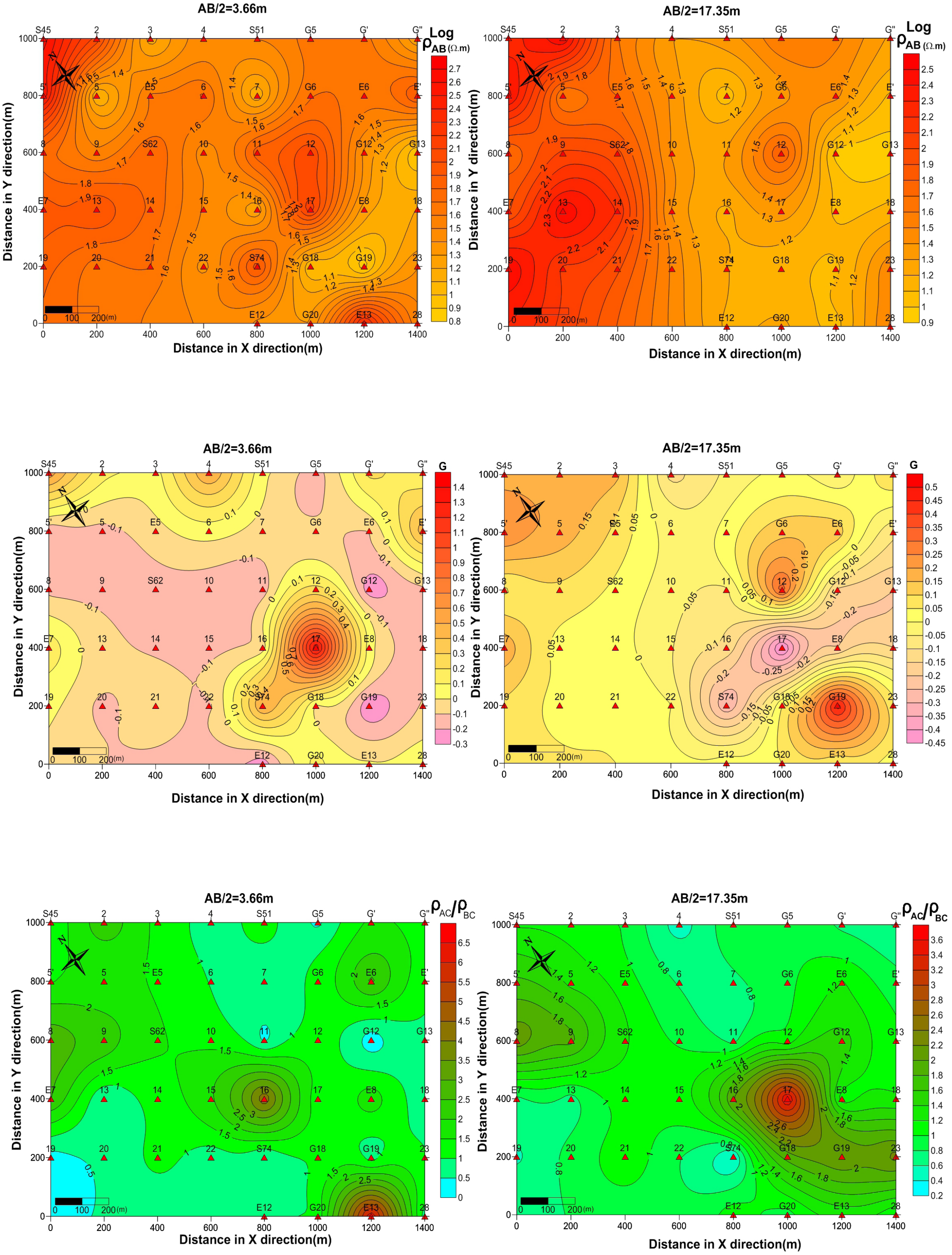

Figure 9. Variation' maps of ρ_{AB}, G, and ρ_{AC}/ρ_{BC} for the study area for AB/2 of 3.66, 17.35, 37.78 and 82.28 m.

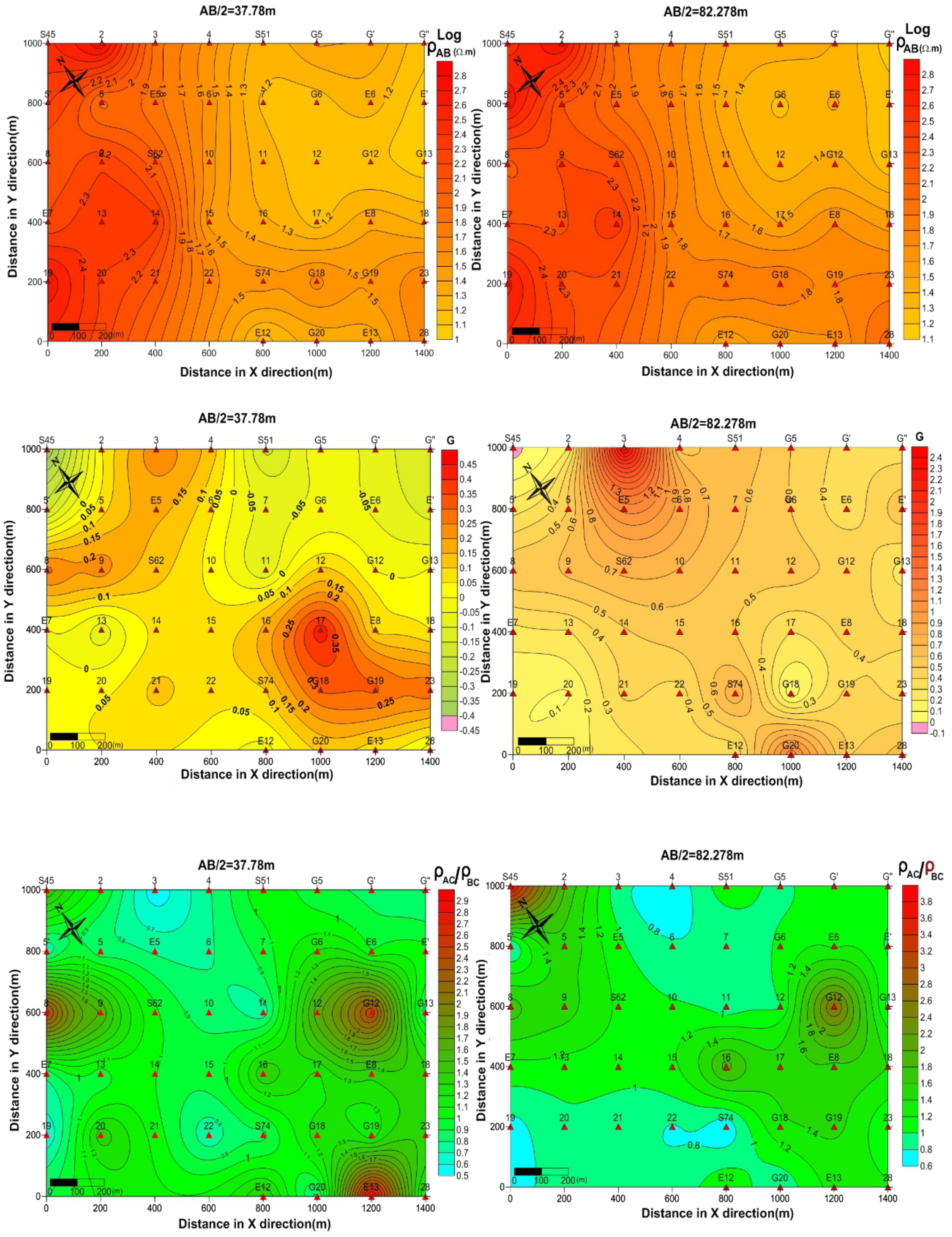

Figure 9. Continue.

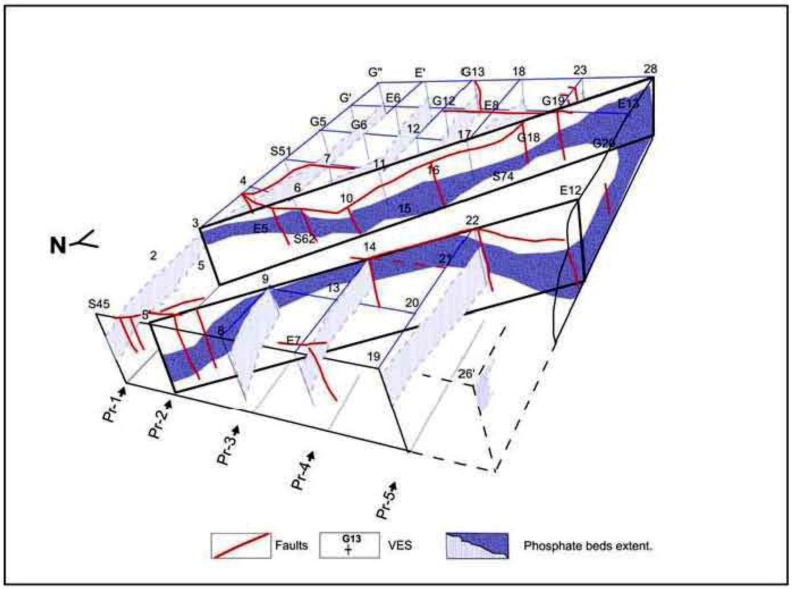

Figure 10. Structural and geological fence diagram showing lateral variations of the phosphatic layer in the study area at Al-Sharquieh mine, based on the interpretations of shallow VES configuration (Asfahani, 2010).

Conclusion

Shallow geoelectrical combined sounding-profiling configuration was adapted and proposed in this research to characterize the phosphate deposits in Al-Sharquieh mine in Syria. Its results application allows us to make the following conclusions:

1.- The high vertical resolution of the computed gradient parameter (G) of the modified combined sounding-profiling configuration is obtained compared with the traditional apparent resistivity Schlumberger (ρ_{AB}),which yields poor resolution.

2.- The traditional resistivity measurements (ρ_{AB}) in the study area have a logarithmic behavior. The logarithmic scale is therefore preferable (Log ρ_{AB}) for establishing the different traditional resistivity maps, as documented above. This scale improves relatively the resolution of the resistivity data (ρ_{AB}), where acceptable comparisons could be easily made with both the gradient (G) and the ratio (ρ_{AC}/ρ_{BC}).

3.- The high sensitivity of the computed parameter (G) for the vertical lithological boundaries helps in any quantitative interpretation of the traditional VES data.

4.- The adapted geoelectrical combined sounding-profiling configuration is sensitive to fractured and faulted zones.

5.- The determination of faults and fracture zones in the study area by the new shallow adapted combined array is a useful indirect guide for uranium prospecting in such a phosphatic environment.

6.- Different maps were used to represent the results of the traditional resistivity (Log ρ_{AB}), (G), and (ρ_{AC}/ρ_{BC}) allowing integrated qualitative interpretations.

7.- The sole interpretation of traditional resistivity measurements (ρ_{AB}) in the form of profiling and map resulted in very poor resolution and does not give sufficient clarity of the lithological and real resistivity distributions in the study area. The interpretation which combines additional different parameters such as (G), and (ρ_{AC}/ρ_{BC}) allows better resistivity and lithological distribution.

8.- It is proven in this research paper that the combined soundings and the subsequent analysis of (G) and (ρ_{AC}/ρ_{BC}) data are important tools to improve the resolution of the geoelectrical interpretation.

9.- The combined three electrodes configuration adapted in this research is recommended for other different applications in mineral and structural exploration.

Acknowledgment

The author would like to thank Dr. I. Othman, General Director of Syrian Atomic Energy Commission for his permission to publish this research. The two anonymous reviewers and the editor of Geofisica internacional Dr. Rene E. Chavez are cordially thanked for their professional suggestions and constructive remarks that considerably improved the final version of this paper.

References

Abbas M., 1987, Geochemie de l'uranium des phosphorites des Palmyrides Centrals, Syrie: These Sci., Univ., Louis Pasteur Strasbourg, France, 166 p.

Asfahani J., Mohamad R., 2000, Investigation of electrical properties of radioactive phosphatic layers in Al-Sharquieh mine, Syria. *Exploration and Mining Geology, 9*, 141–148.

Asfahani J., RadwanY., Layyous I., 2010, Integrated geophysical and morphotectonic survey of the impact of Ghab extensional tectonics on the Qastoon dam, Northwestern Syria. Pure and Applied Geophysics, 167, 323–338.

Asfahani J., 2010, Geophysical case study of shallow and deep structures based on traditional and modified interpretation methods: Application to tectonic studies and mineral exploration. *Exploration and Mining Geology, 19*(3–4), 135–152.

Asfahani J., 2016, Inverse slope method for interpreting vertical elecrtical soundings in sedimentary phosphatic environments in the Al- Sharquieh mine, Syria. CIM Journal*, Vol.7, No.2, 93-104.*

Candansayar M. E., Basokur A. T., Peksen E., 1999, Detecting small scale targets by the two-sided gradient transformation. J. Balkan Geophys. Vol.**2**, No. 4. P.100-111.

Candansayar M. E., Basokur A. T., 2001, Detecting small scale targets by the 2D inversion of two-sided three-electrode data: application to an archaeological survey. Geophys Prospecting. 49, P 13-25.

Dey H., Morrison H., 1979, Resistivity modeling for arbitrarily shaped 3-D structures. Geophysics 44 (4), 753.

Dobrin M. B., 1976, Introduction to geophysical prospecting: New York, NY: Mc Graw-Hill.

Hafizi M. K., 1998, Fracture detection in hard rocks using combined resistivity profiling and square array technique. EAGE 60th conference and technical exhibition. Leipzig, Germany.

Jubeli Y., 1998, The role of airborne radiometric survey in defining the distribution of phosphate rocks in Syria desert and the northern Palmyrides. Explor. Min. Geol. 6(3), 269-278.

Karous M., 1982, Gradient curves in resistivity methods with asymmetrical arrangements of electrodes. University of Oulu, Department of Geophysics, Report No. 3, 23 pp.

Karous M., PernuT. K., 1985, Combined sounding profiling resistivity measurements with the three-electrode arrays.Geophysical Prospecting, **33**, 447-459.

Koefoed O., 1979, Geosounding principles (Elsevier, Amesterdam) P. 420.

Krige D.G., 1951, A statistical approach to some basic mine valuation problems on the Witwatersand. Journal of the Chemical, Metallurgical and Mining Society of South Africa, 2(6), 119-139.

Orellana E., Mooney H.M., 1966, Master tables and curves for vertical electrical sounding over layered structures, interciencia, Madrid, Spain.

Pichgin, N.I., Habibullaev I.KH. , 1985, Methodological Recomendations in studying geo- tectonic conditions of vertical electrical soundings data with application of EC computer for solving hydrogeological and geo-engineering problems. Tashkend. (in Russian).

Ponikarov V. P., 1966, The Geological Map of Syria, scale 1:200000, sheets I-37-XIX and I-36-XXIV, Ministry of Industry, Damascus.

Schulz R., Tezkan B., 1988, Interpretation of Resistivity measurements over 2D structures. Geophys. Prospecting. **36**, P. 962-975.

Zohdy A.A.R., 1989, A new method for the automatic interpretation of Schlumberger and Wenner sounding curves. Geophysics 54, 245–253.

Zohdy A.A.R. , Bisdorf, R.J. , 1989, Schlumberger Sounding Data Processing and Interpretation Program, US Geological Survey, Denver.

Geofísica Internacional (2018) 57-3: 205-222

Original paper

A Graphic Processing Unit (GPU) based implementation of an incompressible two-phase flow model in porous media

V. Leonardo Teja-Juárez* and Luis M. de la Cruz

Received: March 14, 2018; accepted: May 23, 2018; published on line: July 02, 2018

Resumen

En este trabajo se presenta una estrategia de paralelización de un simulador completamente implícito para la solución numérica del modelo de flujo bifásico incompresible en medios porosos usando unidades de procesamiento gráfico (GPU, por sus siglas en inglés). El modelo matemático está basado en las ecuaciones de conservación de masa para las fases agua y aceite. Se utiliza la formulación Presión-Saturación para simplificar el modelo numérico. La técnica de Volumen Finito y el método de Newton-Raphson se usan para discretizar y linealizar las ecuaciones diferenciales parciales, respectivamente. Se propone la construcción del Jacobiano directamente en la GPU, lo que reduce la información que debe intercambiarse entre la CPU (Unidad Central de Procesamiento CPU, por sus siglas en inglés) y la GPU. El simulador utiliza bibliotecas que ya incluyen los métodos del subespacio de Krylov para resolver sistemas de ecuaciones lineales. Se comparan los resultados de tres problemas de referencia utilizando diferentes tamaños de malla. También se evalúa el rendimiento del código numérico desarrollado. Los resultados de la GPU versus CPU indican que el simulador numérico alcanzó hasta 22x de aceleración para construir el Jacobiano y 3x de aceleración para ejecutar el código numérico completo usando la paralelización GPU.

Palabras clave: Modelo bifásico, Newton-Raphson, Unidades de Procesamiento Gráfico (GPU), construcción del Jacobiano, aceleración.

Abstract

In this paper a parallelization strategy of a fully implicit simulator for the numerical solution of the incompressible two-phase flow model in porous media is presented using GPUs (Graphics Processing Units). The mathematical model is based on the mass conservation equations for the water and oil phases. Mathematical formulation of Pressure-Saturation is used to simplify the numerical model. The Finite Volume technique and the Newton-Raphson method are used to discretize and linearize the partial differential equations, respectively. The construction of the Jacobian directly on the GPU is proposed, which reduces the information that needs to be exchanged between the CPU (Central Processing Unit) and the GPU. The simulator uses libraries that already include methods that belong to the Krylov subspace to solve linear equations systems. The results of three benchmark problems by using different grid sizes are compared. The performance of the numerical code developed is also evaluated. Results of the GPU against the CPU indicate that the numerical simulator reached 22x of speed up to build the Jacobian, and 3x of speed up for executing the whole numerical code by using the GPU parallelization.

Key words: Two-phase flow model, Newton-Raphson, Graphics Processing Units (GPU), Jacobian construction, speed up.

V. L. Teja-Juárez*
Posgrado en Ciencias de la Tierra
Universidad Nacional Autónoma de México
Ciudad universitaria
Delegación Coyoacán, 04510
México CDMX, México
*Corresponding author: vleonardo.teja@gmail.com

L. M. de la Cruz
Instituto de Geofísica
Universidad Nacional Autónoma de México
Ciudad universitaria
Delegación Coyoacán, 04510
México CDMX, México

Introduction

Nowadays new techniques called Enhanced Oil Recovery Methods (EOR) are applied to improve the oil recovery in a hydrocarbon reservoir. Lake (1989) gives a definition for the EOR methods: EOR is oil recovery by the injection of materials not normally present in the reservoir. This definition covers all modes of oil recovery and most oil recovery agents. Considering this definition the EOR methods might consider both secondary and tertiary recovery. Before EOR methods are applied there is a technique that almost always has to be considered, that is, the waterflooding technique. Waterflooding technique is the oldest assisted recovery method and it remains as the most common method used to sweep the oil that was not produced by natural pressure, and to keep the oil pressure when this has declined due to reservoir conditions (Latil, 1980).On the other hand, due to the growing need in the oil industry to make faster and more efficient calculations to simulate the recovery conditions before, during and after the production life of a reservoir, it is necessary to test new computational techniques that reduce the run time of the numerical simulators. Several investigations have been carried out to improve the run time of the reservoir simulators (Killough *et al*., 1991; Shiralkar *et al*., 1998; Ma and Chen, 2004; Dogru *et al*., 2009). Most of these papers have been developed using distributed computing. Recently, Wang *et al*. (2015) developed a scalable black oil simulator using ten millions of grid blocks approximately, their simulator reached a scalability factor of 1.03 using 2048 processors. Also Liu *et al*. (2015) developed a three phase parallel simulator applying MPI (Message Passing Interface) for communications between computational nodes and OpenMP for shared memory. They obtained an efficiency of 95.7% by using 3072 processors. However, there is a limitation to use this technique, since a computational cluster with tens until thousands of processors is needed to achieve the desired speed up.

As an alternative NVIDIA has developed a programing language called CUDA (Compute Unified Device Architecture) which can be used to take advantage of the power computing graphics cards for general purpose simulations. Yu *et al*. (2012), used GPUs to parallelize a reservoir simulator which can run large scale problems. They used over one million grid blocks obtaining a good speed up compared to the numerical code of the CPU. Li and Saad (2013), developed a numerical code of preconditioned linear solvers based on GPU, their numerical experiments indicate that Incomplete LU (ILU) factorization preconditioned GMRES method achieved a speed up nearing to 4 compared versus CPU numerical code. Liu *et al*. (2013), reported improved preconditioners and algebraic multigrid linear solvers applied to reservoir simulations using GPUs. De la Cruz and Monsivais (2014) developed a two phase porous media flow simulator to compare the performance of a single GPU with a single node of a cluster using distributed memory. These authors found that a single GPU is better than a computational node with twelve processors. Trapeznikova *et al*. (2014) developed a software library for numerical simulation of multiphase porous media flows that is applied to GPU-CPU hybrid supercomputers. The model is implemented by an original algorithm of the explicit type. An explicit three-level approximation of the modified continuity equation is used. After that the Newton method is used locally at each point of the computational grid. Authors used SPE-10 project as benchmark, they achieved a 97x of speed up when they compare the run time obtained by a single GPU versus one CPU, and 18x of speed up when a computational node of six processors is used. Mukundakrishnan *et al*. (2015), presented the implementation in GPUs of a black oil simulator, which uses a fully implicit scheme for the discretization in the time and the constrained pressure residual -algebraic multigrid (CPR-AMG) to solve the linear system equations. They reported an average of 20 minutes for the run time to solve a problem with 16 million of active blocks by using 4 GPUs. Anciaux-Sedrakian *et al*. (2015) made a numerical study of different preconditioners such as: Polynomial, ILU and CPR-AMG which were implemented in a heterogeneous architecture (CPU-GPU). They emphasize two key points to obtain high performance in heterogeneous architectures; the first is to maximize the utilization and occupancy of the GPU and the second refers to minimize the high cost of transferring GPU data to the node with the CPUs and vice versa. Their results show that a combination of 1 processor plus 1 GPU is approximately 2 times faster compared versus an 8-processor node by applying CPR-AMG preconditioner.

In this work a simulator for oil recovery was developed based in the water injection process and the simultaneous solution technique described by Chen *et al*. (2006). A parallelization scheme is proposed by using GPUs for both the construction of the Jacobian matrix and the solution of the linear system of equations.

The paper is organized in this way: In Section 2, the mathematical equations of the water injection and pressure-saturation formulation model are introduced. In Section 3, the numerical discretization is presented by using the Finite Volume Method (FVM) and the linearization of the equations by applying the Newton-Rapshon method (NR). In Section 4, the computational implementation of the CPU and GPU are shown and main algorithms are explained. In Section 5, numerical results of three benchmark problems are presented. Also in this section, the performance of the parallel numerical code is evaluated by comparing the run time obtained in both GPU and CPU.

Mathematical model of the incompressible two-phase flow in porous media

The mathematical model of the incompressible two-phase flow can be used to simulate the water injection into a hydrocarbon reservoir. The mass balances are obtained by taking into account two phases: oil and water. Governing equations can be obtained by applying an axiomatic formulation (see Herrera and Pinder, 2012 for a complete description on this formulation). A general local balance mass equation can be written as follows:

$$\frac{\partial\left(\phi\rho_\alpha S_\alpha\right)}{\partial t}+\nabla\cdot\left(\overrightarrow{u_\alpha}\rho_\alpha\right)=q_\alpha \tag{1}$$

Here ϕ is the porosity of the media ρ_α, S_α, u_α, and q_α represent the density, saturation, velocity and source of phase α. The Darcy's velocity is used expressed as follows:

$$\vec{u}_\alpha=-\frac{\overset{=}{k}k_{r\alpha}}{\mu_\alpha}\nabla\Phi_\alpha \tag{2}$$

where $\overset{=}{k}$ is the diagonal tensor of absolute permeability and $k_{r\alpha}$ is the relative permeability of phase α; the Greek letters Φ_α and μ_α are the potential and the dynamic viscosity for phase α, respectively. Now, substituting (2) into (1) and replacing α by o and w, the next two coupled mass balance equations were obtained (Chen *et al*., 2006):

$$\frac{\partial\phi\rho_w S_w}{\partial t}=\nabla\cdot\left(\frac{\overset{=}{k}k_{rw}\rho_w}{\mu_w}\nabla\Phi_w\right)+q_w \tag{3}$$

$$\frac{\partial\phi\rho_o S_o}{\partial t}=\nabla\cdot\left(\frac{\overset{=}{k}k_{ro}\rho_o}{\mu_o}\nabla\Phi_o\right)+q_o \tag{4}$$

The mass balance equations are interrelated by the following mathematical expressions:

$$S_o+S_w=1 \tag{5}$$

$$\Phi_\alpha+\rho_\alpha-\rho_w\wp z \tag{6}$$

$$p_w=p_o-p_{cow} \tag{7}$$

$$p_{cow}=p_{cow}\left(S_w\right) \tag{8}$$

where p_α is the pressure of the phase α, $\wp$ is the magnitude of gravity, z is the depth and p_{cow} is the oil-water capillary pressure as a function of S_w.

Equations (3) and (4) are non-linear and strongly coupled. In order to simplify the numerical solution of these equations, the pressure-saturation formulation was used which consists in selecting oil pressure and water saturation as primary variables and in using the fractional flow theory to derive one equation for pressure and one equation for saturation (Peaceman, 1977; Chen *et al*., 2006). The mass balance equation for water phase is:

$$\frac{\partial\left(\phi\rho_w S_w\right)}{\partial t}-\nabla\cdot\left(\rho_w\frac{\overset{=}{k}k_{rw}}{\mu_w}\left(\left(\nabla p_o-\nabla p_{cow}\right)-\rho_w\wp\nabla z\right)\right)=q_w \tag{9}$$

Considering non-compressible flow, equation (9) becomes:

$$\phi\frac{\partial S_w}{\partial t}-\nabla\cdot\left[\overset{=}{k}\lambda_w\cdot\left(\nabla p_o-\frac{dp_{cow}}{dS_w}\nabla S_w-\rho_w\wp\nabla z\right)\right]=\frac{q_w}{\rho_w} \tag{10}$$

where the following substitutions were carried out:

$$\nabla p_{cow}=\frac{dp_{cow}}{dS_w}\nabla S_w \tag{11}$$

$$\lambda_w=\frac{k_{rw}}{\mu_w} \tag{12}$$

Taking into account the fractional flow of the phase α (f_α) that is defined as the quotient of the phase α mobility (λ_α) over the total mobility (λ), $f_\alpha=\frac{\lambda_\alpha}{\lambda}$, a general pressure equation was derived:

$$\frac{\partial\phi}{\partial t}-\nabla\cdot\bar{\bar{k}}\lambda\Big[\sum_{\alpha}f_{\alpha}\nabla p_{\alpha}-\sum_{\alpha}f_{\alpha}\rho_{\alpha}\wp\nabla z\Big]+\sum_{\alpha}\frac{1}{\rho_{\alpha}}\Big[\phi S_{\alpha}\frac{\partial\rho_{\alpha}}{\partial t}+\vec{u}_{\alpha}\nabla\cdot\rho_{\alpha}\Big]-\sum_{\alpha}\frac{q_{\alpha}}{\rho_{\alpha}}=0 \tag{13}$$

For more details about fractional flow formulation readers can consult Chen *et al*., 2006. Considering no change in the porosity, and non-compressible flows, equation (13) can be reduced to:

$$-\nabla\cdot\left[\bar{\bar{k}}\lambda\nabla p_{o}-\bar{\bar{k}}\lambda_{w}\frac{dp_{cow}}{dS_{w}}\nabla S_{w}-\left(\lambda_{o}\rho_{o}+\lambda_{w}\rho_{w}\right)\wp\nabla z\right]=\frac{q_{w}}{\rho_{w}}+\frac{q_{o}}{\rho_{o}} \tag{14}$$

Equations (10) and (14) are coupled and non-linear. The Newton-Raphson approach was used to linearize the equations and solve them using a fully-implicit strategy. In this work three different cases of study are described.

Numerical model

In this section a brief description is given of the use of the Finite Volume Method (FVM) to discretize equations (10) and (14), and the Newton-Raphson method to linearize those equations.

Calculation of residuals by using the Finite Volume Method

As a way to show how FVM is applied to compute the residuals for the governing equations, the saturation equation for the three-dimensional case is discretized. Integrating equation (10) with respect to time and the control volume shown in Figure 1, equation (15) is obtained:

$$\int_{n}^{n+1}\Big\{\int_{\Delta V}\Big[\phi\frac{\partial S_{w}}{\partial t}-\nabla\cdot\left[\bar{\bar{k}}\lambda_{w}\left(\nabla p_{o}-\frac{dp_{cow}}{dS_{w}}\nabla S_{w}-\rho_{w}\wp\nabla z\right)\right]-\frac{q_{w}}{\rho_{w}}\Big]dV\Big\}dt=0 \tag{15}$$

In order to evaluate the terms of equation (15) the following considerations were taken into account: 1) a backward Euler approximation is used, 2) the permeability tensor is diagonal and 3) the space derivatives are approximated using central differences. Therefore, the discretized form of equation (15) in terms of a residual is written as follows:

$$\begin{aligned}
R_{w}\left(p_{o},S_{w}\right)=&\frac{\phi\Delta V}{\Delta t}[(S_{w})-(S_{w})^{n}]_{P}-\left[T_{w,e}\left(p_{o,E}-p_{o,P}\right)-T_{w,w}\left(p_{o,P}-p_{o,W}\right)\right]+\left[T_{w,e}\frac{dp_{cow}}{dS_{w}}\Big|_{e}\left(S_{w,E}-S_{w,P}\right)\right.\\
&\left.-T_{w,w}\frac{dp_{cow}}{dS_{w}}\Big|_{w}\left(S_{w,P}-S_{w,W}\right)\right]+\left[T_{w,e}\wp\rho_{w}\big|_{e}\left(z_{w,E}-z_{w,P}\right)-T_{w,w}\wp\rho_{w}\big|_{w}\left(z_{w,P}-z_{w,W}\right)\right]\\
&-\left[T_{w,n}\left(p_{o,N}-p_{o,P}\right)-T_{w,s}\left(p_{o,P}-p_{o,S}\right)\right]+\left[T_{w,n}\frac{dp_{cow}}{dS_{w}}\Big|_{n}\left(S_{w,N}-S_{w,P}\right)\right.\\
&\left.-T_{w,s}\frac{dp_{cow}}{dS_{w}}\Big|_{s}\left(S_{w,P}-S_{w,S}\right)\right]+\left[T_{w,n}\wp\rho_{w}\big|_{n}\left(z_{w,N}-z_{w,P}\right)-T_{w,s}\wp\rho_{w}\big|_{s}\left(z_{w,P}-z_{w,S}\right)\right]\\
&-\left[T_{w,t}\left(p_{o,T}-p_{o,P}\right)-T_{w,b}\left(p_{o,P}-p_{o,B}\right)\right]+\left[T_{w,t}\frac{dp_{cow}}{dS_{w}}\Big|_{t}\left(S_{w,T}-S_{w,P}\right)\right.\\
&\left.-T_{w,b}\frac{dp_{cow}}{dS_{w}}\Big|_{b}\left(S_{w,P}-S_{w,B}\right)\right]+\left[T_{w,t}\gamma_{w}\big|_{t}\left(z_{w,T}-z_{w,P}\right)-T_{w,b}\gamma_{w}\big|_{b}\left(z_{w,P}-z_{w,B}\right)\right]-\frac{q_{w,P}}{\rho_{w}}\Delta V
\end{aligned} \tag{16}$$

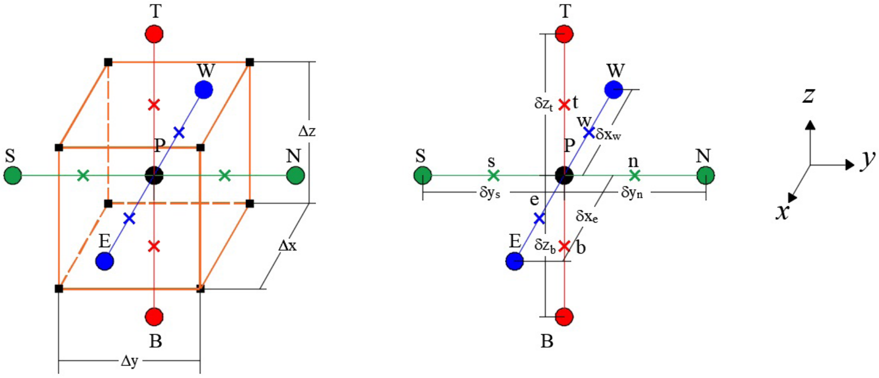

Figure 1. Three-dimensional stencil to apply the FVM. $\Delta V=\Delta x\Delta y\Delta z$ is defined.

where the transmissibility is computed as $T_w = \frac{k_{ii}\lambda_w A_i}{\delta x_i}$ for *i=1, 2, 3*; the specific weight is defined as $\gamma_w = \rho_w \wp$, A_i is the face area of volume perpendicular to the axis *i*, for example, $A_1 = \Delta y \Delta z$, and δx_i represents the distance between neighboring volumes centers. Similarly the residual R_o for the pressure equation (14), is expressed as follows:

$$
\begin{aligned}
R_o\left(p_o,S_w\right) = {} & \left[T_e\left(p_{o,E}-p_{o,P}\right)-T_w\left(p_{o,P}-p_{o,W}\right)\right]-\left[T_{w,e}\frac{dp_{cow}}{dS_w}\Big|_e\left(S_{w,E}-S_{w,P}\right)-T_{w,w}\frac{dp_{cow}}{dS_w}\Big|_w\left(S_{w,P}-S_{w,W}\right)\right] \\
& -\left[\frac{k_{xx}(\lambda_w\gamma_w+\lambda_o\gamma_o)A_1}{\delta x}\Big|_e\left(z_{w,E}-z_{w,P}\right)-\frac{k_{xx}(\lambda_w\gamma_w+\lambda_o\gamma_o)A_1}{\delta x}\Big|_w\left(z_{w,P}-z_{w,W}\right)\right] \\
& +\left[T_{w,n}\left(p_{o,N}-p_{o,P}\right)-T_{w,s}\left(p_{o,P}-p_{o,S}\right)\right]-\left[T_{w,n}\frac{dp_{cow}}{dS_w}\Big|_n\left(S_{w,N}-S_{w,P}\right)-T_{w,s}\frac{dp_{cow}}{dS_w}\Big|_s\left(S_{w,P}-S_{w,S}\right)\right] \\
& -\left[\frac{k_{yy}(\lambda_w\gamma_w+\lambda_o\gamma_o)A_2}{\delta y}\Big|_n\left(z_{w,N}-z_{w,P}\right)-\frac{k_{yy}(\lambda_w\gamma_w+\lambda_o\gamma_o)A_2}{\delta y}\Big|_s\left(z_{w,P}-z_{w,S}\right)\right] \\
& +\left[T_{w,t}\left(p_{o,T}-p_{o,P}\right)-T_{w,b}\left(p_{o,P}-p_{o,B}\right)\right]-\left[T_{w,t}\frac{dp_{cow}}{dS_w}\Big|_t\left(S_{w,T}-S_{w,P}\right)-T_{w,b}\frac{dp_{cow}}{dS_w}\Big|_b\left(S_{w,P}-S_{w,B}\right)\right] \\
& -\left[\frac{k_{zz}(\lambda_w\gamma_w+\lambda_o\gamma_o)A_3}{\delta z}\Big|_t\left(z_{w,T}-z_{w,P}\right)-\frac{k_{zz}(\lambda_w\gamma_w+\lambda_o\gamma_o)A_3}{\delta z}\Big|_b\left(z_{w,P}-z_{w,B}\right)\right]+\left[\frac{q_w}{\rho_w}+\frac{q_o}{\rho_o}\right]\Delta V
\end{aligned}
\tag{17}
$$

Here T_i, implies the calculation of the transmissibility considering the total mobility λ and $T_{w,i}$ refers to the transmissibility considering the mobility of the water phase λ_w. In equations (16) and (17) the superscript $n + 1$ is omitted for simplicity.

Newton-Rapshon Method

Because there are nonlinearities in the discretized equations, the Newton-Raphson method was selected to linearize and to solve these equations. The main advantage of the method is its numerical stability compared with methods which use explicit discretization (Abou-Kassem *et al*., 2006; Chen, 2007). For applying the Newton-Raphson method p_o^{n+1} and S_w^{n+1} were selected as primary variables. Thus, the system of equations to solve has the following form

$$
\begin{pmatrix}
\frac{\partial R_o}{\partial p_o}\Big|^k & \frac{\partial R_o}{\partial S_w}\Big|^k \\
\frac{\partial R_w}{\partial p_o}\Big|^k & \frac{\partial R_w}{\partial S_w}\Big|^k
\end{pmatrix}
\begin{pmatrix}
\delta p_o^{k+1} \\
\delta S_w^{k+1}
\end{pmatrix}
=
\begin{pmatrix}
-R_o^k \\
-R_w^k
\end{pmatrix}
\tag{18}
$$

Matrix on the left of equation (18) is the Jacobian and superscript k is used to indicate the Newtonian iteration. The system written in extended form gives:

$$
\begin{aligned}
& \frac{\partial R_o\left(p_o,S_w\right)}{\partial P_{o,B}}\Big|^k \delta p_{o,T}^{k+1}+\frac{\partial R_o\left(p_o,S_w\right)}{\partial P_{o,S}}\Big|^k \delta p_{o,S}^{k+1}+\frac{\partial R_o\left(p_o,S_w\right)}{\partial p_{o,W}}\Big|^k \delta p_{o,W}^{k+1}+\frac{\partial R_o\left(p_o,S_w\right)}{\partial p_{o,P}}\Big|^k \delta p_{o,P}^{k+1}+ \\
& \frac{\partial R_o\left(p_o,S_w\right)}{\partial p_{o,E}}\Big|^k \delta p_{o,E}^{k+1}+\frac{\partial R_o\left(p_o,S_w\right)}{\partial p_{o,N}}\Big|^k \delta p_{o,N}^{k+1}+\frac{\partial R_o\left(p_o,S_w\right)}{\partial p_{o,T}}\Big|^k \delta p_{o,T}^{k+1}+ \\
& \frac{\partial R_o\left(p_o,S_w\right)}{\partial S_{w,B}}\Big|^k \delta S_{w,T}^{k+1}+\frac{\partial R_o\left(p_o,S_w\right)}{\partial S_{w,S}}\Big|^k \delta S_{w,S}^{k+1}+\frac{\partial R_o\left(p_o,S_w\right)}{\partial S_{w,W}}\Big|^k \delta S_{w,W}^{k+1}+\frac{\partial R_o\left(p_o,S_w\right)}{\partial S_{w,P}}\Big|^k \delta S_{w,P}^{k+1}+ \\
& \frac{\partial R_o\left(p_o,S_w\right)}{\partial S_{w,E}}\Big|^k \delta S_{w,E}^{k+1}+\frac{\partial R_o\left(p_o,S_w\right)}{\partial S_{w,N}}\Big|^k \delta S_{w,N}^{k+1}+\frac{\partial R_o\left(p_o,S_w\right)}{\partial S_{w,T}}\Big|^k \delta S_{w,T}^{k+1}=-R_o^k
\end{aligned}
\tag{19}
$$

$$\left.\frac{\partial R_w\left(p_o,S_w\right)}{\partial P_{o,B}}\right|^k \delta p^{k+1}_{o,T} + \left.\frac{\partial R_w\left(p_o,S_w\right)}{\partial P_{o,S}}\right|^k \delta p^{k+1}_{o,S} + \left.\frac{\partial R_w\left(p_o,S_w\right)}{\partial p_{o,W}}\right|^k \delta p^{k+1}_{o,W} + \left.\frac{\partial R_w\left(p_o,S_w\right)}{\partial p_{o,P}}\right|^k \delta p^{k+1}_{o,P} +$$

$$\left.\frac{\partial R_w\left(p_o,S_w\right)}{\partial p_{o,E}}\right|^k \delta p^{k+1}_{o,E} + \left.\frac{\partial R_w\left(p_o,S_w\right)}{\partial p_{o,N}}\right|^k \delta p^{k+1}_{o,N} + \left.\frac{\partial R_w\left(p_o,S_w\right)}{\partial p_{o,T}}\right|^k \delta p^{k+1}_{o,T} +$$

$$\left.\frac{\partial R_w\left(p_o,S_w\right)}{\partial S_{w,B}}\right|^k \delta S^{k+1}_{w,T} + \left.\frac{\partial R_w\left(p_o,S_w\right)}{\partial S_{w,S}}\right|^k \delta S^{k+1}_{w,S} + \left.\frac{\partial R_w\left(p_o,S_w\right)}{\partial S_{w,W}}\right|^k \delta S^{k+1}_{w,W} + \left.\frac{\partial R_w\left(p_o,S_w\right)}{\partial S_{w,P}}\right|^k \delta S^{k+1}_{w,P} +$$

$$\left.\frac{\partial R_w\left(p_o,S_w\right)}{\partial S_{w,E}}\right|^k \delta S^{k+1}_{w,E} + \left.\frac{\partial R_w\left(p_o,S_w\right)}{\partial S_{w,N}}\right|^k \delta S^{k+1}_{w,N} + \left.\frac{\partial R_w\left(p_o,S_w\right)}{\partial S_{w,T}}\right|^k \delta S^{k+1}_{w,T} = -R^k_w \tag{20}$$

Equations (19), (20) along with the residuals (16) and (17) are used to build the linear system as shown in Figure 2, where the subscript m refers to the total number of discrete volumes.

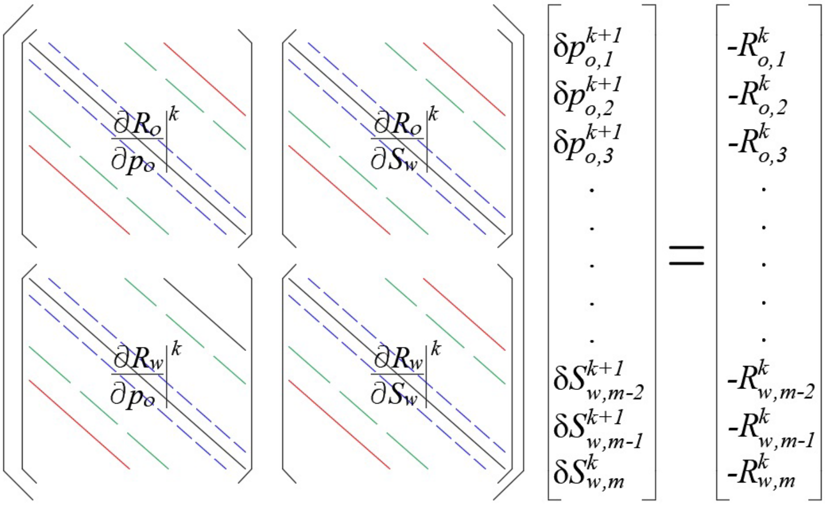

Figure 2. Linear system equations for the primary variables p_o and S_w.

One of the main issues in this kind of problems is how to calculate the Jacobian elements and how to solve the resulting linear system. Both tasks are time consuming, therefore new techniques are needed to reduce the time used in doing these computational processes. In the next section details of the computational implementation that makes use of graphical processing units (GPUs) are presented in order to parallelize the construction of the Jacobian and the solution of the resulting linear system

Computational implementation

In this section, the computational methodology used is briefly described to implement the algorithms provided by the numerical methods outlined in previous sections.

CPU Implementation

First of all, the algorithms to be executed in an ordinary CPU were implemented for comparison purposes. The codes were written using the C++ language and the EIGEN library (Jacob and Guennebaud, 2016), the last one was used to simplify the array and matrices management and the solution of the linear systems of equations. The pseudocode of the main algorithm is shown in Figure 3.

In the first three lines of the pseudocode shown in Figure 3, all required variables and arrays are declared and initialized with adequate values, this includes the initial and boundary conditions, petrophysical values, size of the mesh, time step, etc. In line 4 the simulation

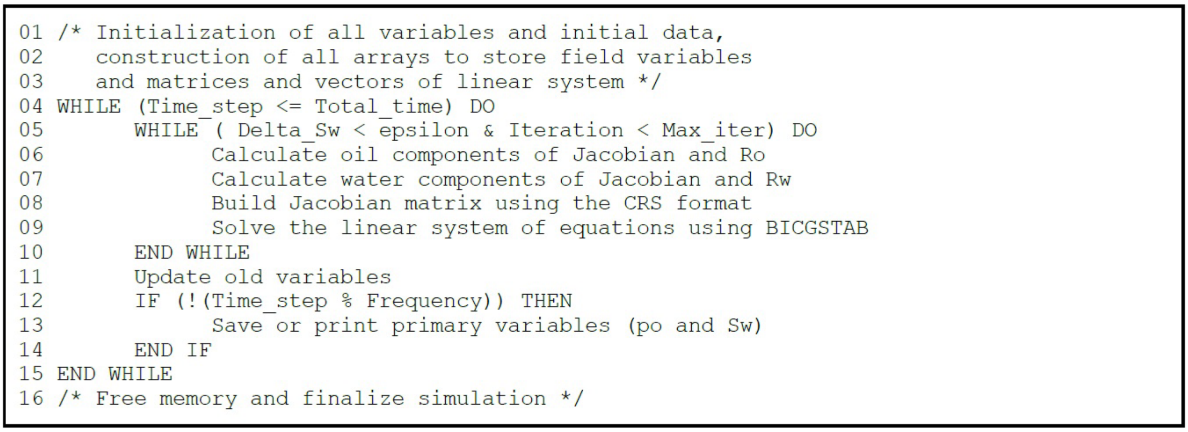

```
01 /* Initialization of all variables and initial data,
02    construction of all arrays to store field variables
03    and matrices and vectors of linear system */
04 WHILE (Time_step <= Total_time) DO
05       WHILE ( Delta_Sw < epsilon & Iteration < Max_iter) DO
06             Calculate oil components of Jacobian and Ro
07             Calculate water components of Jacobian and Rw
08             Build Jacobian matrix using the CRS format
09             Solve the linear system of equations using BICGSTAB
10       END WHILE
11       Update old variables
12       IF (!(Time_step % Frequency)) THEN
13             Save or print primary variables (po and Sw)
14       END IF
15 END WHILE
16 /* Free memory and finalize simulation */
```

Figure 3. Pseudocode of the main algorithm.

initiates and is carried out until the total number of time steps is reached. Inside this first cycle, another one implements the Newton-Raphson (NR) algorithm. This internal cycle starts in line 5 and is carried out until the norm of the change of the water saturation ($|\delta S_w|$) is less than a prescribed value (ε) or the prescribed maximum number of iterations of the NR algorithm is reached. Lines 6 to 9 represent the main steps to solve the problem and use the highest percentage of CPU time. In lines 6 and 7 every entry of the Jacobian matrix is calculated, this means to calculate the discretized components of the residuals, equations (18) and (19), and their corresponding derivatives. It is worth mentioning that all derivatives are done numerically and first order forward finite differences are used to do so. Then in step 9 the Jacobian matrix is build using the Compressed Row Storage (CRS) format in order to take advantage of the sparseness of the matrix and to save memory. In the calculations, these three steps take around 8% of the total time. In line 9 the linear system is solved using the Biconjugate Gradient Stabilized (BICGSTAB) method algorithm which is contained in the EIGEN library. This step takes around 75% of the total CPU time. Once the NR algorithm has converged, all the required variables were updated to be used in the next time step, line 11. Finally, the solution (primary variables) were saved or printed every time the *Iteration* variable is divisible by a prescribed *Frequency*. This frequency will become important in the GPU implementation.

GPU Implementation

The implementation in CPU presented in the previous section is standard and do not have any complications. For the GPU implementation the Compute Unified Device Architecture (NVIDIA, 2012) and the CUSP Library were used, which provides a high-level interface for manipulating sparse matrices and solving sparse linear systems (Maia and Dalton, 2016). The present implementation is almost done totally in GPU, which means that the amount of information exchange between CPU and GPU is relatively low. In this sense, the pseudocode of the main algorithm for GPU implementation is similar to the one shown in Figure 3. The following differences have to be mentioned: a) the cycle starting in line 4 require all the variables and arrays defined in lines 1-3, therefore a first exchange of information is done from CPU to GPU, however this is minimal due to the fact that the biggest arrays are constructed directly in the GPU; b) the operations in lines 6, 7, 8, 9 and 11 are all coded in CUDA, therefore, several kernel functions occur that are executed in the GPU device; c) the operation in line 13 requires a movement of information from GPU to CPU, however this is done only every time the *Iteration* is divisible by the *Frequency* and this can be just one time, for example when the simulation is finished, or when the user requires the information of the final solution.

The kernel functions are executed in parallel by threads. These threads are defined by global indexes that belong to a grid of blocks. The grid and block sizes are defined by the user. The grid can be defined for 1, 2 or 3 dimensions. Each block has a finite number of threads, usually up to 1024 thread count. The maximum grid size is given by the manufacturing specifications of each graphics card. All this features of modern GPUs can be consulted elsewhere in NVIDIA CUDA web site. Taking all this into account, it is only possible to efficiently parallelize numerical codes that do not exceed the number of threads that can be executed in the grid of blocks. On the other hand, it is easy to parallelize functions that execute the same operations over the entries of arrays, since only the threads indexes have to be defined and this definition replaces each loop. As an example of this method, Figures 4 and 5 show an extract of the codes for calculating the Jacobian block corresponding to the residual R_o and its derivatives ($\partial R_o / \partial p_o$), in CPU and GPU respectively.

In the function jacobianCoeff_RoPo3D() all the coefficients of Jacobian block $\partial R_o / \partial p_o$ were calculated. The code is standard and is based in tridimensional arrays which contain some variables related to the Cartesian mesh for the numerical simulation. Therefore, three nested cycles occur, one cycle for each axis. In the most internal cycle, several functions are executed to carry out several numerical methods, among them: interpolations for initial relative permeability and saturations from centers of volumes to its faces (lines 5 and 6), calculation of relative permeability using data from tables (line 7), calculations of coefficients of the residual and its derivatives (lines 9 and 10), and the assembling of the corresponding block (line 11).

In the same way as in the Figure 4, in Figure 5 an extract of code of the kernel function is shown that implements the calculation of the Jacobian block $\partial R_o / \partial p_o$. The kernel function jacobianCoeff_RoPo3D() is executed in the GPU. The first thing to do is to determine the thread index, see lines 2-4. Using this index it is possible that each thread of the block in the grid, execute the operations defined in lines 5-12 concurrently. Line 5 is required to assure that the index is inside the limits of the arrays. Lines 6 to 12 consist of kernel functions, similar to the functions defined in CPU, see Figure 4, but using the index to perform each one of the numerical methods needed to calculate the corresponding block of the Jacobian matrix. These kernels are device functions that can only be executed by another kernel and are able to use the GPU memory (Sanders, 2010; NVIDIA, 2012). Two kind of memories were used: global memory to store the primary variables (S_w and p_o), the properties of the porous media (k, ϕ, etc) and some other important arrays of the simulation; constant memory is used to store constant values, i.e, the viscosities, conversion factors and some tables of properties (relative permeability). Figure 6 shows schematically how the variables are stored within the GPU memory.

```
01 void jacobianCoeff_RoPo3D (*physical parameters as arguments) {
02   for (i=1; i<nx-1; i++){
03     for (j=1; j<ny-1; j++){
04       for (k=1; k<nz-1; k++){
05         interpolatePermeability(k, k_e, k_w, k_n, k_s, k_t, k_b);
06         interpolateSaturation(Sw, Sw_e, Sw_w, Sw_n, Sw_s, Sw_t, Sw_b);
07         calculate_kro(Sw, kro(Sw),kro_e, kro_w, kro_n, kro_s, kro_t, kro_b);
08 /* ... Some other calculations  ... */
09         F(Po)=Tr_e*(Po);
10         F(Po+deltaPo)=Tr_e*(Po+deltaPo);
11         Block_RoPo3D[3D(i,j,k)]=firstOrderDerivative(F(Po), F(Po+deltaPo), deltaPo);
12       }
13     }
14   }
15 }
```

Figure 4. Function to calculate the Jacobian block.

```
01 __global__ void jacobianCoeff_RoPo3D (*physical parameters as arguments) {
02   int i = threadIdx.x + blockIdx.x*blockDim.x;
03   int j = threadIdx.y + blockIdx.y*blockDim.y;
04   int k = threadIdx.z + blockIdx.z*blockDim.z;
05   if(i>0 && i < nx-1 && j > 0 && j < ny-1 && k > 0 && k < nz-1){
06     interpolatePermeability(k, k_e, k_w, k_n, k_s, k_t, k_b);
07     interpolateSaturation(Sw, Sw_e, Sw_w, Sw_n, Sw_s, Sw_t, Sw_b);
08     calculate_kro(Sw, kro(Sw),kro_e, kro_w, kro_n, kro_s, kro_t, kro_b);
09 /* ... Some other calculations  ... */
10     F(Po)=Tr_e*(Po);
11     F(Po+deltaPo)=Tr_e*(Po+deltaPo);
12     Block_RoPo3D[3D(i,j,k)]=firstOrderDerivative(F(Po), F(Po+deltaPo), deltaPo);
13   }
14 }
```

Figure 5. Kernel function to calculate the Jacobian block.

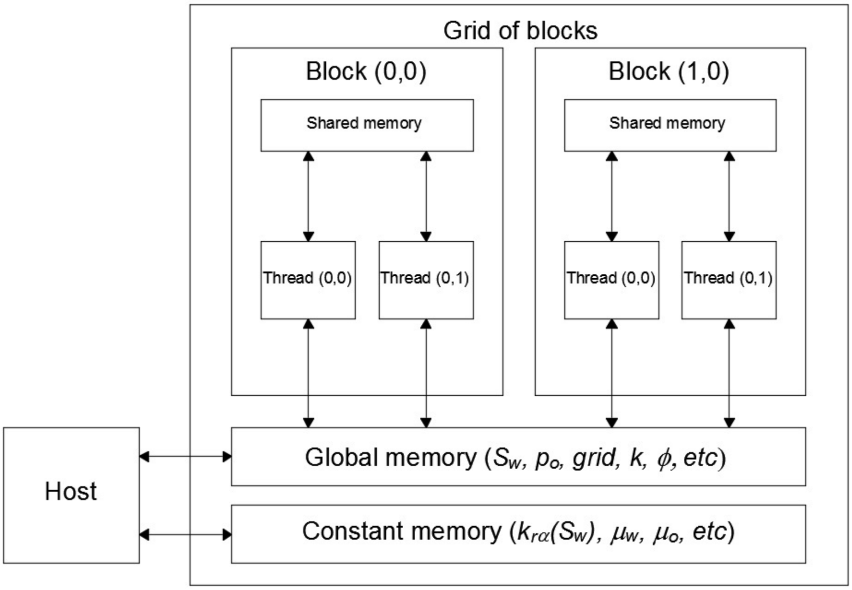

Figure 6. GPU memory used to store variables to build the Jacobian.

Finally, once the Jacobian components has been built, the linear system of equations is constructed in CRS format. This extra step is needed in order to use the algorithms of the EIGEN and CUSP libraries. Both libraries require a matrix in the CRS format and a right hand side (rhs) vector. The result is stored in another vector that contains the solution of the linear system.

Numerical results

As a way to validate the numerical code, in this section numerical results obtained for three different cases are presented. Also numerical performance experiments were carried out to test computationally the parallel numerical code that is compared versus serial code.

Buckley Leverett

The Buckley-Leverett model describes the displacement of oil by water in an horizontal domain. This mathematical model is widely used in the validation of two phase fluid flow simulators, because it has an analytic solution for the water saturation profile. The hypothesis of the Buckley-Leverett model are:

a) The displacement occurs at a one-dimensional medium.
b) The porous media is isotropic.
c) No effects of capillary pressure nor gravity forces are considered.
d) There are no sources nor sinks.
e) Water gets injected to a constant flow through the left boundary of the domain. Oil is produced on the right boundary at a constant pressure.

The parameters to carry out the simulation are shown in Table 1. Relative permeabilities $k_{ra}(S_w)$ can be obtained from Chen *et al*. (2006).

In this paper a comparison of the analytical solution versus the solution obtained numerically is presented. The numerical parameters were selected as follows: to evaluate the derivatives within the Jacobian blocks increments of $\Delta S_w = 1x10^{-05}$ for water saturation and $\Delta p_o = 0.1$ for the oil pressure were used. Stop criterion for leaving the Newton-Rapshon loop was selected to: $|\delta S_w| < 1x10^{-05}$ and a fixed time step of 1 day

Table 1. Parameters to solve the Buckley-Leverett problem.

Property	**Value**
Length of domain (L_x)	1,000 (ft)
Absolute permeability (k)	100.0 (mD)
Porosity (ϕ)	0.20
Water viscosity (μ_w)	0.42 (cP)
Oil viscosity (μ_o)	15.5 (cP)
Residual water saturation (S_{wr})	0.40
Residual oil saturation (S_{or})	0.18
Injection velocity (v_{inj})	2.0E-06 (ft/s)
Production pressure (p_{out})	1,000 (psi)

was chosen. The number of discrete volumes selected to study its effect in the solution were: 100, 500, 1,000, 5,000 and 10,000. The total time simulation was of 120 days and results are saved every 30 days. Table 2 shows a comparison between analytical and numerical solutions at some selected positions. As shown in this table as the number of volumes increases the relative error and the root mean square deviation (RMSD) respect to the analytical solution decreases.

Figure 7 shows the water saturation and pressure profiles obtained for 120 days of total simulation by using 10,000 discrete volumes. Results of the water saturation profile are congruent with the analytical solution (dashed line). This result indicates that the problem has been solved correctly.

Table 2. Numerical results obtained for the Buckley-Leverett problem.

Number of discrete volumes	Position x (ft)	Simulation time (days)	Sw Numerical	Sw Analytical domain	Error %	RMSD At the whole
100	145	30	0.4721	0.4	18.033	0.01510
	275	60	0.4792	0.4	19.809	0.01590
	405	90	0.4801	0.4	20.037	0.01598
	535	120	0.4786	0.4	19.666	0.01875
500	145	30	0.42238	0.4	5.5942	0.01127
	275	60	0.42049	0.4	5.1216	0.01095
	405	90	0.40972	0.4	2.4295	0.01104
	535	120	0.40849	0.4	2.1213	0.01093
1,000	145	30	0.40784	0.4	1.9593	0.00987
	275	60	0.40399	0.4	0.99737	0.01027
	405	90	0.40080	0.4	0.19905	0.00981
	535	120	0.40056	0.4	0.13941	0.00962
5,000	145	30	0.40028	0.4	0.07096	0.00944
	275	60	0.39998	0.4	0.00525	0.00942
	405	90	0.39999	0.4	0.00170	0.00897
	535	120	0.40001	0.4	0.00150	0.00839
10,000	145	30	0.400130	0.4	0.03159	0.00916
	275	60	0.400020	0.4	0.00568	0.00917
	405	90	0.400001	0.4	0.00093	0.00881
	535	120	0.400001	0.4	0.00091	0.00827

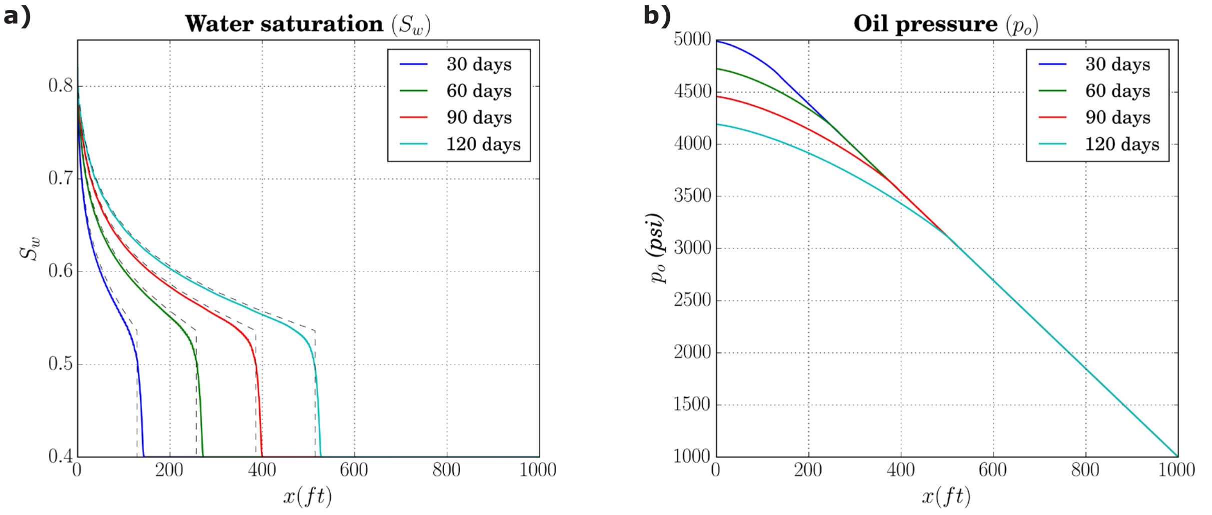

Figure 7. Results for 10,000 discrete volumes: a) Water saturation profile S_w, analytical solution (dashed line) versus numerical solution (continuous line); b) Oil pressure profile p_o.

Five Spot

The model known as "Five Spot" describes the displacement of oil by water in an isotropic domain, in which a producer well and an injector well are placed in the opposite corners of the domain (See Figure 8). In the Five Spot conceptual model the follow assumptions are considered:

a) The displacement occurs at a bidimensional domain.
b) The porous media is isotropic.
c) The effects of capillary pressure are considered.
d) There are one source (injector well) and one sink (producer well).
e) Gravity forces are neglected.

The parameters to carry out the simulation are shown in Table 3. Relative permeabilities k_{ra} (S_w) and capillary pressure p_{cow} can be obtained from Chen *et al*. (2006).

Table 3. Parameters to solve the Five Spot problem (Chen *et al*., 2006).

Property	**Value**
Size of domain (L_x x L_y)	1,000 x1,000 (ft)
Absolute permeability (k)	100.0 (mD)
Porosity (ϕ)	0.20
Water viscosity (μ_w)	0.096 (cP)
Oil viscosity (μ_o)	1.14 (cP)
Residual water saturation (S_{wr})	0.22
Residual oil saturation (S_{or})	0.20
Injection pressure (p_{wb}^{in})	3,700 (psi)
Production pressure (p_{wb}^{out})	3,500 (psi)

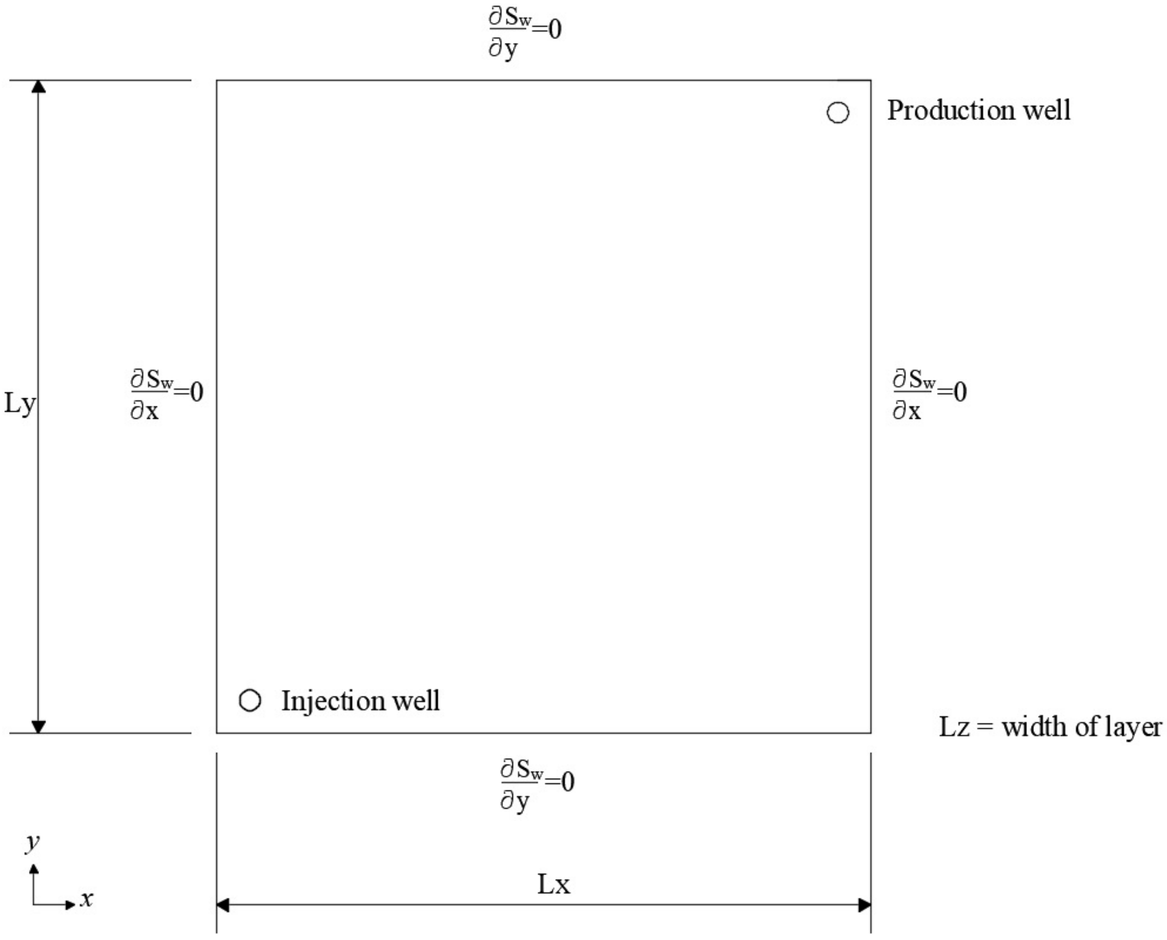

Figure 8. Five Spot physical model.

For this problem the total time simulation was selected to 8,000 days and the results are reported every 500 days. Numerical parameters are the same to those in the Buckley-Leverett problem. Because there is no analytical solution for this problem, it is validated with the results reported by Chen *et al*. (2006). Figure 9 a) shows the production of water and oil in reservoir barrels per day (RB/day) throughout the simulation time. In this figure it can be seen that the results reported by Chen *et al*. (2006) and those obtained in this work have a similar qualitatively behavior. The difference between curves may be due to the numerical techniques used, since Chen *et al*. (2006) used an adaptive time step with an IMPES scheme. The RMSD obtained for the production curves are 43.88 and 137.94 for oil and water production, respectively. In Figure 9 b) fractional flow (F_w) curves are compared. It can be appreciated that the water cut happens after 1,000 days of simulation, which is almost the same result reported by Chen *et al*. (2006).

To verify the solution shape two more simulations were carried out, one considering 30x30 mesh size of and another using 90x90 volumes. Values obtained for RMSD using 30x30 volumes were 41.97 and 135.44; while by using 90x90 volumes were 41.02 and 134.82, for oil and water production respectively.

Figure 10 shows the water saturation profiles at different simulation times in the whole numerical domain. This figure is presented in order to clarify how the waterfront sweeps the oil from the porous medium.

The seventh SPE project

The seventh SPE project is a benchmark that describes the water injection and oil production using horizontal wells, this problem was adapted by Nghiem *et al*. (1991) and Chen *et al*. (2006) for two-phase fluid flow. In the ´resent case capillary pressure and gravity forces were considered. Therefore equations (10) and (14) are used without any modification.

To solve this problem the SPE proposes a mesh of 10x10x7 (Figure 11). This mesh is refined to the y axis center, in order to place the injection and production wells. The length of the blocks in the x axis are uniform and equal to 300 ft ($\delta x = 300\,ft$). For the length of the blocks in the y axis, the distribution is as follows: $\delta y_1 = \delta y_9 = 620\,ft$, $\delta y_2 = \delta y_8 = 400\,ft$, $\delta y_3 = \delta y_7 = 200\,ft$, $\delta y_4 = \delta y_6 = 100\,ft$ and $\delta y_5 = 60\,ft$. For the z axis $\delta z_k = 20\,ft$ for $k_{1,2,3,4}$, $\delta z_5 = 30\,ft$ and $\delta z_k = 50\,ft$ were used. Injection well is placed in the layer δz_6, at the center of the axis y and it crosses all the blocks in the x axis. Production well is placed in the layer δz_1, at the center of the axis y and it crosses only the blocks $\delta x_{6,7,8}$ in the x axis. Parameters to execute the simulation are shown in Table 4. Relative permeabilities $k_{ra}(S_w)$, capillary pressure $p_{cow}(S_w)$, and initial conditions can be obtained from Nghiem *et al*. (1991).

For this problem the total simulation time was selected to be 1,500 days and results are reported every 100 days. Results are validated by comparing production curves reported by Chen *et al*. (2006). Figure 12 a) shows the oil production in stock tank barrels per day (STB/day) during the entire simulation time. It can be noted that the results are qualitatively similar to those reported by Chen *et al*. (2006), although the curve reported by them declines slightly faster. The accumulated oil production curves are also compared, these results are shown in Figure 12 b).

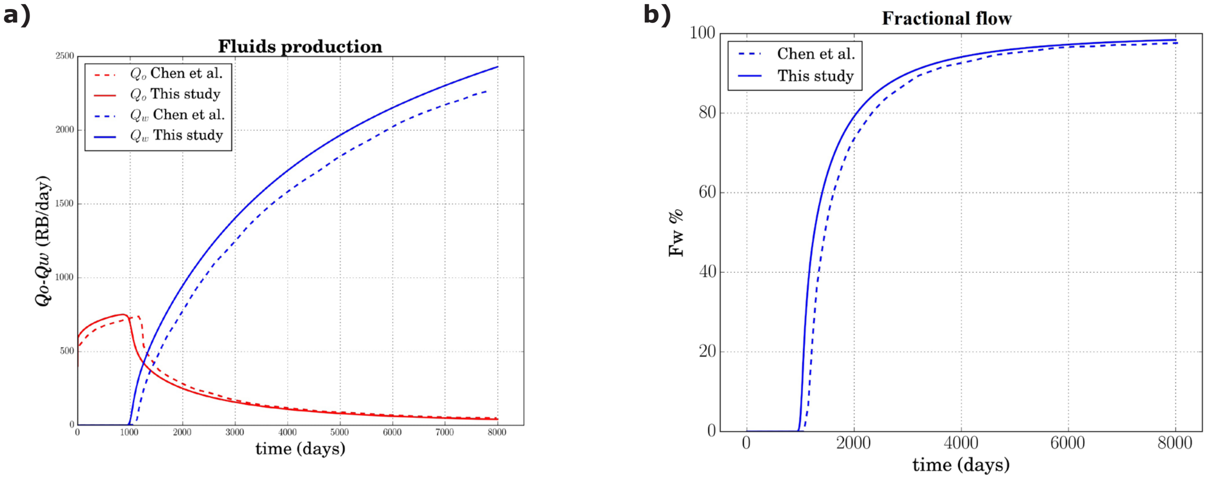

Figure 9. Results obtained using 10x10 discrete volumes: a) water and oil productions Qw-Qo in reservoir barrels per day (RB/day); b) fractional flow Fw (%).

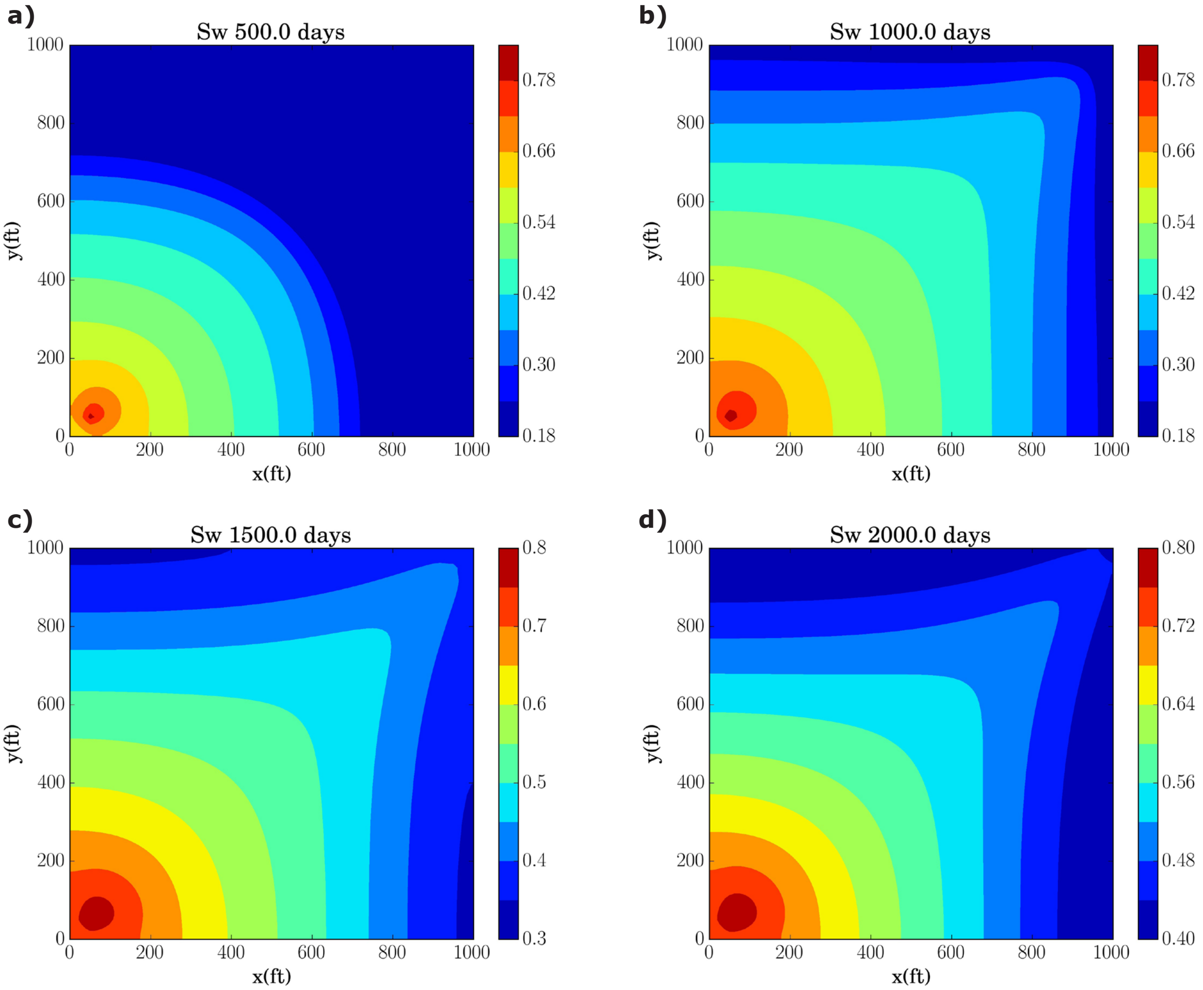

Figure 10. Water saturation profiles for different simulation times using a 90x90 volume.

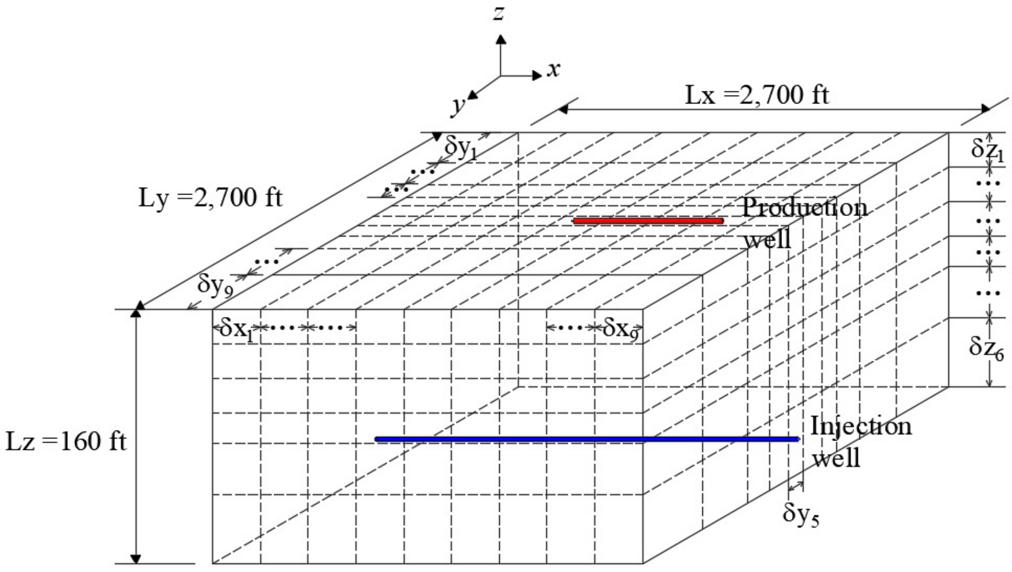

Figure 11. Seventh SPE project physical model.

Table 4. Parameters to solve the Seventh SPE project (Nghiem *et al*., 1991).

Property	Value
Size of domain (L_x x L_y x L_z)	2,700 x 2,700 x160 (ft)
Absolute permeability (k_x, k_y, k_z)	(300.0, 300.0, 30.0) (mD)
Porosity (ϕ)	0.20
Water viscosity (μ_w)	0.96 (cP)
Oil viscosity (μ_o)	0.954 (cP)
Residual water saturation (S_{wr})	0.22
Residual oil saturation (S_{or})	0.0
Injection pressure (p^{in}_{wb})	3,651.4 (psi)
Production pressure (p^{out}_{wb})	3,513.6 (psi)

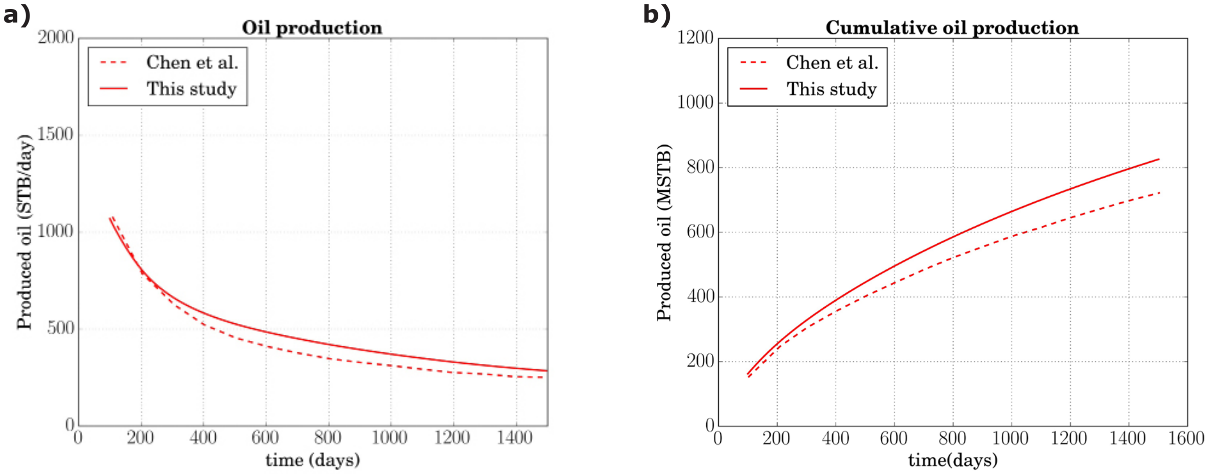

Figure 12. Results obtained using 10X10X7 discrete volumes: a) Oil production (STB/day); b) Cumulative oil production (MSTB).

The small difference observed in Figures 12, may be due to implementations of the numerical method and conversion factor used for the STB; in the present work the STB conversion factor from Nghiem *et al*. (1991) was used. It should be noted that this problem was solved only with the grid size proposed by Nghiem *et al*. (1991), as it is indicated by this benchmark. The RMSD obtained in this problem is 55.77 for the oil production values and 68.08 for cumulative oil production. In order to know the behavior of the fluids flow in the layer where the production well is placed. Figure 13 shows the saturation profiles S_w in this layer for six selected simulation times by using the grid size proposed by Nghiem *et al*. (1991). For the saturation profiles belonging to 100 and 300 simulation days, it is noted that the water has begun to sweep the oil present in the layer forming a "water feather". For the 1,200 and 1,500 profiles the water feather has spread out to more than a half the domain. This means that about 40% of the oil present in the layer has already been produced.

Numerical performance experiments

In order to analyze the performance of the numerical code, the five spot water injection problem was selected. Numerical parameters selected were: $\Delta S_w=1\text{x}10^{-05}$ for water saturation and $\Delta p_o=1\text{x}10^{-03}$ for oil pressure. Stop criterion for leaving the Newton-Rapshon loop was selected to: $|\delta S_w| < 1\text{x}10^{-03}$ and a fixed time step of 0.01 day was chosen; results are saved every 1.0 day. 10 days were selected for the total simulation time.

Numerical results presented in this section were obtained by executing our numerical code in a workstation with a single processor Intel (R) i7 (R) CPU 3820 3.60 GHz, 16 Gigabytes of RAM and an NVIDIA Tesla C2075 (R) GPU with 448 cuda-cores and 6 Gigabytes of dedicated memory.

Table 5 shows the average run-time for each Newton-Raphson step. The Jacobian run-

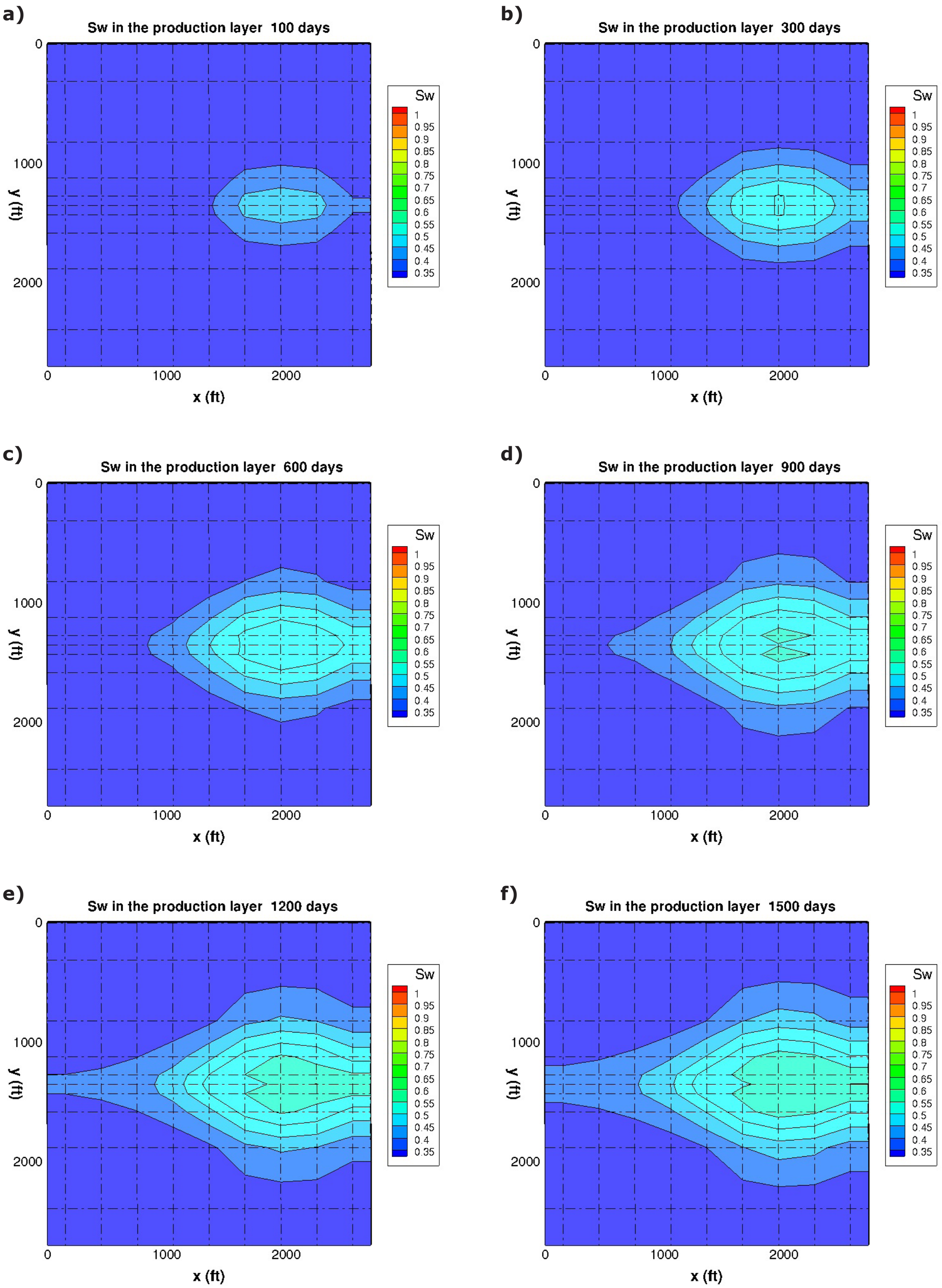

Figure 13. Water saturation profiles in the production layer for different simulation times.

time increases considerably when the number of volumes is bigger. As an example, 0.796 *s* were spended when volumes were 550x550 in CPU, while only 0.0379 *s* were used on the GPU that means 21x of speed up. This result is a considerable save of computation time taking into account that this procedure has to be repeated every Newton iteration.

Most authors indicate about 75% computation time is consumed in the solution of the system of linear equations. For solving the linear equations system, BICGSTAB solver without a preconditioner was used. This solver is already included in EIGEN and CUSP libraries (Jacob and Guennebaud, 2016; Maia and Dalton, 2016). Run times are shown in Table 6. Results indicate that CPU is faster than GPU when linear system is small (45,000 unknowns). When the linear system increases from 45,000 to 125,000 unknowns the computing time using the GPU is less than CPU. For a system with 605,000 unknowns, the maximum speed up is achieved (2.207x).

In a numerical code developed with GPU without graphics in real time, numerical results always have to be transfered from GPU to CPU for later processing. This process is computationally expensive because it has to be carried out each time step or when the user requires it. The time measured for this operation was from $1.69x10^{-05}$ to 0.101 seconds, for the 30x30 and 550x550 number of volumes, respectively. For this reason real speed up must be quantified when the whole numerical code has finished. Figure 14 shows run time and speed up for executing the whole code. In this figure can be noted GPU is slower than CPU when the problem is executed with few volumes. In the other hand, GPU speed up increases if the number of nodes for executing the problem increases. For executing the numerical code with 302,500 blocks (550x550 number of volumes) 3.0x of speed up is achieved, that is, the total run time for the CPU was 6.8 days whereas for the GPU it was only 2.26 days. It is worth mentioning that in this case the information transfer GPU-CPU does not have a considerable effect, since it was executed only 10 times. It should be kept in mind that this is a benchmark problem, therefore it is not necessary to use a bigger grid size to solve it adequately.

Conclusions

Sequential and parallel implementations of a fully implicit simulator for waterflooding process have been presented. Both implementations were validated with three different benchmarks and similar results were obtained in comparison with other authors and in comparison with analytical

Table 5. Average run-time obtained to compute the Jacobian.

Number of volumes	CPU run-time (s)	GPU run-time (s)	Speed up (x)
30x30	0.00284	0.00084	3.38x
90x90	0.02340	0.00164	14.26x
150x150	0.07141	0.00311	22.96x
250x250	0.15049	0.00754	19.95x
550x550	0.79686	0.037937	21.00x

Table 6. Average run-time obtained to solve the linear equations system.

Number of volumes	Unknowns number	CPU run-time (s)	GPU run-time (s)	Speed up (x)
30x30	1,800	0.007599	0.21234	0.035x
90x90	16,200	0.19308	0.85252	0.226x
150x150	45,000	0.98792	1.0727	0.9209x
250x250	125,000	4.3418	2.7515	1.570x
550x550	605,000	29.408	13.32	2.207x

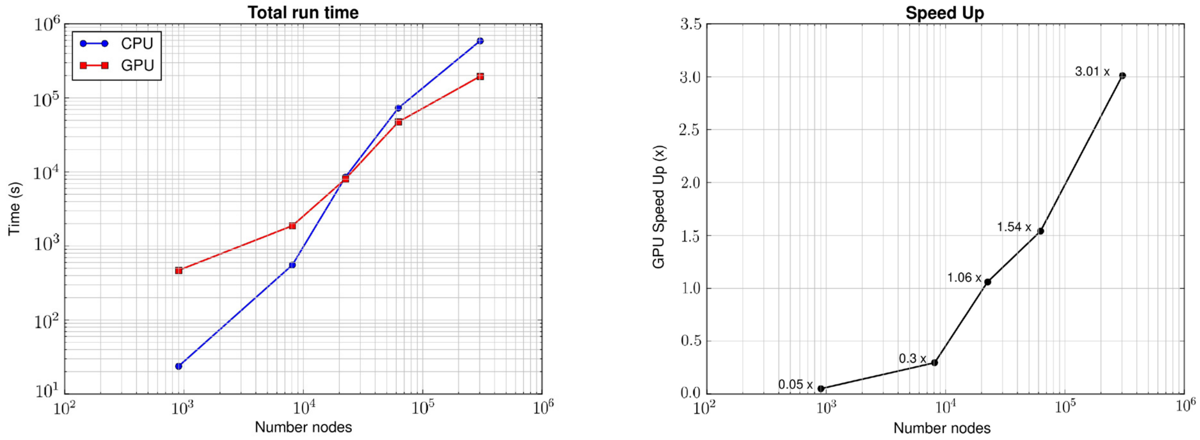

Figure 14. Numerical performance: a) CPU & GPU total run-time and b) GPU speed up.

solutions. The strategy of parallelization allows to reduce the calculation time of the Jacobian matrix, resulting from the Newton-Raphson method, using the architecture of the GPUs. Numerical results indicate that the GPU implementation reach until 22.9 times faster than the CPU counterpart for the finest mesh. On the other hand, the solution of the final linear system was also carried out in the GPU. A speed up of this step of 2.2 for the finest mesh was ontained. In total, taking into account the construction of the Jacobian matrix, the solution of the linear system and the exchange of information between CPU and GPU, gave a total speed up to 3. As expected, this speed up can be improved as the number of unknowns is incremented, however, the limited number of threads and memory of GPUs is a first obstacle to go forward. Even though the libraries used for solving the linear systems are optimized, they need to be improved with special preconditioners in order to obtain better results in terms of CPU and GPU time, and pair the 22x of speed up that was achieved in the present best calculation of Jacobian matrix. On the other hand, the GPU used in this work is not the newest one in the market, in such a way that a limitation occurs by the number of CUDA cores (448) and the memory (6GB) of the hardware; however, as can be seen, as the size of the problem increase, the speed up improves, therefore if, for example a GPU Tesla K40m (2880 CUDA cores and 12 GB in memory) is used better results can be expected. Finally, the present strategy can be used for several number of GPUs along with domain decomposition methods; this allows to increase even more the size of the problem (to several millions of unknowns) and as a consequence the speed up will be improved. Of course, this requires better solvers for the linear systems, for example geometric or algebraic multigrid methods.

Acknowledgments

V. Leonardo Teja-Juárez acknowledges the financial support from Consejo Nacional de Ciencia y Tecnología (CONACYT, MX) with the scholarship number 327261. Special thanks to my tutor committee: PhD. Ismael Herrera Revilla and PhD. Simon Lopez Ramirez for their valuable comments and advice during the development of this work.

References

Abou-Kassem J.H., Farouq-Ali S., and Islam M.R., 2006, Petroleum Reservoir Simulations: a basic approach. Gulf Publishing Company, Texas, pp 445.

Anciaux-Sedrakian A., Eaton J., Gratien J., Guignon T., Havé P., Preux C., Ricois O., and others, 2015. Will GPGPUs be finally a credible solution for industrial reservoir simulators? in SPE Symposium on Reservoir Simulation. Houston, Texas, 23-25 February.

Chen Z., 2007, Reservoir simulation: mathematical techniques in oil recovery. SIAM, Philadelphia, pp 219.

Chen Z., Huan G., and Ma Y., 2006, Computational methods for multiphase flows in porous media. SIAM, Philadelphia, pp 521.

de la Cruz, L.M. and Monsivais D., 2014, Parallel numerical simulation of two-phase flow model in porous media using distributed and shared memory architectures. *Geofísica internacional*, 53(1):59–75.

Dogru A.H., Fung L.S., Middya U., Al-Shaalan T.M., Pita J.A., HemanthKumar K., Su H., Tan J.C., Hoy H., Dreiman W., 2009, A next-generation parallel reservoir simulator for giant reservoirs, In SPE/EAGE Reservoir Characterization & Simulation Conference, Abu Dhabi, United Arab Emirates, 19-21 October.

Herrera I. and Pinder G.F., 2012, Mathematical modeling in science and engineering: An axiomatic approach. John Wiley & Sons, New Jersey, pp 243.

Jacob B., and Guennebaud G., and others, 2016, template library for linear algebra, EIGEN C++, Web page: http://eigen.tuxfamily.org.

Killough J., Bhogeswara R., and others, 1991, Simulation of compositional reservoir phenomena on a distributed-memory parallel computer. *Journal of Petroleum Technology*, 43(11):1–368.

Lake L.W., 1989, Enhanced Oil Recovery. Prentice Hall, New Jersey, pp 550.

Latil M., 1980, Enhanced oil recovery. Éditions Technip, Paris, pp 239.

Li R. and Saad Y., 2013, GPU-accelerated preconditioned iterative linear solvers. *The Journal of Supercomputing*, 63(2):443–466.

Liu H., Wang K., Chen Z., Jordan K., Luo J., Deng H., and others, 2015, A parallel framework for reservoir simulators on distributed-memory supercomputers, in SPE/IATMI Asia Pacific Oil & Gas Conference and Exhibition. Bali, Indonesia, 20-22 October

Liu H., Yu S., Chen Z., 2013, Development of algebraic multigrid solvers using GPUs, in SPE Reservoir Simulation Symposium, The Woodlands, Texas, 18-20 February.

Ma Y. and Chen Z., 2004, Parallel computation for reservoir thermal simulation of multicomponent and multiphase fluid flow. Journal of Computational Physics, 201(1):224–237.

Maia F., and Dalton S., and others, 2016, Generic parallel algorithms for sparse matrix and graph computations, CUSP, Web page: http://cusplibrary.github.io/.

Mukundakrishnan K., Esler K., Dembeck D., Natoli V., Shumway J., Zhang Y., Gilman J.R., Meng H., and others, 2015, Accelerating tight reservoir workflows with GPUs, in SPE Symposium on Reservoir Simulation. Houston, Texas, 23-25 February.

Nghiem L., Collins D.A., Sharma R., 1991, Seventh SPE comparative solution project: Modelling of horizontal wells in reservoir simulation, in SPE Symposium on Reservoir Simulation, Anaheim, California, 17-20 February.

NVIDIA, 2012, NVIDIA CUDA C Programming Guide, Version 4.2, Web page: http://docs.nvidia.com/cuda/cuda-c-programming-guide.

Peaceman D.W., 1977, Fundamentals of numerical reservoir simulation. Elsevier, Texas, pp 176.

Sanders J., and Kandrot E., 2010, CUDA by Example: An Introduction to General-Purpose GPU Programming. Addison-Wesley Professional, Boston, pp 290.

Shiralkar G.S., Stephenson R., Joubert W., Lubeck O., van Bloemen Waanders B., 1998, Falcon: A production quality distributed memory reservoir simulator. *SPE Reservoir Evaluation & Engineering*, 1(05):400–407.

Trapeznikova M.A., Churbanova N.G., Lyupa A.A., and Morozov D.N, 2014, Simulation of multiphase flows in the subsurface on GPU-based supercomputers*. Parallel Computing: Accelerating Computational Science Engineering (CSE), Advances in Parallel Computing*, 25:324–333.

Wang K., Liu H., and Chen Z., 2015, A scalable parallel black oil simulator on distributed memory parallel computers. *Journal of Computational Physics*, 301:19–34.

Yu S., Liu H., Chen Z., Hsieh B., Shao L., 2012, GPU-based parallel reservoir simulation for large-scale simulation problems, in SPE Europec/EAGE Annual Conference, Copenhagen, Denmark, 4-7 June.